cy 2

The Nuclear Spins, Hyperfine Structure Separations, and Magnetic Moments of Cs^{127}, Cs^{129}, Cs^{130}, and Cs^{132}

By

Howard Alan Shugart

B.S. (California Institute of Technology) 1953

M.A. (University of California) 1955

DISSERTATION

Submitted in partial satisfaction of the requirements for the degree of

DOCTOR OF PHILOSOPHY

in

Physics

in the

GRADUATE DIVISION

of the

UNIVERSITY OF CALIFORNIA

Approved:

Henry Briggs Silsbee
William A. Nierenberg
John O. Rasmussen

Committee in Charge

June 1957

DISCLAIMER

UCRL-3770

UNIVERSITY OF CALIFORNIA

Radiation Laboratory
Berkeley, California

Contract No. W-7405-eng-48

The Nuclear Spins, Hyperfine Structure Separations, and Magnetic Moments of Cs^{127}, Cs^{129}, Cs^{130}, and Cs^{132}

Howard Alan Shugart

May 15, 1957

Printed for the U. S. Atomic Energy Commission

TABLE OF CONTENTS

Table of Contents (continued)

ABSTRACT

The nuclear spins, hyperfine structure separations, and magnetic moments of four cesium isotopes have been measured, using an atomic beam magnetic resonance apparatus designed to utilize the low background flop-in method. The results are:

Isotope	$\tau_{1/2}$	I	$\Delta\nu$ (mc/sec)	μ_I (n.m.)
Cs^{127}	(6.2 hr)	1/2	8960 ± 200	+ 1.44 ± .03
Cs^{129}	(31 hr)	1/2	9230 ± 200	+ 1.48 ± .03
Cs^{130}	(30 m)	1	6420 ± 350 if	+ 1.37 ± .08
			6800 ± 350 if	- 1.45 ± .08
Cs^{132}	(6.2 d)	2	8653 ± 30	+ 2.22 ± .02

The spin measurement by Bellamy and Smith of I = 5/2 for (9.7 d) Cs^{131} has also been verified, using a different method of isotope preparation, detection, and identification.

The isotopes Cs^{127}, Cs^{129} and Cs^{130} were prepared by (α,kn) reactions in $iodine^{127}$, while Cs^{129}, Cs^{131}, Cs^{132}, and other cesium isotopes were produced by (p,n) reactions in normal gaseous xenon.

Detection of resonances of these radio-isotopes was accomplished by observing the activity deposited on sulfur-coated "buttons". Upon removal from the vacuum, the sulfur collectors were counted in x-ray scintillation counters, employing 2 mm sodium iodide, thallium-activated crystals and high gain photomultiplier tubes. In most cases the counters were set for the K x-ray emitted following capture of the K electron by the nucleus. At these settings the low counter background (~ 1 count/min) permitted the

observation of very low intensity resonances.

The hyperfine structure separation of each isotope is obtained by observing the frequency of the associated resonance at progressively higher magnetic fields, where the frequency contains an appreciable quadratic shift. Using the Fermi-Segrè relation, the nuclear moment follows from the hyperfine structure measurement.

The theory of the experiment, apparatus modifications, experimental procedure, and treatment of experimental data and results are described.

I. INTRODUCTION

During the last few years attempts have been made to measure the nuclear spins and magnetic moments of many isotopes of a given element in an effort to substantiate or contradict present ideas concerning the structure of the atomic nucleus. These measurements, at present, appear to form one of the most direct tests of a particular nuclear model and are rapidly becoming accessible to experimentalists in several fields. Once an element has been investigated, a study of its isotopes, where the constituent nuclei differ only in the number of neutrons, presents a relatively simple instrumentation problem, since all the members of the series possess nearly identical physical and chemical properties. On the other hand, the available quantity of many isotopes is so small that special methods and precautions must be observed to obtain measurable signals. Most attempts in this direction using the atomic beam magnetic resonance method have utilized the low background techniques of mass spectrographic or radioactive detection.

Perhaps equally important in the study of nuclear structure, it is desirable to have a knowledge of long series of isotones, where adjacent constituents differ by a single proton. This information involves acquiring observations of many chemically different elements and will likely be obtained through the study of the isotopes of neighboring elements.

Many experimental techniques, including molecular beams, microwave spectroscopy, optical spectroscopy, paramagnetic resonance, β- and γ-ray spectroscopy, and others, have aided in furthering the knowledge of nuclear properties. Of these, the one which treats the atom in the most isolated

state is that of molecular beams. From the pioneering experiments of Dunoyer in 1911 (DUN 11), the study of collision-free beams of particles has grown in importance under the direction of many capable scientists. The technique was used by Stern (STE 21) in 1921 to demonstrate the space quantization of angular momentum and to measure magnetic moments crudely. Later, through the introduction of radiofrequency spectroscopy, Rabi and others (RAB 38) provided a precision in the method, so now very accurate measurements of the electric and magnetic properties of nuclei, atoms, and molecules are possible.

The particular phase of atomic beam resonance methods to be discussed here is only an application of a single technique of the many which exist today. Although descriptions of apparatus and measurements of atomic, nuclear and molecular properties are scattered through the literature, several authors have effectively reviewed the field of molecular beams. (FRA 31, 37, HAM 41, BES 42, KEL 46, EST 46, KUS 50, RAM 50, 53, 56, SMI 55.) The advancing scope of information accessible to measurement, and the many recent refinements in instrumentation assure an increasing interest in molecular and atomic beam research, as a tool in precision measurements and even recently in accurate frequency or time standards.

The apparatus employed in the work described here utilizes the flop-in method first used by Zacharias and his coworkers (ZAC 42). All of the major constructional details of the present apparatus, along with the optimum design criteria used in its conception, are presented in the Ph.D. thesis of Robert J. Sunderland (SUN 56A). Briefly and only qualitatively the system is described as follows. From the instant an atom leaves the

atomic beam oven, it finds itself in an excellent vacuum where the mean free path is many times the largest dimension of the apparatus. Those atoms travelling in the proper direction after leaving the oven, pass between the pole tips of three separate electromagnets (denoted A, C, and B successively from the oven toward the detector). The A and B magnetic fields possess, in the horizontal direction, a large magnetic field gradient, which serves to deflect any atom having a magnetic moment. The C field, along with an impressed radiofrequency magnetic field, functions as a means to induce changes in the state of the atom before it enters the B field. Thus, ideally, when an atom traverses the entire length of the fields in a given quantum state, it is completely deflected out of the beam and misses the detector. To exclude atoms with high velocity and any molecular species which would suffer little or no deflection, a stop wire, placed in the B magnet, intercepts these atoms which otherwise would contribute to a large background at the detector. On the other hand, when the proper transition occurs in the C field, the A and B magnets act on the atom in opposite directions. While the A magnet causes a deflection in one direction, in a special case discussed later, the B magnet affects the atom in the opposite sense, causing a deflection which counteracts the deflection produced by the A magnet. This has the net effect of permitting those atoms which underwent a transition in the C field to reach the detector and be observed as a resonance. By the nature of the method, no atoms should reach the detector [except for small gas scattering and Majorana transitions (MAJ 32)] unless they undergo the proper transition in the C field region. In this way resonances appear as increases in the number of

atoms reaching the detector. To observe the small number of radioactive atoms hitting the detector, the beam is collected on sulfur-coated "buttons" and counted in x-ray counters to determine the activity of the deposit. By observing the frequency of a resonance and the corresponding value of the static C field at several different settings, the spin, hyperfine structure separation and magnetic moment may be calculated.

The Cs atomic beam experiment carried out here is part of a program of the Atomic Beam Laboratory of the University of California for the systematic atomic beam study of nuclear properties of radioactive species. After a series of measurements here on alkali halides with a molecular beam machine by G. Bemski (BEM 53) the atomic beam work under the direction of Professors William A. Nierenberg and Henry B. Silsbee began with a zero moment apparatus, which J. P. Hobson and J. C. Hubbs used to measure the spin, hyperfine structure and magnetic moment of 4.7 hr Rb^{81} (HOB 54, 54A, 55, HUB 54, 55). Because efforts with this apparatus to obtain the spin of 6.3 hr Rb^{82} failed, R. J. Sunderland converted the zero moment machine into the present magnetic resonance, flop-in apparatus and measured the nuclear spins of 6.3 hr Rb^{82}, 83 d Rb^{83}, and 34 d Rb^{84} (SUN 56, 56A, HOB 56). Since then, properties of the following radio-isotopes have been measured: nuclear spin of 31.5 m Rb^{81m} (SHU 56, HUB 56); hyperfine structure and magnetic moments of Rb^{81}, Rb^{82}, Rb^{83}, Rb^{84} (HUB 57A); nuclear spin of 6.2 hr Cs^{127}, 31 hr Cs^{129}, and 30 m Cs^{130} (NIE 56); nuclear spin of 7.1 d Cs^{132} (NIE 56A); nuclear spin of 40 d Ag^{105} (SIL 56); nuclear spin of 3.3 hr Cu^{64} (NIE 57); and the nuclear spin of Ga^{66} and 72 hr Ga^{67} (HUB 57). Results concerning the hyperfine structure separations of the Cs isotopes

(SIL 57) discussed in this thesis are to be published soon.

Work is now in progress on K^{43}, Ag^{106}, and Ag^{110m}. With the construction of an evaporator for the separation of radio-isotopes from the target material, W. B. Ewbank plans to attack the problem of the neutron-deficient Cu, Ag and Au isotopes. Likewise, many other nuclear species fall into the class of elements available to the atomic beam apparatus and are presently being considered for investigation. In addition, this laboratory operates two other atomic beam machines (under the direction of Drs. J. C. Hubbs and E. Lipworth, respectively) for investigation of the transuranic elements and the halogen atoms. The transuranic machine has been used to investigate the thallium isotope spins by G. O. Brink (BRI 56, 57A) and the gallium isotopes by J. L. Worcester (WOR 57).

The first element investigated by Lipworth, et al. in the halogen apparatus has been iodine. A fourth atomic beam machine, being constructed by G. O. Brink, J. Khan, and J. Winocur, will be applied to the problem of the hyperfine structure anomalies of most of the elements previously investigated here. Because of the large number of easily obtainable, relatively long-lived, neutron-deficient Cs isotopes, the hyperfine structure anomalies of Cs^{127}, Cs^{129}, Cs^{130}, Cs^{131}, and Cs^{132} will most likely be measured first. Once the technique of performing hyperfine structure anomaly experiments becomes established, the Rb isotopes may easily be measured by the same methods applied to the Cs isotopes.

The following thesis will describe original experiments conducted on the four neutron-deficient isotopes Cs^{127}, Cs^{129}, Cs^{130} and Cs^{132}.

II. THEORY OF THE EXPERIMENT

A. Theory of Hyperfine Structure Interaction

The atomic beam magnetic resonance method is best understood through a knowledge of the energy levels of an atom in a particular quantum state and subject to an external magnetic field. Such a description of the atomic energy levels must include the interaction energy originating between the atomic electrons and the nucleus, as well as that between the external magnetic field and both the electrons and the nucleus. The measurements of energy level differences by radiofrequency spectroscopy and the deflection properties of an atom in the inhomogeneous magnetic fields of the atomic beam apparatus rely on the variation in energy of an atom with a change in magnetic field or quantum state of the atom. The theory of the hyperfine structure interaction has been worked out in great detail by many authors and explained in many ways. The explanation included here follows those given in some of the following sources and compilations: SMI 55, RAM 53, 56.

A consistent description of the nuclear and atomic interactions usually begins with a few assumptions and definitions:

1. The nucleus contains a charge Ze confined to a small region near the center of the atom.

2. The nuclear spin, I, denotes in units of $\hbar$ the total nuclear angular momentum.

$$\overrightarrow{\text{ang. mom.}} = \hbar\vec{I}. \qquad (1)$$

The value of the nuclear spin, I, is integral if the nucleus possesses an

even number of constituent nucleons and half odd integral for an odd number of particles. Likewise, integral spin nuclei obey Bose-Einstein statistics, while half integral ones obey Fermi-Dirac statistics.

3. The magnetic moment, $\vec{\mu}_I$, and the spin, $\vec{I}$, are used to define the nuclear gyromagnetic ratio, γ_I, and the nuclear g-factor, g_I, by the equations

$$\vec{\mu}_I = \gamma_I \hbar \vec{I} = g_I \mu_o \vec{I}, \tag{2}$$

where μ_o is the Bohr magneton, $|e|\hbar/2mc = +.92732(6) \times 10^{-20}$ ergs gauss^{-1}; e is the electronic charge; m is the mass of the electron; c is the velocity of light; and $\hbar$ is Planck's constant divided by 2π.

Similar quantities and relations hold for the case of the atomic electrons to relate $\vec{\mu}_J$, $\vec{J}$ and g_J.

$$\vec{\mu}_J = \gamma_J \hbar \vec{J} = g_J \mu_o \vec{J}. \tag{3}$$

The lowest order interaction existing between a nucleus and the surrounding electrons may be considered in the first approximation as originating through the interplay of the nuclear magnetic moment with the magnetic field of the electrons at the nucleus. The discrete set of energy levels resulting from the various relative orientations of the nuclear magnetic moment and electronic magnetic field are designated as the hyperfine structure of the atom. The separation in energy between two sets of levels is called a hyperfine structure separation. In the approximation that the nucleus is a point dipole, this interaction has the form

$$\mathcal{H} = - \vec{\mu}_I \cdot \vec{H}_J , \tag{4}$$

where $\mathcal{H}$ is the Hamiltonian; $\vec{\mu}_I$ is the nuclear magnetic moment; and $\vec{H}_J$ is the magnetic field produced at the nucleus by the electrons of the atom. The negative sign is necessary, just as in classical electricity and magnetism, to assure that the lowest energy is assigned to the case where the magnetic dipole moment and the magnetic field are aligned.

For an atom with J and I greater than or equal to 1, the nuclear quadrupole moment may interact with the gradient of the electric field of the electrons to provide an additional term in the Hamiltonian. Likewise, for cases of higher angular momenta, higher order terms appear as a consequence of the possibility of having greater multipole moment orders and higher derivatives of the electric and magnetic fields at the nucleus. At the present time, the number of quadrupole interactions which have been observed is quite large, but only a few magnetic octupole interactions have been detected (RAM 56).

Because the work described here pertains only to atoms in the $^2S_{1/2}$ ($\vec{L} = 0$, $\vec{S} = 1/2$, $\vec{J} = \vec{L} + \vec{S} = 1/2$) electronic state, the analysis is greatly simplified by the exclusion of all interactions other than the magnetic dipole one. While some of the nuclei described here may well possess quadrupole and higher order multipole moments, the spherical symmetry of the $^2S_{1/2}$ electronic configuration prohibits at the nucleus the existence of an electric field gradient and higher order electric or magnetic gradients arising from the electrons. In this way, no contribution to the atom's energy can result because of the lack of internal sources of field gradients. In all of the following work, the total electronic angular momentum is $\hbar/2$, unless otherwise specified.

Thus, in the absence of higher order interactions for zero external magnetic field, Eq. (4) provides a description of the hyperfine structure interaction of the cesium atom with which one is concerned here. Since the magnetic field, $\vec{H}$, at the nucleus is proportional to $\vec{J}$ for matrix elements diagonal in J, and since $\vec{\mu}_I$ is proportional to $\vec{I}$ by Eq. (2), the Hamiltonian of Eq. (4) becomes

$$\mathcal{H} = ha\vec{I} \cdot \vec{J}, \tag{5}$$

where

$$ha = -\left(\frac{\mu_I}{I}\right)\frac{\vec{H}_J \cdot \vec{J}}{\vec{J} \cdot \vec{J}} .$$

The value of a may be calculated theoretically under the assumptions that the nucleus is a uniformly magnetized sphere and that the magnetic moment density of the electron spin is constant within this sphere (FER 30). With these assumptions, the hyperfine structure interaction for a single electron in the $^2S_{1/2}$ state is

$$ha = \frac{8}{3}\frac{hcR\alpha^2 Z^3 g_I}{n^3(M/m)} , \tag{6}$$

where R is the Rydberg constant; α is the fine structure constant; M is the proton mass; m is the electron mass; n is the principal quantum number; g_I is the nuclear g-factor; Z is the charge of the nucleus; and h is Planck's constant. More complicated expressions exist for the interaction constant when the electron is not in an S state (GOU 33, BRE 28, 30, 33, 48, 49, MAR 40), or when two electrons contribute to the field (KOS 52, SCH 55).

The total angular momentum in units of $\hbar$, $\vec{F}$, of an atom is obtained by

the addition of $\vec{I}$, the nuclear spin, and $\vec{J}$, the electronic spin:

$$\vec{F} = \vec{I} + \vec{J}. \tag{7}$$

Thus the angular momentum state of an atom may be expressed, for the case when $\vec{I}$ and $\vec{J}$ are coupled to form an $\vec{F}$, by designating the value of F and also the value, m, the component of $\vec{F}$ in the z direction. This type of coupling is observed to hold in weak external magnetic fields, where $\vec{F}$ precesses about the field. For strong external magnetic fields, $\vec{I}$ and $\vec{J}$ precess individually about $\vec{H}$, with the result that I, J, m_I, m_J are the best quantum numbers to describe the system. Figs. 1a and 1b help depict the manner of precession of $\vec{F}$, $\vec{I}$, and $\vec{J}$ in a weak magnetic field and of $\vec{I}$ and $\vec{J}$ in a strong magnetic field.

Associated with the external magnetic field and the various magnetic moments, $\vec{\mu}$, of the atom are further terms in the Hamiltonian expressing additional energy of the atom of the form

$$\mathcal{H} = - \vec{\mu} \cdot \vec{H}_o , \tag{8}$$

where H_o = externally applied magnetic field. As a consequence, the total Hamiltonian for the atom may be written, using Eqs. (5) and (8),

$$\mathcal{H} = ha\vec{I} \cdot \vec{J} - \frac{\mu_J}{J} \vec{J} \cdot \vec{H}_o - \frac{\mu_I}{I} \vec{I} \cdot \vec{H}_o . \tag{9}$$

In this expression, the second and third terms describe the effect of the external magnetic field upon the atomic energy levels, which, in the absence of such a field, have structure by virtue of the first or hyperfine structure interaction term.

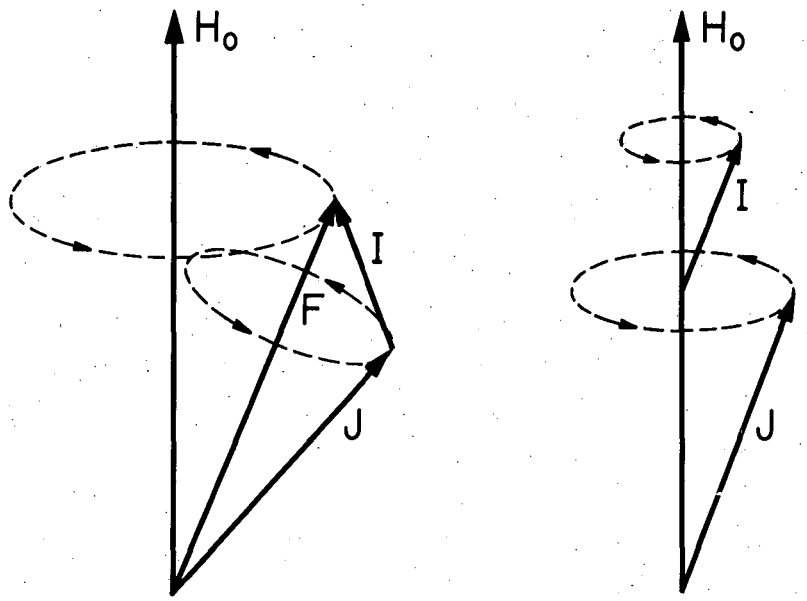

MU-13365

Figs. 1a and 1b. Precession of I, J, and F in a weak and strong magnetic field.

If one assumes the weak field coupling of $\vec{I}$ and $\vec{J}$ to form an $\vec{F}$, only the components of $\vec{\mu}_I$ and $\vec{\mu}_J$ along $\vec{F}$ are effective in producing a magnetic moment capable of interacting with the external field. The components perpendicular to $\vec{F}$ average to zero as $\vec{I}$ and $\vec{J}$ precess about $\vec{F}$. In this case,

$$\vec{J} \cdot \vec{H}_o = \vec{J} \cdot \frac{\vec{F}}{|F|} \frac{\vec{F} \cdot \vec{H}_o}{|F|},$$

$$\vec{I} \cdot \vec{J} = \frac{\vec{F}^2 - \vec{I}^2 - \vec{J}^2}{2} = \frac{F(F+1) - I(I+1) - J(J+1)}{2},$$

and

$$\vec{J} \cdot \vec{F} = \frac{F(F+1) + J(J+1) - I(I+1)}{2F(F+1)}.$$

Then, using the F, m representation, Eq. (9) becomes

$$W(F,m) = (Fm|\mathcal{H}|Fm)$$

$$= ha(Fm|I\cdot J|Fm) - \frac{\mu_J}{J} \frac{F(F+1) + J(J+1) - I(I+1)}{2F(F+1)} (Fm|F\cdot H_o|Fm)$$

$$- \frac{\mu_I}{I} \frac{F(F+1) + I(I+1) - J(J+1)}{2F(F+1)} (Fm|F\cdot H_o|Fm). \qquad (10)$$

Substituting the value of the diagonal matrix elements results in

$$W(F,m) = -\frac{ha}{2}[F(F+1) - I(I+1) - J(J+1)]$$

$$- \left[\frac{\mu_J}{J} \frac{F(F+1) + J(J+1) - I(I+1)}{2F(F+1)} \right.$$

$$\left. + \frac{\mu_I}{I} \frac{F(F+1) + I(I+1) - J(J+1)}{2F(F+1)} \right] mH_o. \qquad (11)$$

It is evident for zero external magnetic field that W(F,m) does not depend on m. Also the interval rule follows immediately,

$$W(F) - W(F - 1) = haF, \tag{12}$$

for $H_o = 0$. For the case of $J = 1/2$ and $F = I + 1/2$, the interval rule becomes

$$W(I + 1/2) - W(I - 1/2) = h\Delta\nu = ha\,\frac{2I + 1}{2}, \tag{13}$$

where $\Delta\nu$ is the hyperfine structure separation constant.

In the opposite extreme, when $\vec{I}$ and $\vec{J}$ are completely decoupled and precess individually about H_o, m_I and m_J are the appropriate quantum numbers. Physically, the decoupling of $\vec{I}$ and $\vec{J}$ may be thought of as occurring when the precession of $\vec{F}$ about the external magnetic field becomes comparable in frequency to the frequency of rotation of $\vec{I}$ and $\vec{J}$ about $\vec{F}$. Now, using the m_I,m_J representations, Eq. (9) becomes

$$W(m_I,m_J) = (m_I m_J|\mathcal{H}|m_I m_J) = ham_I m_J - \frac{\mu_J}{J} m_J H_o - \frac{\mu_I}{I} m_I H_o . \tag{14}$$

When two of the terms of the Hamiltonian of Eq. (9) become comparable, no simple representation has only diagonal matrix elements of the energy. In this case, solving the problem exactly requires obtaining all of the matrix elements in a convenient representation.

For intermediate magnetic fields, the secular equation is easily solved, using either the F,m or the m_I,m_J representation (BRE 31, RAM 56). The algebra necessary in either case is tedious, but straightforward.

The Breit-Rabi equation ($J = 1/2$) for the energy levels as a function of magnetic field follows from both cases. The usual expression of the

Breit-Rabi formula uses the parameter X in the following way:

$$W(F,m) = -\frac{\Delta W}{2(2I+1)} - \frac{\mu_I}{I} mH \pm \frac{\Delta W}{2}\left(1 + \frac{4mx}{2I+1} + x^2\right)^{1/2}, \qquad (15)$$

where

$$\Delta W = h\Delta\nu = ha\,\frac{2I+1}{2},$$

and

$$x = \frac{\left(-\frac{\mu_J}{J} + \frac{\mu_I}{I}\right) H_o}{\Delta W}.$$

The ± sign before the square root refers to $F = I + 1/2$ and $F = I - 1/2$ states respectively.

As an example of the normal diagram resulting from the plot of the Breit-Rabi formula, Figs. 2, 3, and 4 show the variation of the energy levels in an atom with $J = 1/2$, $I = 1/2$, 1 and 2, as a function of x (defined above). The nuclear magnetic moment is taken as positive, but its magnitude is neglected in computing these diagrams. The effect of a negative nuclear magnetic moment is to rotate the Breit-Rabi diagram 180° about the abscissa. Also there are slight shifts in the level spacings, if one does not neglect the g_I or μ_I terms in Eq. (15). These diagrams will later serve to illustrate the possible transitions observable in the atomic beam apparatus used here.

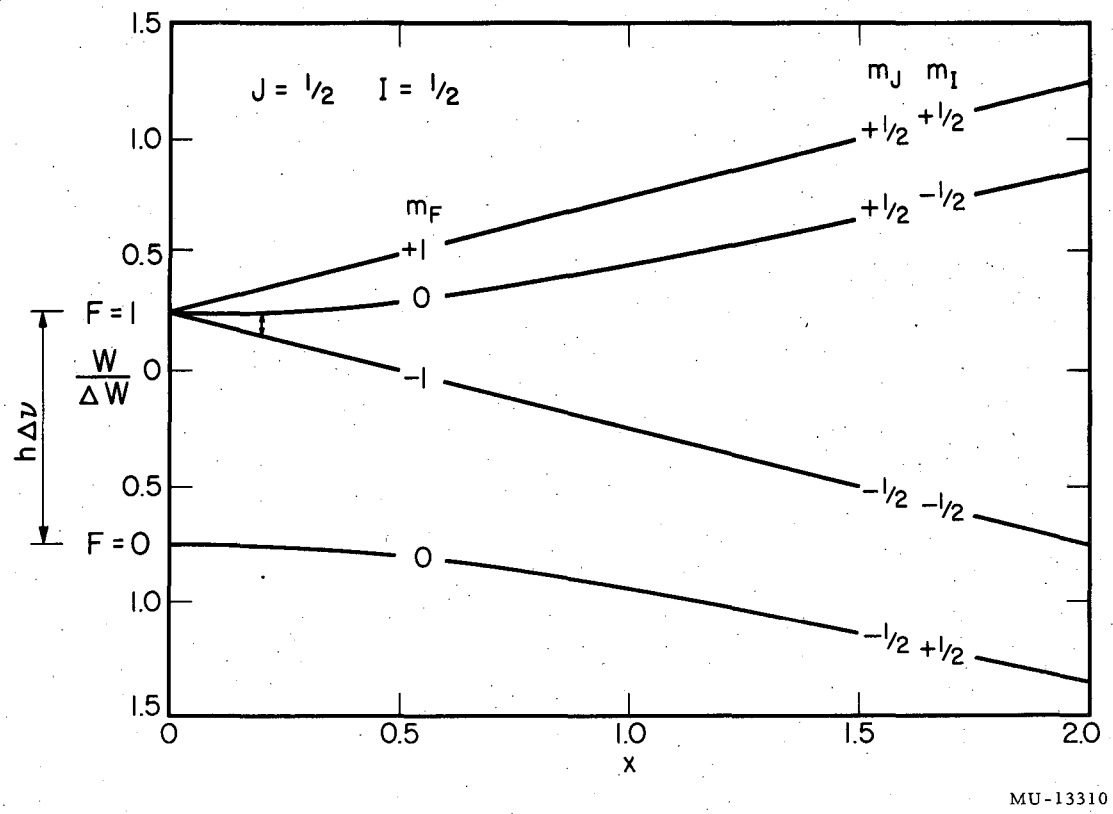

Fig. 2. Breit-Rabi diagram for J = 1/2 and I = 1/2.

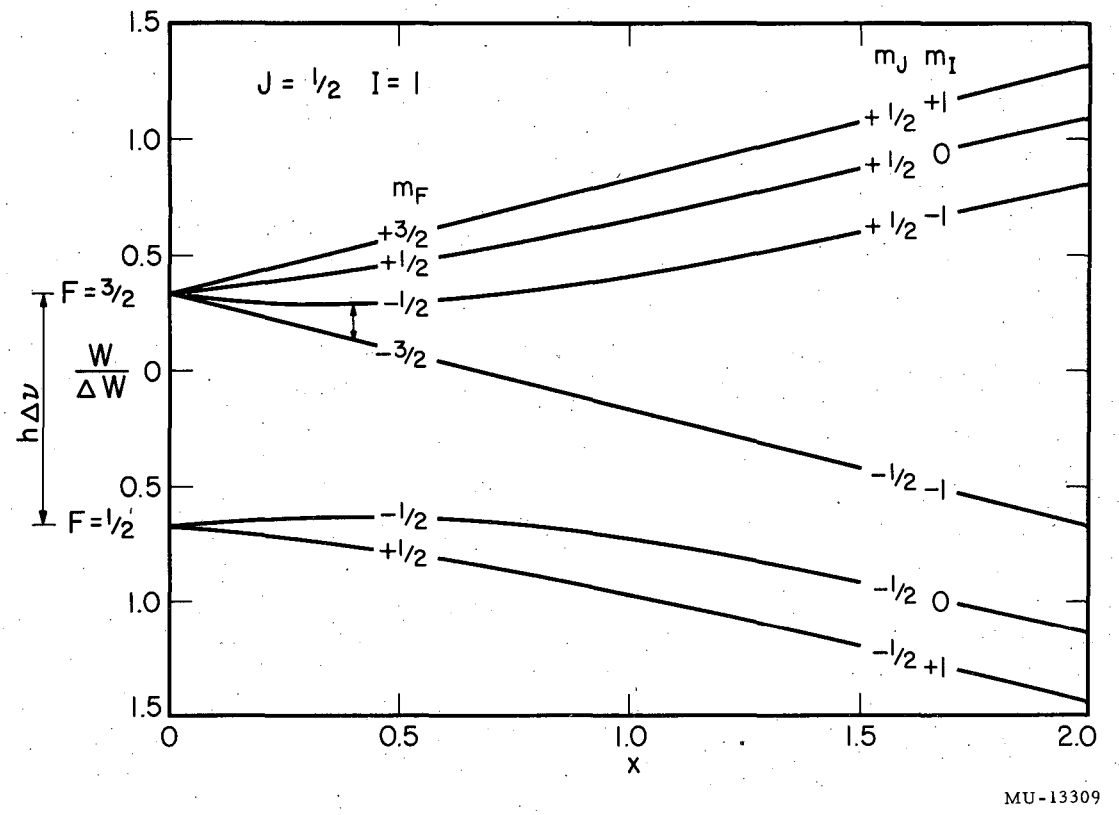

Fig. 3. Breit-Rabi diagram for J = 1/2 and I = 1.

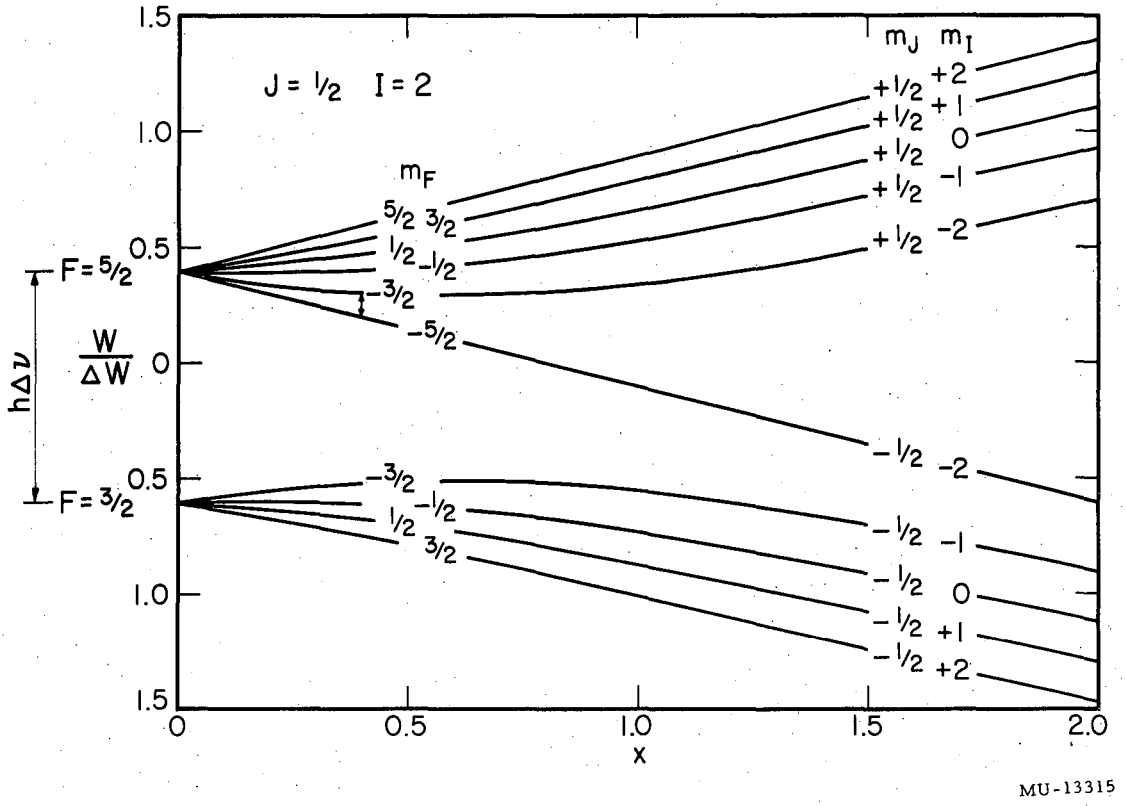

Fig. 4. Breit-Rabi diagram for J = 1/2 and I = 2.

B. Observable Transitions in the Atomic Beam Flop-In Technique

A schematic drawing of the atomic beam apparatus used in these experiments is shown in Fig. 5. The inhomogeneous A and B magnetic fields have their field gradients pointing in the same direction. Therefore, the force experienced by a magnetic moment oriented similarly in these two fields will be in the same direction in both fields and of magnitude

$$\vec{F} = - \nabla W = - \frac{\partial W}{\partial H_o} \nabla H_o = \mu_{eff} \nabla H_o \, , \tag{16}$$

where $\mu_{eff} = - \partial W / \partial H_o$ is the component of $\vec{\mu}$ along $\vec{H}_o$. The value of μ_{eff} may be obtained by differentiating Eq. (15) with respect to H to obtain

$$\mu_{eff} = - \frac{\partial W}{\partial H_o} = m g_I \mu_o \mp \frac{1}{2} (g_I - g_J) \mu_o \frac{\left(\frac{2m}{2I+1} + x \right)}{\left(1 + \frac{4mx}{2I+1} + x^2 \right)^{1/2}} \, , \tag{17}$$

in the F,m representation, with the $\mp$ sign referring to $F = I + 1/2$ and $F = I - 1/2$ states respectively. For large fields where the m_I, m_J representation is convenient to use, the effective magnetic moment may be expressed, using Eq. (14),

$$\mu_{eff} = - \frac{\partial W}{\partial H_o} = \frac{\mu_J}{J} m_J + \frac{\mu_I}{I} m_I \, . \tag{18}$$

Since $\mu_J \approx \pm 2000 \, \mu_I$, the effective magnetic moment is of the order of one Bohr magneton ($e\hbar/2mc$), or about $.9 \times 10^{-20}$ ergs/gauss. Because the effective magnetic moment is the negative slope of curves drawn in the Breit-Rabi diagrams of Figs. 2, 3, and 4, reference to these diagrams

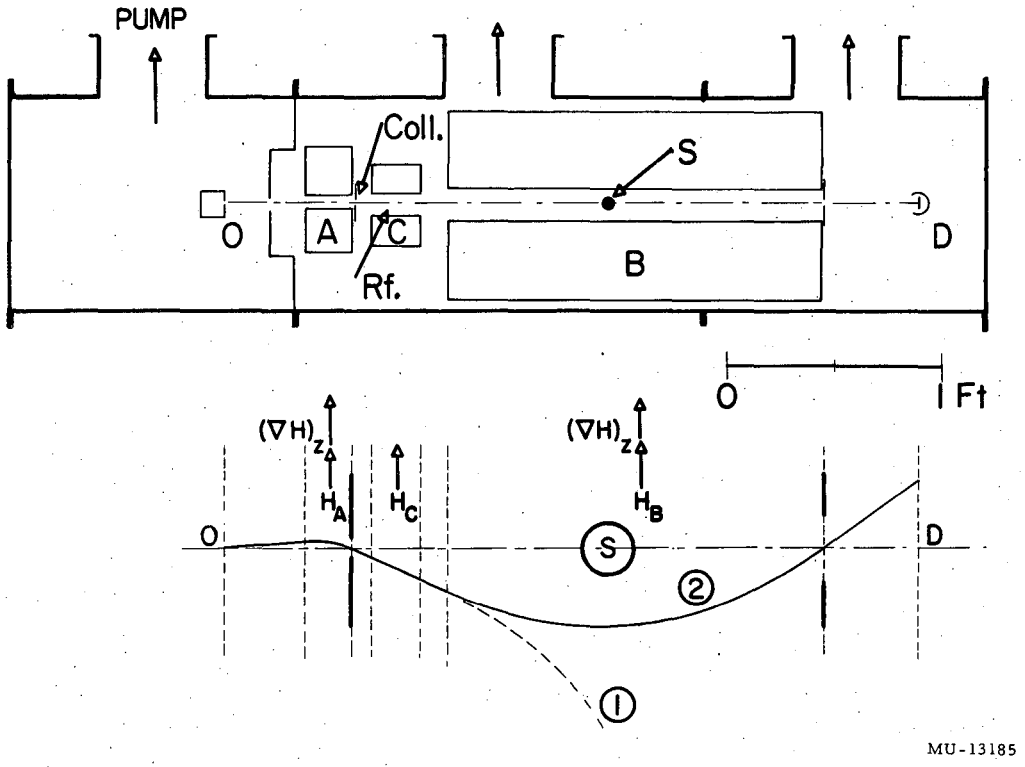

Fig. 5. Schematic arrangement and trajectory in an atomic beam, flop-in apparatus.

quickly shows the variation of the effective magnetic moment with magnetic field. Above a value of 2 for x, all states have a moment of the order of $\pm \mu_o$ (1 Bohr magneton). As the field decreases, some states possess zero slope, and hence zero magnetic moment. Observation of the conditions for transmission of atoms through an inhomogeneous field by virtue of their zero effective moment constitutes the "zero moment method". This method has been used in the investigation of nuclear properties by Millman (MIL 35, 36, 38) and others (FOX 35, MAN 36, 36A,37, HAM 39, REN 40). The technique was first applied to short-lived radioactive species by Hobson, Hubbs, Nierenberg and Silsbee (HOB 54, 54A, 55, HUB 54, 55) in this laboratory.

For most atoms the value of the magnetic field for $x > \sim 1.5$ occurs in easily obtainable regions. Thus, if the A and B fields are set sufficiently high, the effective magnetic moment will be of the order of one Bohr magneton and essentially independent of m_I. Since the gradients of the A and B magnets are in the same direction, an atom in a given state in the two fields will be deflected similarly. If an atom starts from the oven, O, in Fig. 5, with a negative magnetic moment and receives a deflection, as shown in the A magnet, it will follow the trajectory ① under the assumption that no transition takes place in the state of the atom between the A and B fields. This trajectory misses the exit slit. On the other hand, if the state of the atom is changed in the C field, so that it now has a positive effective magnetic moment in the B field region, the atom is refocused around the stop wire, S, (trajectory ②) and passes through the exit slit. Those transitions which change the sign of the

effective magnetic moment at high fields are used in the flop-in method. Usually it is desirable to observe transitions at relatively low values of the C magnetic field ($x \ll 1$). Subject to the selection rules, $\Delta F = 0, \pm 1$, $\Delta m = 0, \pm 1$, the only transitions which cause moment reversal at high fields are:

$$\text{For } J \pm 1/2, \quad F = I + 1/2, \quad m = -I - 1/2 \leftrightarrow m = -I + 1/2,$$

$$\Delta F = \pm 1, \quad \Delta m = \pm 1 \text{ or } 0,$$

except $m = -I - 1/2 \leftrightarrow m = -I + 1/2$.

Those transitions for which $\Delta m = \pm 1$ are called π transitions and are induced by an oscillating magnetic field perpendicular to the static C field. Components of the oscillating field parallel to the static C field induce $\Delta m = 0$ or σ transitions. All of these transition frequencies, except the $m = -I - 1/2 \leftrightarrow m = -I + 1/2$ transition frequency, which approaches zero with the C magnetic field, are of the order of the hyperfine structure energy divided by h. For sufficiently weak C field, the energy difference of the $\Delta F = 0$, $m = -I - 1/2 \leftrightarrow m = -I + 1/2$ transition, which is used in the flop-in method, may be expressed in terms of the corresponding frequency as:

$$\text{For } J = 1/2, \text{ and } g_J \cong -2, \quad \nu \cong \frac{\mu_o H}{h(2I + 1)} \cong \frac{2.80\ H}{2I + 1} \text{ mc/gauss-sec.} \quad (19)$$

It is assumed here that the field is sufficiently low that higher order terms in H may be neglected.

C. Spin Assignments

Eq. (19) provides a convenient way of measuring nuclear spins if the transition frequency, ν, and the magnetic field, H, are known. In practice, the C magnetic field, H, is determined by calibration with an easily detected stable isotope whose spin is well known. In the experiments presented here, the low field resonance of stable Cs^{133} carrier ($I = 7/2$) served to calibrate the C field. Use of the stable carrier, effusing simultaneously with the radio-isotopes, provides a means of normalizing the beam, and insures that the trajectories of the calibration isotope and radio-isotopes are alike and hence subject to the same transition magnetic field, H. The radiofrequency hairpin used in this work provides an oscillating magnetic field parallel to the atomic beam but perpendicular to the static magnetic field, H. This provides observable π transitions of which $m = -I - 1/2 \leftrightarrow m = -I + 1/2$ is one. In practice, the step requiring the calculation of H is omitted by observing that

$$\nu = \frac{2I_o + 1}{2I + 1} \nu_o , \qquad (20)$$

where ν and I refer to an unknown isotope, and ν_o and I_o refer to the calibration isotope. During a spin search, exposures at the various frequencies corresponding to various values of I are made. Most of these exposures will contain only apparatus background. However, the one exposure, which is made at the frequency corresponding to the spin of the unknown isotope, will contain the atoms passed through the apparatus on resonance, in addition to apparatus background. In this way the nuclear

spin may be established.

Two difficulties prevent an unambiguous determination of the spin from only one observation. First, if one is operating at very low frequencies, the resonance width could be too great to permit the resolution of two adjacent spins. This becomes especially important when more than one isotope is present. In that case, the tail of a strong isotope might mask a weaker isotope resonance. Secondly, the assumptions on which Eqs. (19) and (20) are based, require that the second order effect of H is negligible. An approximate formula, which shows the quadratic dependence of frequency with the magnetic field is:

$$\nu \cong \frac{2.800H}{2I+1} + \left[\frac{2.800H}{2I+1}\right]^2 \frac{2I}{\Delta\nu}, \qquad (21)$$

where $\Delta\nu$ is the hyperfine structure separation and g_I again is neglected. When $\Delta\nu$ is small, the second term may become comparable to the resonance width, causing the resonance to be shifted away from the frequency predicted by Eqs. (19) and (20). If the shift is sufficient, it may actually cause the resonance to appear at a frequency corresponding to a smaller value of the spin. Doubt as to the value of the spin from the first run is removed by repeating the measurements at higher fields. The higher field resonance will confirm the spin assignment of the low field resonance and also place a lower limit on the hyperfine structure separation $\Delta\nu$.

D. Hyperfine Structure Separations

It is obvious from Eq. (21) that crude values of $\Delta\nu$ may be obtained from higher field resonances if the spin of the isotope is known. A more accurate expression for the hyperfine structure separation is obtained by writing the energy difference of the $F = I + 1/2$, $m = -I - 1/2 \leftrightarrow m = -I + 1/2$ transition, using the Breit-Rabi formula, Eq. (15). Setting the energy difference equal to the frequency of the transition, ν, and solving the resulting expression for $\Delta\nu$, gives:

$$\Delta\nu = \frac{\left(\nu + \frac{g_I \mu_o H}{h}\right)\left(-\frac{g_J \mu_o H}{h} - \nu\right)}{\nu + \frac{g_J \mu_o H}{(2I+1)h} + \frac{2I}{2I+1}\frac{g_I \mu_o H}{h}}, \qquad (22)$$

where $g_J = \mu_J/J$; $g_I = \mu_I/I$; μ_o = |Bohr magneton| ergs/gauss; h = Planck's constant (erg sec); H = magnetic C field (gauss); $\Delta\nu$ = hyperfine structure separation (mc/sec); ν = resonance frequency (mc/sec); I = nuclear spin angular momentum (units of $\hbar$); $\mu_o/h \approx 1.4$ mc/gauss-sec.

All of the quantities on the right-hand side of Eq. (22) are known or observable, except g_I, the nuclear g-factor. The numerical value of the nuclear g_I is obtained to within approximately one percent by the Fermi-Segre relation (FER 33),

$$\frac{\Delta\nu_1}{|g_{I_1}|(2I_1 + 1)} = \frac{\Delta\nu_2}{|g_{I_2}|(2I_2 + 1)}, \qquad (23)$$

where the subscript 1 refers to one isotope of a given element, and subscript 2 refers to a second isotope of the same element. The actual g_I

may differ slightly from the one calculated by this formula because of the diamagnetic shielding correction (LAM 41, RAM 52) and the hyperfine structure anomaly (BIT 49, BOH 50, 51, 51A). Still an ambiguity as to the sign of g_I remains, for Eq. (23) predicts only its absolute magnitude. Therefore, two different values of $\Delta\nu$ are obtained from ν and H by the simultaneous solution of Eqs. (22) and (23) for $\Delta\nu$, first assuming a positive g_I and then assuming a negative g_I. When observations at more than one field are made, the corresponding $\Delta\nu$'s are calculated, assuming a positive and then a negative nuclear magnetic moment. Either the $\Delta\nu$'s associated with the positive moment, or the ones associated with the negative moment, will show a consistency. This constancy of one set of $\Delta\nu$'s establishes the sign of the nuclear magnetic moment.

All of the previous discussion has treated only the low frequency $\Delta F = 0$, $m = -I - 1/2 \leftrightarrow m = -I + 1/2$ resonance. The hyperfine structure separation may also be determined from the $\Delta F = \pm 1$, $\Delta m = 0, \pm 1$ transitions in very weak fields. At zero field, the $\Delta F = 1$ transitions all occur at precisely $\Delta\nu$, but for small fields [which are necessary to prevent Majorana transitions which may take place in the changing field regions between magnets (MAJ 32)] a small correction due to the linear shift with field splits the line occurring at $\Delta\nu$ into a series of lines. The maximum possible number of these lines, both π and σ, for $J = 1/2$ is given by $2I$. While the direct observation of the $\Delta F = \pm 1$ transitions gives the hyperfine structure separation to the greatest accuracy, it is not feasible to start with it because of the enormous search problem. Nevertheless, once the hyperfine structure constant has been established

by the low frequency transition, $\Delta F = \pm 1$ transitions will serve to increase the accuracy of previous measurements and to strengthen the evidence for assigning the sign of the moment by confirming the choice of consistent set of $\Delta\nu$'s.

III. THE EXPERIMENTAL APPARATUS

A detailed account of the design and construction of the atomic beam apparatus used in these experiments appears in the thesis of R. J. Sunderland (SUN 56A). The existing equipment was built around the vacuum housing used in the zero moment experiment of Hobson and Hubbs (HOB 54A, HUB 54). The schematic diagram of Fig. 5 shows the general relationship among mechanical components, as well as the relative lengths of the A, B, and C fields. Table 1 gives some of the most important characteristics of the apparatus.

Since the equipment was assembled and aligned in February, 1956, it has received only minor internal alterations. An electron bombardment oven loader, internal radiofrequency coaxial cable, and different radiofrequency hairpins have been added. These additions and their effect on the apparatus' usefulness and characteristics will be discussed in the following sections.

A. Electron Bombardment Loader

Although not too important in the work here, the limitation on the maximum temperature obtainable with the conventional, resistance-heated, oven loader, shown in Figs. 6 and 7, made advisable the construction of an electron-bombardment heated device (Fig. 8), employing smaller ovens to reduce the radiation loss. Such an electron-bombardment oven loader was constructed. Its most important use was in the first run of Cs^{130}, where time was of the utmost importance. The low thermal capacity of the small electron-bombardment oven shown in Fig. 9 permitted establishing a beam of Cs atoms in about one minute, compared to twenty minutes for the resistance-heated oven. This represented a saving in time of almost one half-life in the case of Cs^{130}.

Table 1. Characteristics of the Atomic Beam Apparatus

Area of the source slit	8 to 32 $\times 10^{-5}$ in^2
Area of the detector slit	.05 in^2
Beam height at source	80 mils
Beam height at detector	500 mils
Temperature of source	~400° C
Length of A magnet	2.25 in
Length of B magnet	21.25 in
Length of C magnet	1.5 in
Total length of beam	32 in
Distance from source to A magnet	4.5 in
Distance of source from collimator	6.75 in
Radius of the bead of A magnet	.080 in
Radius of the groove of A magnet	.080 in
Radius of the bead of B magnet	.375 in
Radius of the groove of B magnet	.375 in
Magnetic field strength for A and B magnets	~5000 gauss
Magnetic field strength of C magnet	< 1000 gauss
Field gradient in A magnet $\partial H/\partial z$ / H	~6
Field gradient in B magnet $\partial H/\partial z$ / H	~1.3
Width of C magnet gap	.5 in
Number of turns in A magnet	6 turns
Number of turns in B magnet	24 turns
Number of turns in C magnet	~8000 turns
Current in A and B magnets	50 to 700 amperes

Table 1 (continued)

Current in C magnet	< 125 ma
Resistance of the A magnet winding	.00064 ohms
Resistance of the B magnet winding	.00237 ohms
Resistance of the C magnet winding	~1280 ohms
Power source for A and B magnets	Six 2-volt U.S. Navy submarime batteries of ~ 20,000 a-hr capacity connected to give 4 volts
Battery charger	600 a, 6v generator
C magnet power supply	Lambda Electronics Corp. Regulated Power Supply A1201
Oven chamber diffusion pump	One NRC H-6-P
Magnet chamber diffusion pumps	Two NRC H-6-P
Backing diffusion pumps between six-inch diffusion pumps and forepump	One NRC H-2-P
Operating vacua:	
Fore pressure	~1 to 3 × 10^{-3} mm
Oven chamber	~1 × 10^{-6} mm
Magnet chamber (untrapped)	~1 × 10^{-6} mm
Detector	Surface ionization hot wire type with electrometer shown in Fig. 13.

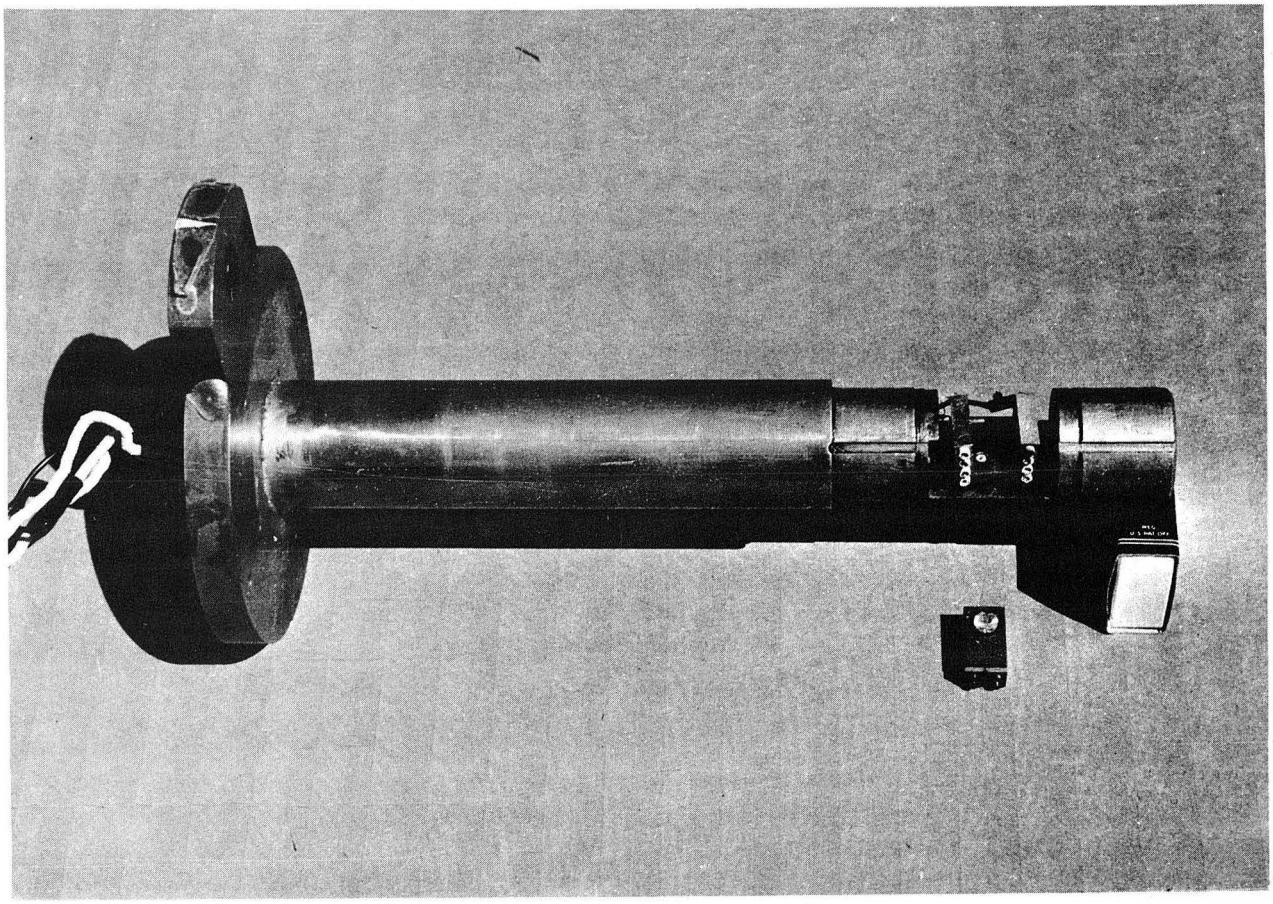

ZN-1718

Fig. 6. The resistance heated oven loader assembly.

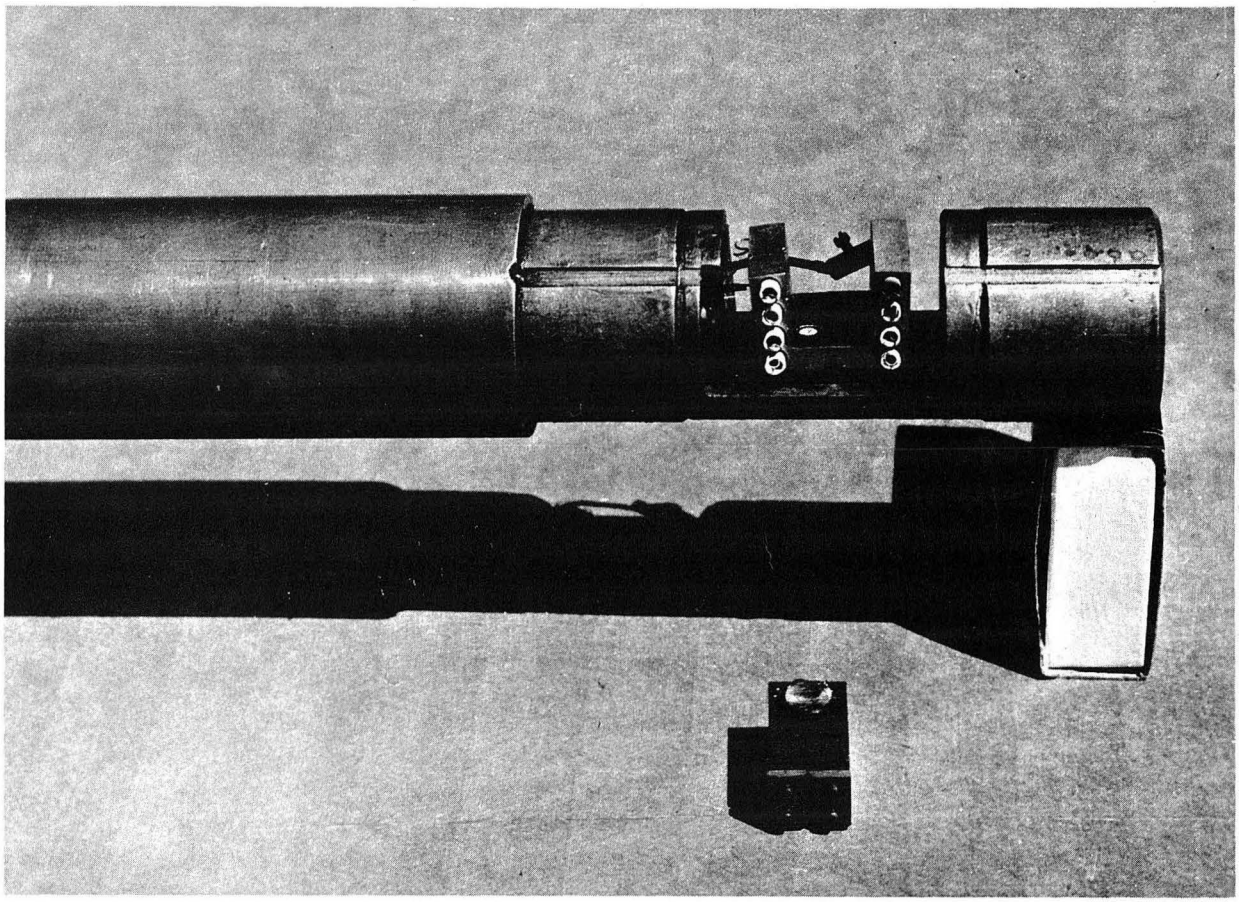

ZN-1719

Fig. 7. The resistance heated dry dock assembly.

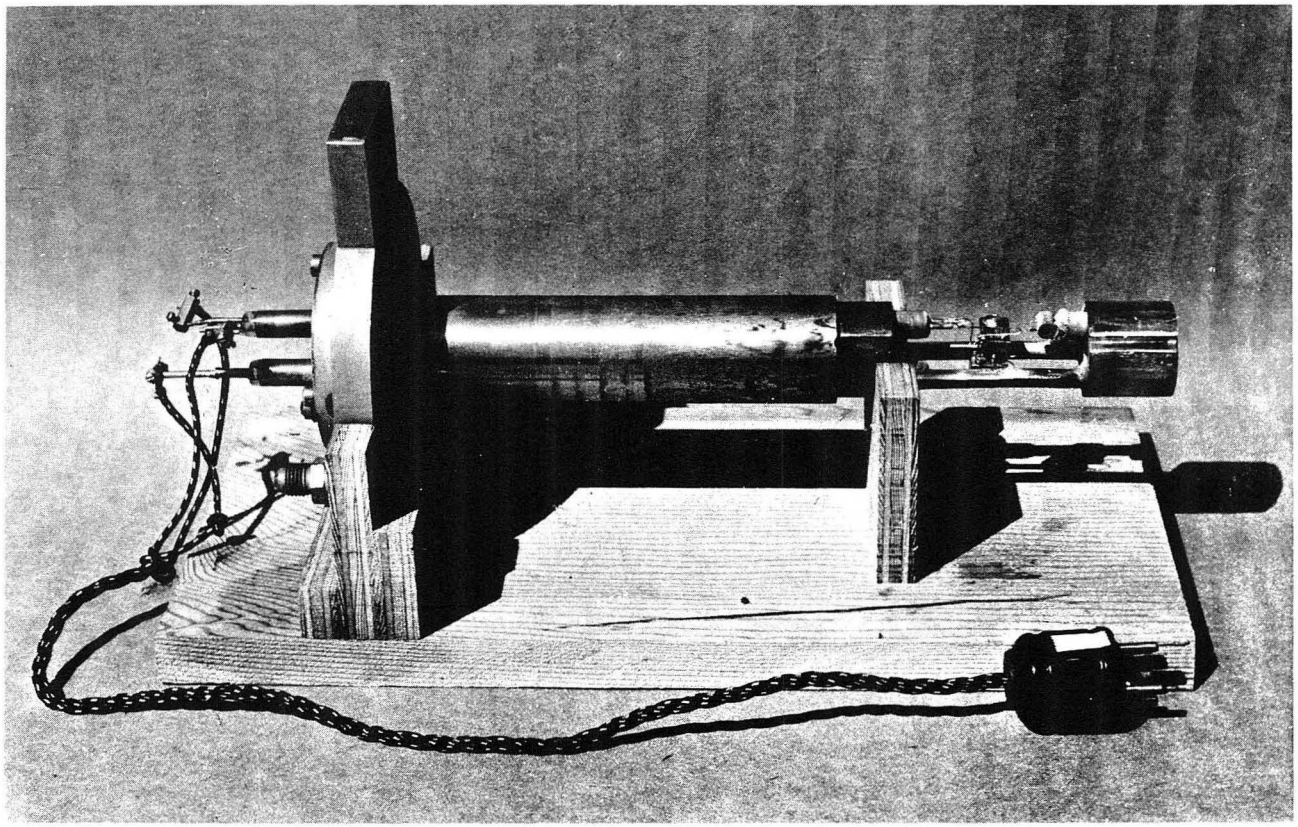

ZN-1720

Fig. 8. The electron bombardment oven loader.

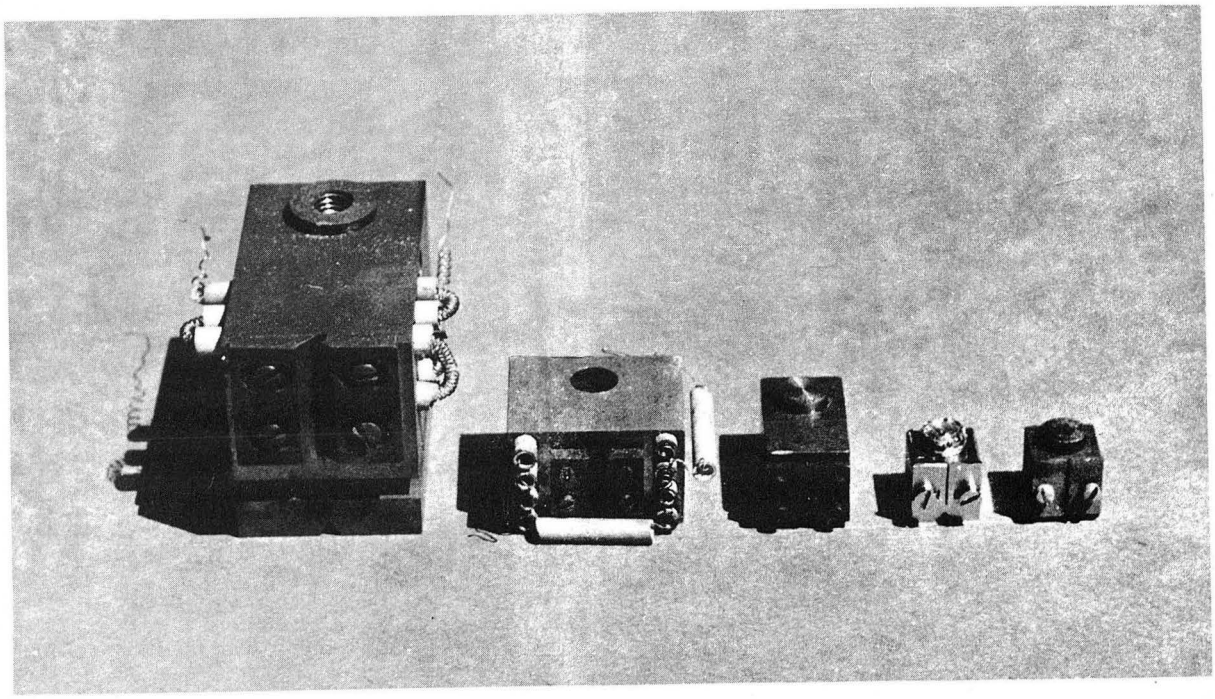

ZN-1721

Fig. 9. Various atomic beam ovens. They are from left to right: molecular beam oven; atomic beam zero moment oven; resistance heated dry dock oven; electron bombardment heated tantalum oven; electron bombardment heated carbon oven.

In this arrangement the oven, made either of tantalum or carbon, rests on three pins which are maintained at a positive potential with respect to the filament. The electrons are thermionically emitted from a .015-inch thoriated-tungsten filament which has undergone several carbonations with Aquadag. The carbonization process lowers the work function of the surface through the formation of thorium and tungsten carbides. It is accomplished by painting the filament with Aquadag and heating it in a vacuum until suitable emission characteristics are obtained. Typical carbonization currents of 12 amps in the .015 mil wire produced good emission after about one hour. Usually the filament current was lowered to 9 or 10 amps after carbonization to ensure long filament life. The accelerating potential is supplied by a full-wave rectifier, employing two type 866 mercury rectifiers (see Fig. 10). This supply is capable of delivering 500 ma at voltages up to 1000 volts. In practice, depending upon the geometry of the oven and filament, the ratio, emission current (ma) to voltage (v) varies from 2 to 1. While cesium beams are produced at low temperature with very low power (2 or 3 watts over filament radiation heating), temperatures as high as 2500°F have been obtained using a tantalum oven.

B. Internal Radiofrequency Coaxial Cable

The enormous variations observed by Sunderland (SUN 56A) in resonance height with frequency were attributed to resonances in the twisted pair lead which connected the hairpin to the vacuum seal on the "octagon" turret of the apparatus (see Fig. 11). These variations placed minima at 70 and 160 mc/sec. Because these minima were about twenty percent of the

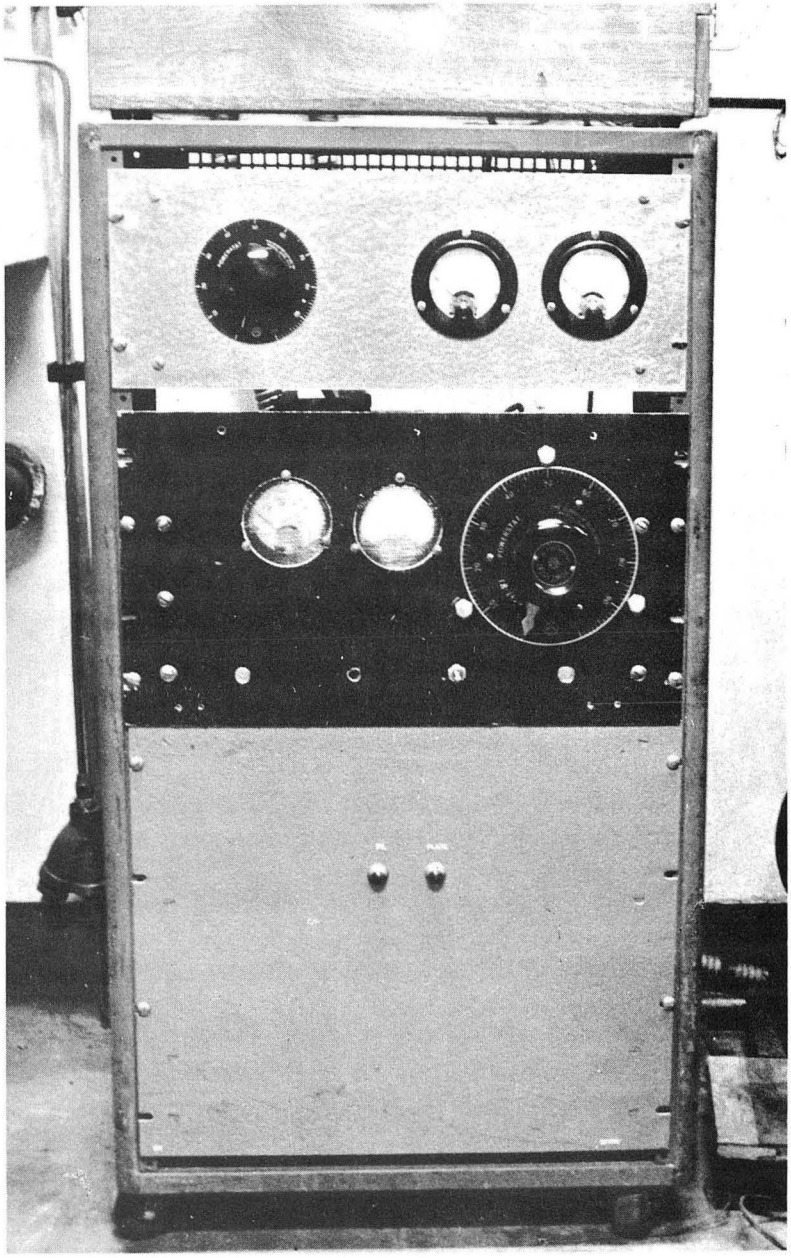

ZN-1722

Fig. 10. The 1000 v, 500 ma electron bombardment power supply.

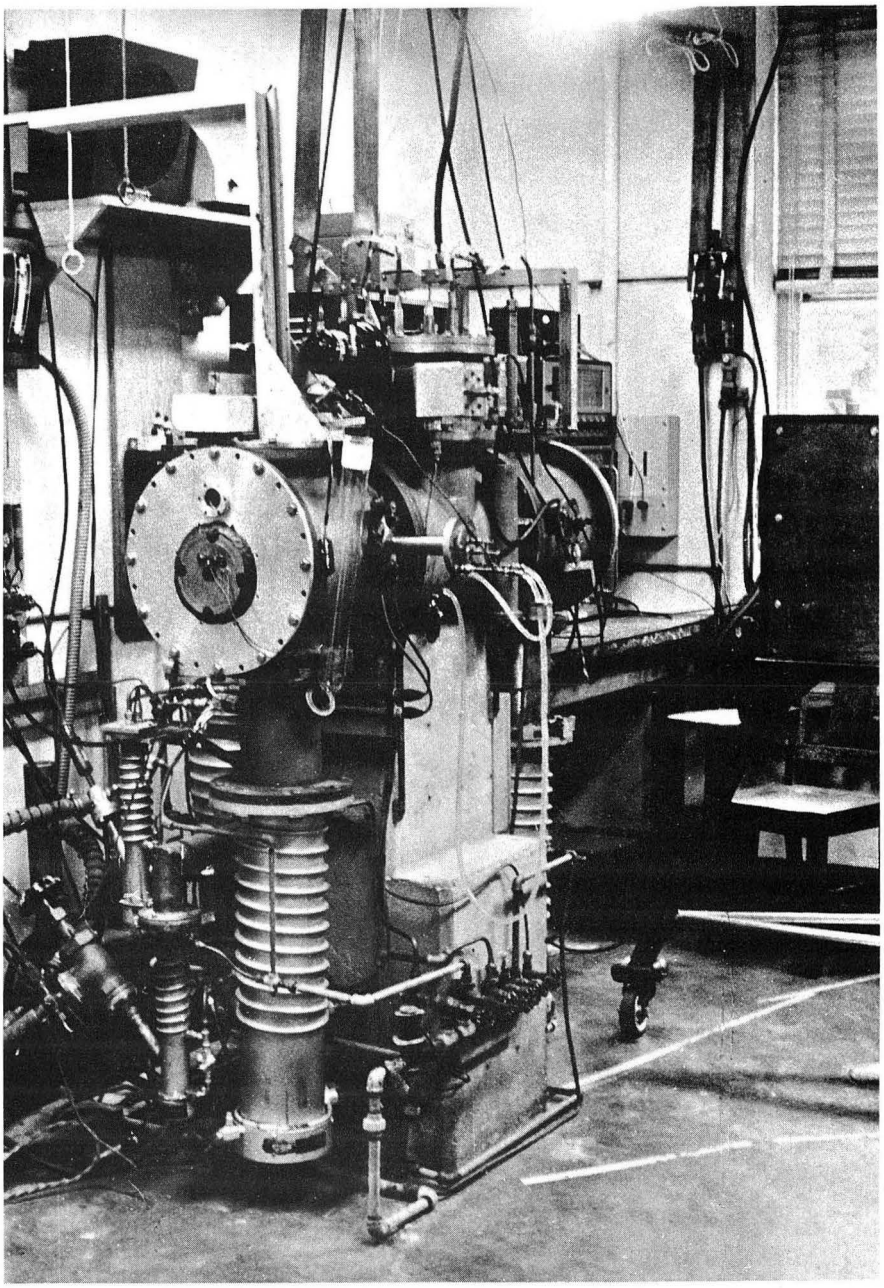

ZN-1723

Fig. 11. The atomic beam apparatus as seen from the oven end.

resonance height at intermediate frequencies, it was useless to attempt to see resonances between 60 and 80 mc/sec or above 130 mc/sec.

The twisted pair leads have now been augmented by a vacuum coaxial cable consisting of a flexible wire threaded through short sections of glass tubing, for insulation and spacing. This assembly was covered by flexible shielding to complete the cable. By this replacement, resonances are continuously observable up to ~ 200 mc, except where the radiofrequency affects the hot wire detector electrometer. The present behavior of the resonance height, as well as the regions of electrometer resonances, are given in Fig. 12. Presumably radioactive resonances could be observed in the regions of electrometer resonances, but effective calibrations using stable isotopes would be impossible in these regions.

C. Radiofrequency Hairpin

The theoretical resonance line width, $\delta\nu$, is related to the time, δt, which the atom spends in the transition field of an atomic beam apparatus by the relation derived by Torrey (TOR 41),

$$\delta\nu\delta t \approx 1.07. \qquad (24)$$

Thus, for a 1 cm hairpin, a cesium atom travelling with the most probable velocity spends about 34 microseconds in the transition region.

$$\delta t = \frac{\ell}{(2kT/m)^{1/2}} = 34 \times 10^{-6} \text{ sec}, \qquad (25)$$

where $\ell = 1$ cm; $T \approx 400^{\circ}C \approx 673^{\circ}K$; $k \approx 1.38 \times 10^{-16}$ erg/deg; $m \approx 2.2 \times 10^{-22}$ gms for Cs^{130}. According to Eq. (24), the line width at 1/2 maximum then

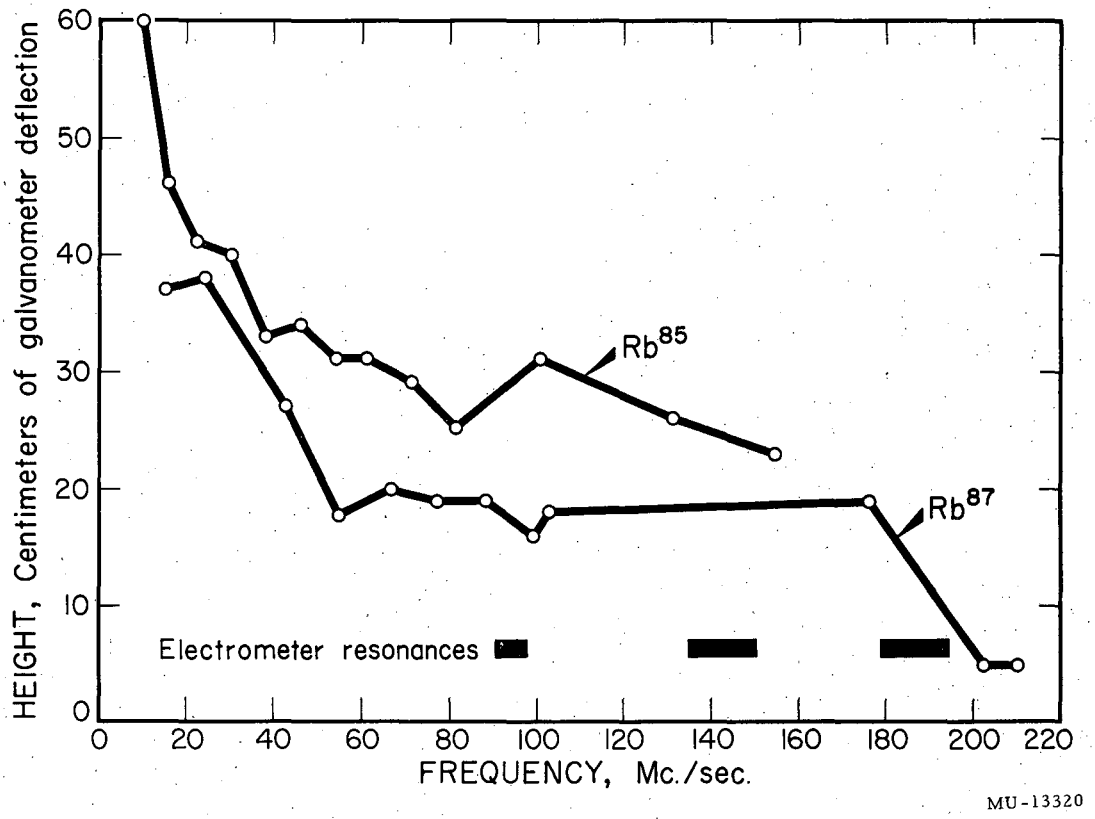

Fig. 12. Variation in resonance height with frequency using present radiofrequency equipment.

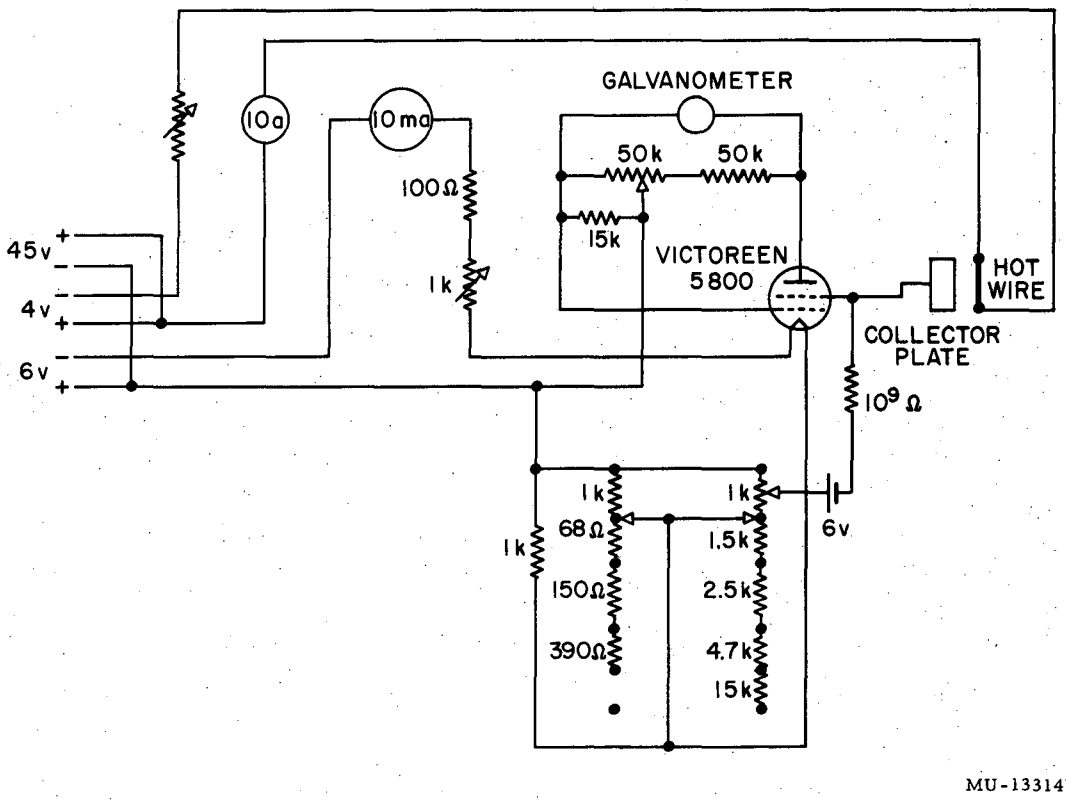

Fig. 13. Electrometer detector circuit.

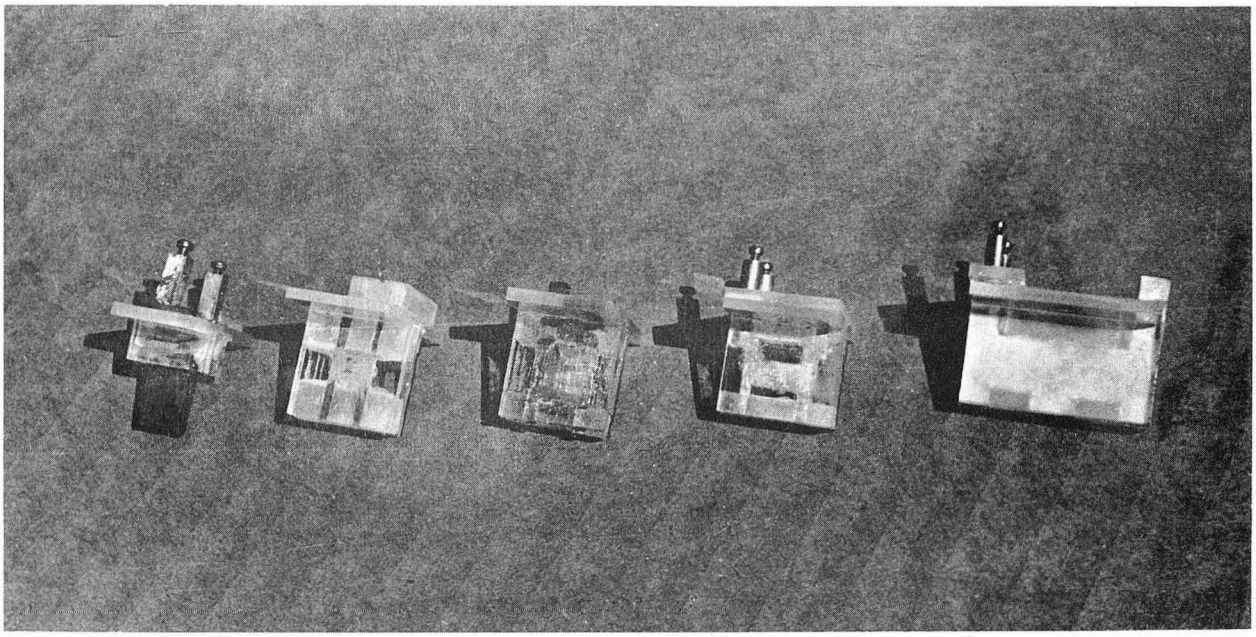

ZN-1724

Figs. 14a and 14b. Radiofrequency hairpins.

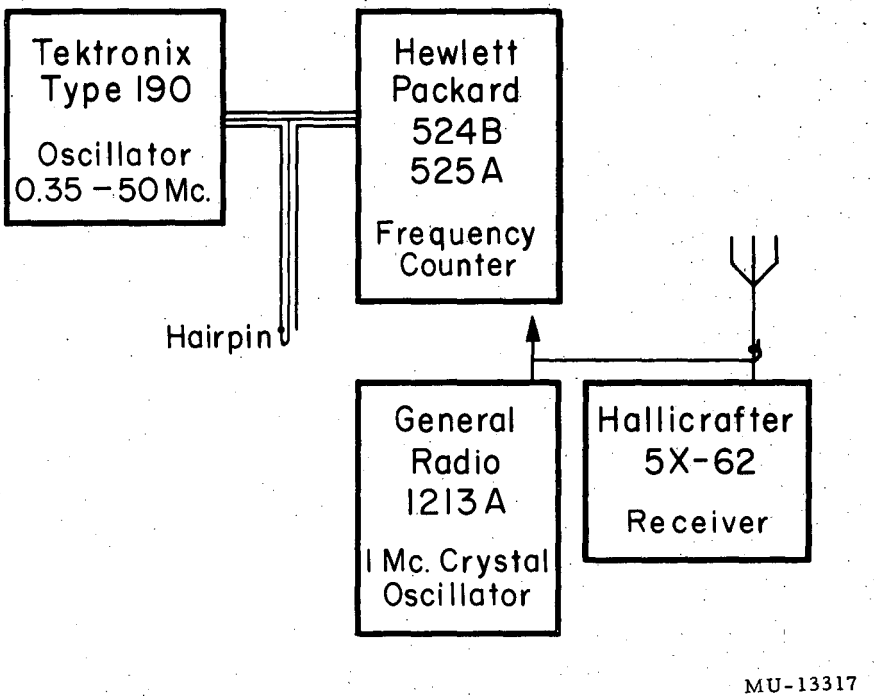

Fig. 15. Radiofrequency equipment (.35 to 20 megacycles per second)

becomes

$$\delta\nu \approx 1.07/\delta t \approx 32 \text{ kc}. \qquad (26)$$

Unfortunately, the observed line width with a 1 cm hairpin was often as much as 15 times this value. The large width was blamed on field inhomogeneities of the C field.

In an effort to reduce this enormous line width, a 1 cm hairpin was moved to different positions in the C field, but no reduction in width occurred. Ultimately the hairpin (see Figs. 14a and 14b) was replaced by one having a single loop of wire. This arrangement produces resonances which vary in width from 100 to 500 kc, depending upon the frequency. The line remains broad at frequencies below 10 mc and narrows at higher frequencies. The single loop wire hairpin represents a compromise between the broadening of the type given by Eq. (24) and broadening due to C field inhomogeneities.

D. Radiofrequency Equipment

The radiofrequency equipment used in the range of .35 mc/sec to .20 mc/sec is shown diagramatically by Fig. 15. The system consists of a Tektronix type 190 oscillator, shorted through the wire loop hairpin. The frequency is measured with a Hewlett-Packard 524B-525A frequency counter, which counts directly the cycles during a known period set by an internal 100 kc crystal. The 100 kc crystal was frequently compared with a General Radio 1213A, 1 mc crystal oscillator. At longer intervals, both crystal oscillators were compared with the 5 and 10 mc transmission of the Bureau of Standards station, WWV, received on a Hallicrafter SX-62 receiver. In

this manner an accuracy of at least 1 part in 10^5 was maintained in all frequency measurements. The maximum error at the highest frequency used would amount to 2 kc/sec out of 200 mc/sec. Since the frequency measuring error was usually much smaller than the stated maximum and much larger errors arise in locating resonance peaks, all errors in stated frequencies arise from resonance peak placement.

Higher frequencies (10 to 200 mc/sec) were generated by a Hewlett-Packard 608A, 10 to 500 mc/sec oscillator (see Figs. 16 and 17). The output was amplified by two Hewlett-Packard 460B wide band amplifiers in cascade. These amplifiers provide effective amplification up to approximately 200 mc/sec. The higher frequencies (10 to 200 mc/sec) utilize supplementary Hewlett-Packard 525A and B plug-in mixers for the frequency measurements. The response of the resonance to the maximum radiofrequency power attainable with the equipment is given in Fig. 12.

E. Counting Equipment

The low background, x-ray scintillation counters used in these experiments have been described in detail by Sunderland (SUN 56A). Their virtue lies in good counting geometry, good counting efficiency and very low background. The buttons, as they come from the atomic beam apparatus, are covered with a single layer of Scotch tape to prevent loss of the accumulated activity and inserted in the bottom of the counter housing. Immediately above the sulfur surface and safety piece of Scotch tape is a window of .001-inch aluminum. Next a 1/4" x 3/4" x 2 mm sodium iodide, thallium activated crystal rests on the aluminum foil. The crystal area is only

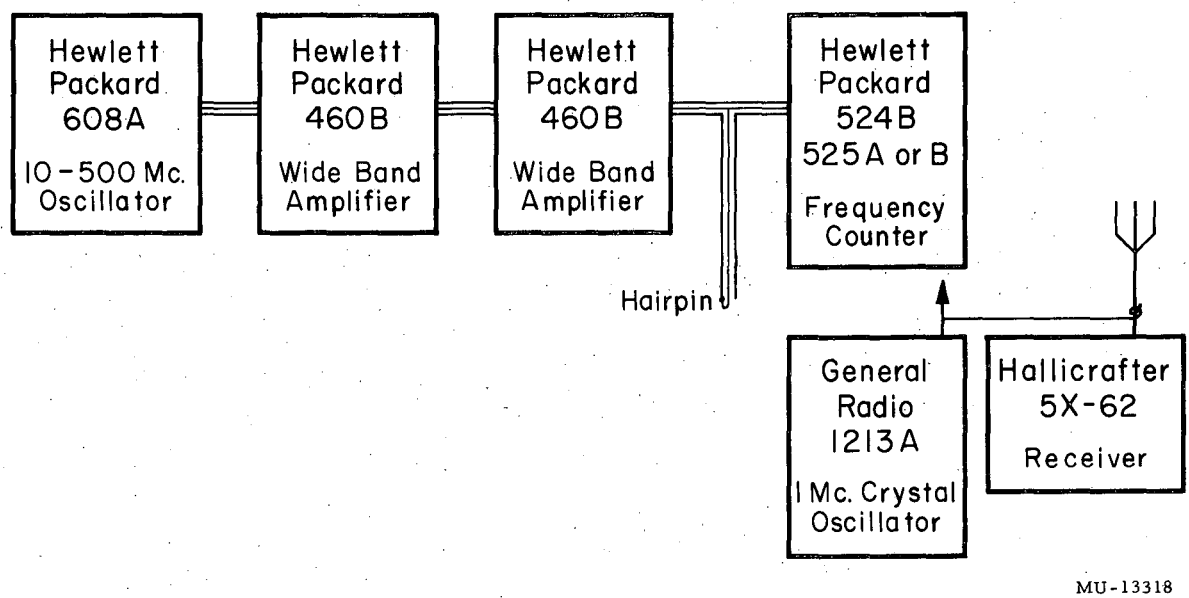

Fig. 16. Radiofrequency equipment (10 to 200 megacycles per second)

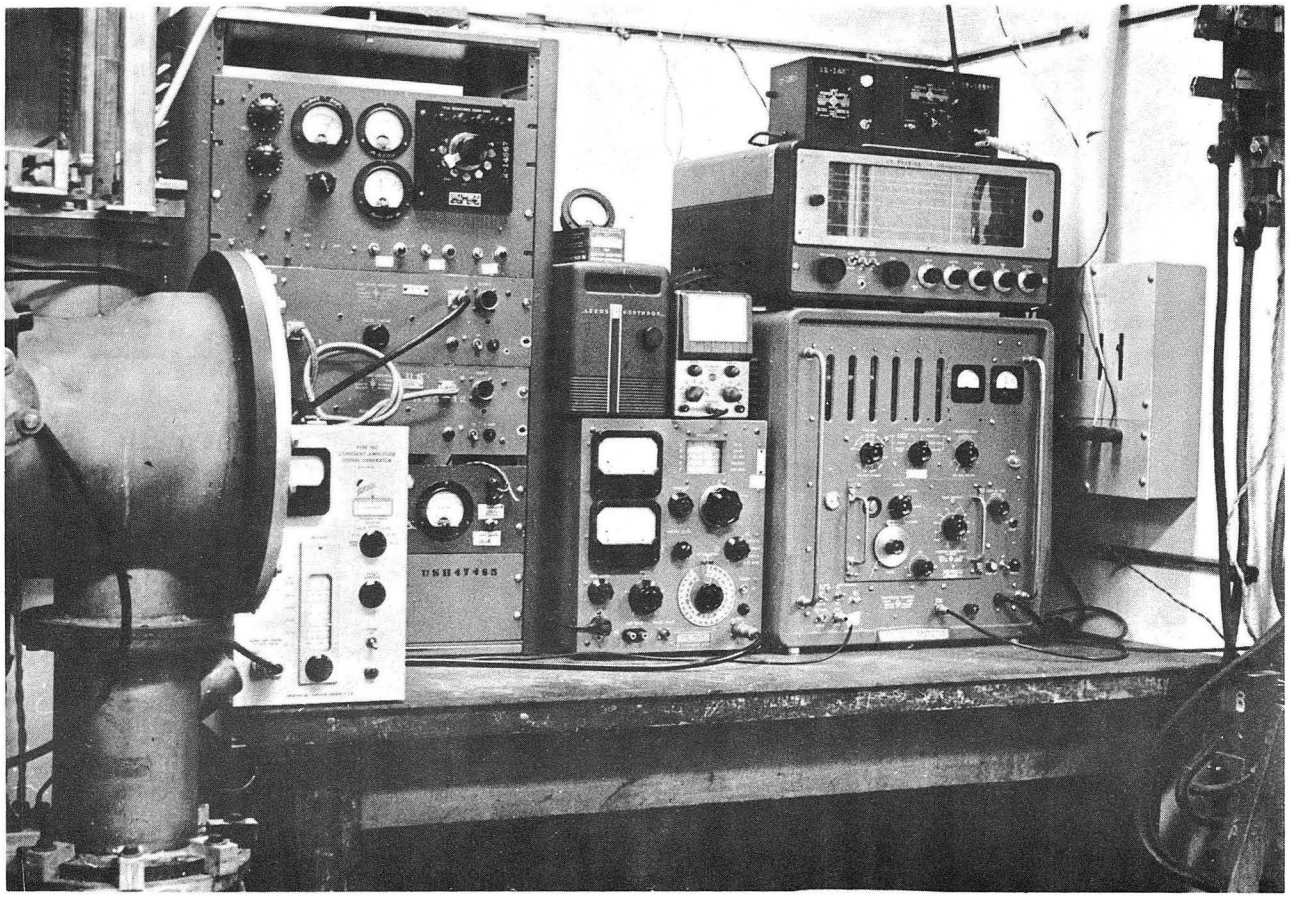

ZN-1725

Fig. 17. The radiofrequency equipment.

slightly larger than that of the button. Finally, a type 6655, 10 stage, photomultiplier tube rests against the sodium iodide crystal. The surrounding space is filled with anhydrous mineral oil to insure good optical contact and also to protect the crystal from the deteriorating effects of moisture. The photomultiplier pulses were fed into preamplifiers with a gain of about 30 and then into differential pulse height analysers and scalers of the type described in UCRL report 2083. Figs. 18 and 19 show some of the counting equipment components.

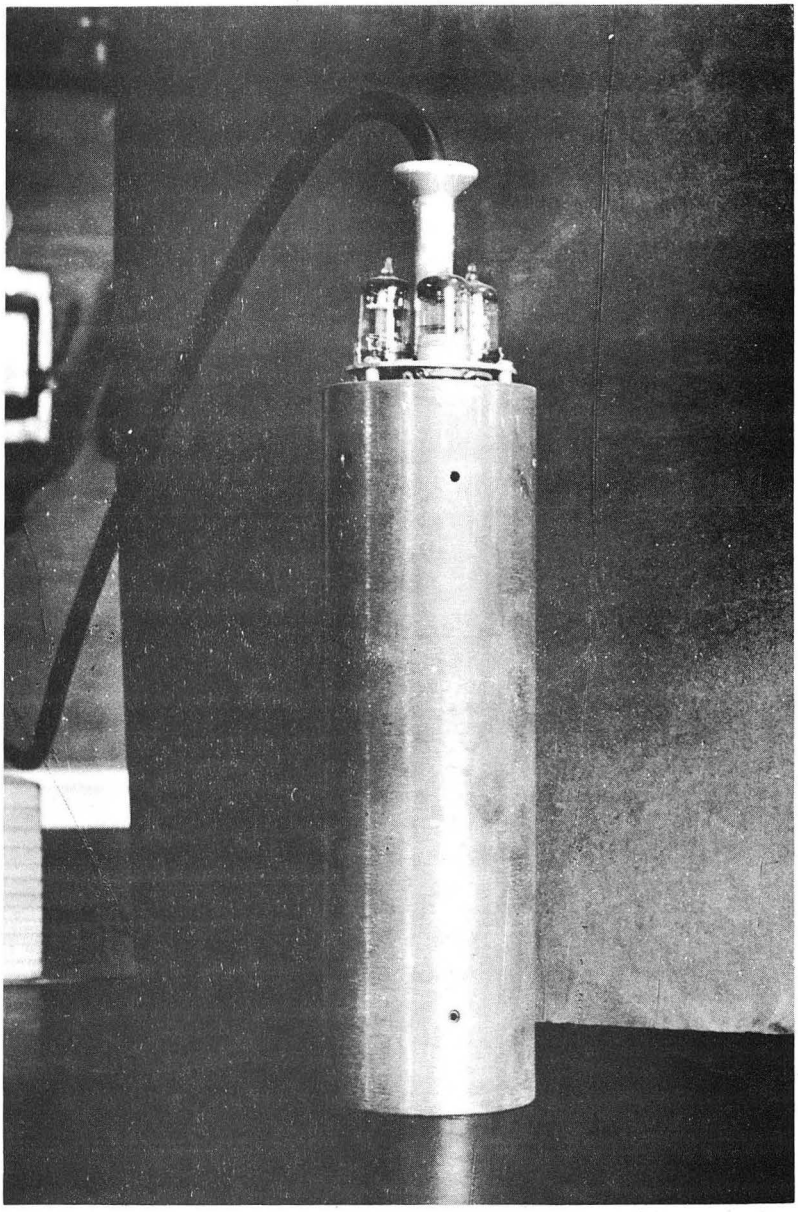

ZN-1726

Fig. 18. An assembled X-ray scintillation counter.

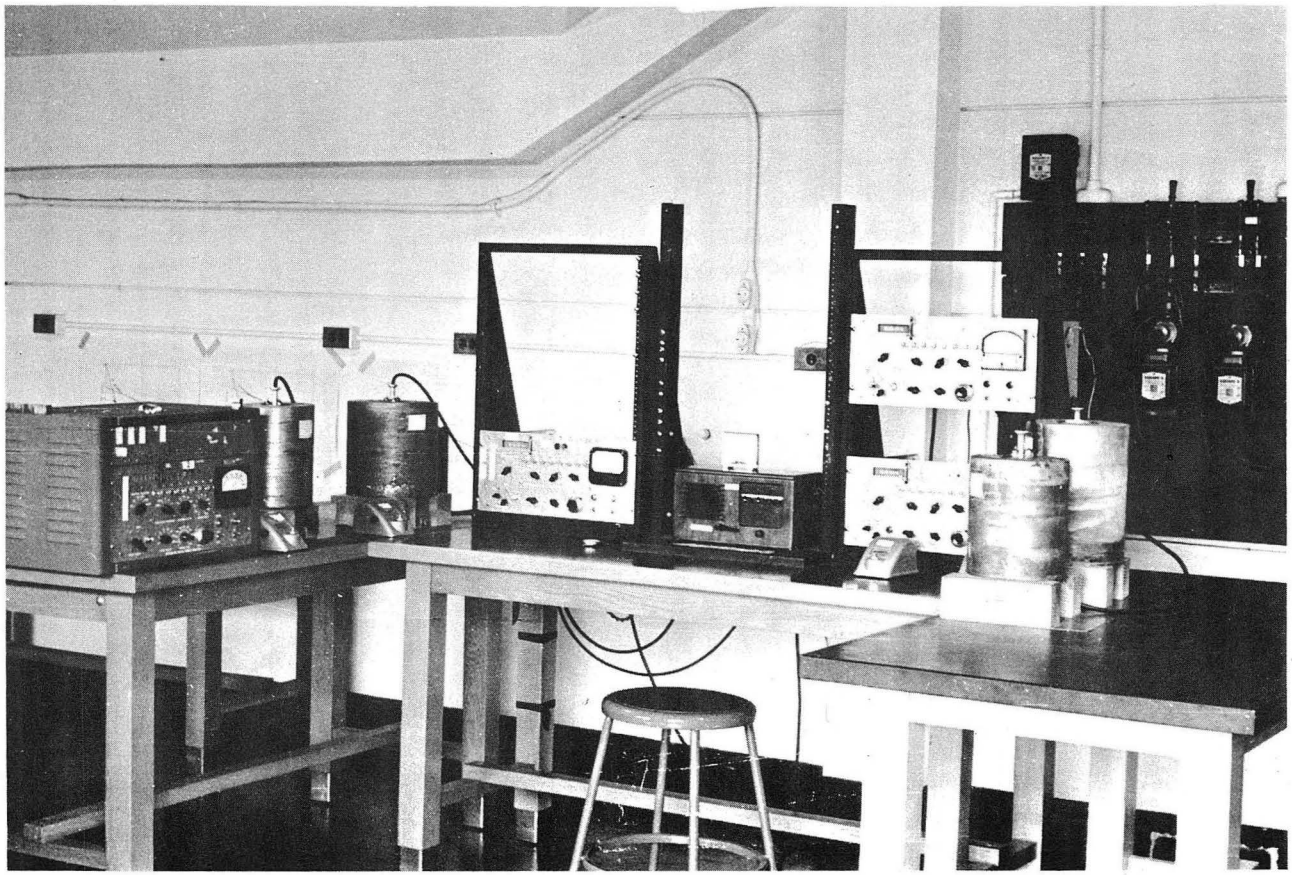

ZN-1727

Fig. 19. The counting equipment.

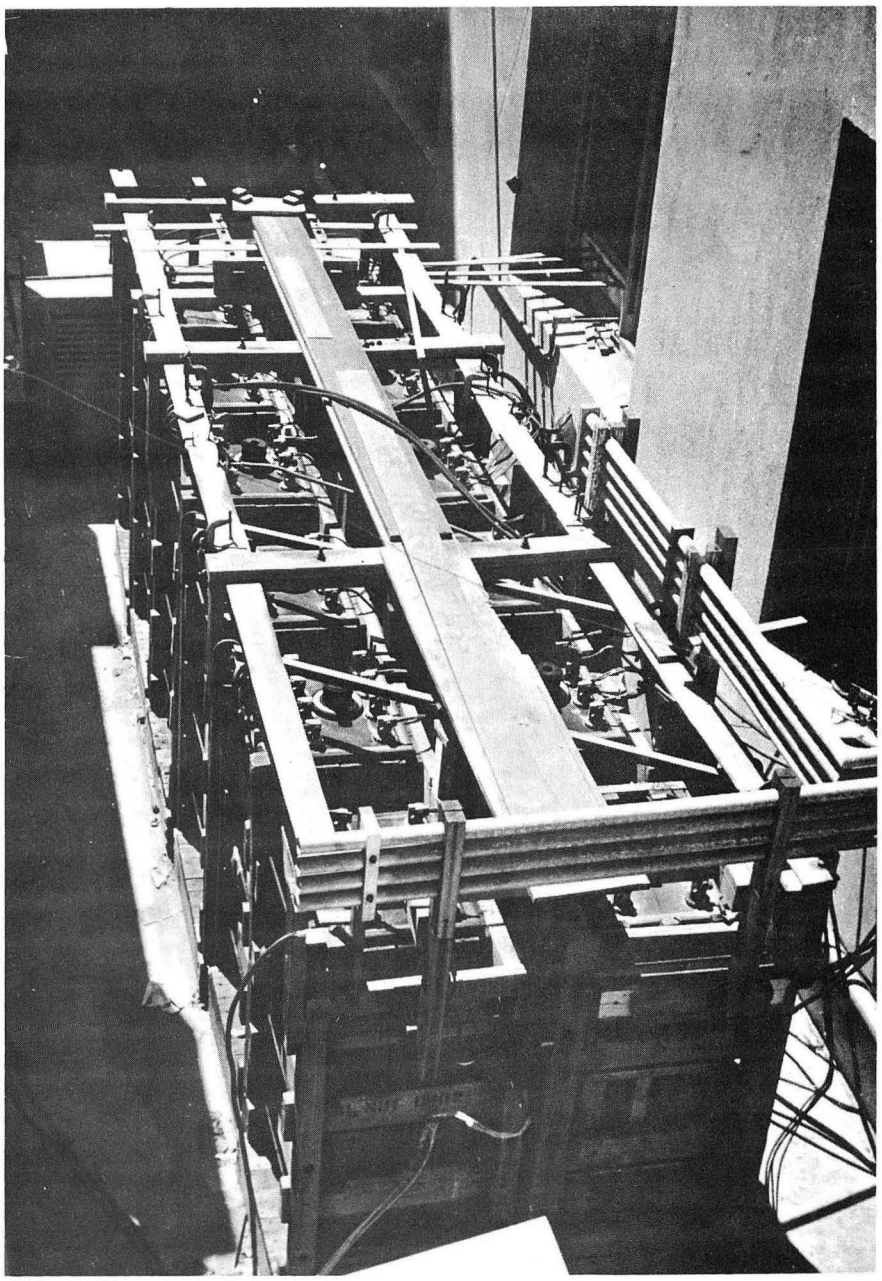

ZN-1728

Fig. 20. The 20,000 ampere-hour submarine storage batteries, which energize the A and B magnets.

IV. ISOTOPE PREPARATION

A. The I(α,kn)Cs Reactions

Three of the neutron deficient isotopes, Cs^{127}, Cs^{129}, and Cs^{130}, were produced by 45.5 Mev alpha-particle bombardment of I^{127} in the form of BaI_2. The specific reactions are $I^{127}(\alpha,n)Cs^{130}$, $I^{127}(\alpha,2n)Cs^{129}$, and $I^{127}(\alpha,4n)Cs^{127}$ (FIN 50, SMI 52). The $I^{127}(\alpha,3n)CS^{128}$ reaction occurs, but the cesium quickly decays with a half-life of 3.8 minutes to a stable xenon isotope.

Alpha neutron nuclear reactions are often treated by the compound nucleus and neutron evaporation models (EVA 55, BLA 52, FER 50). By this model, the alpha-particle penetrates the coulomb barrier of the iodine nucleus and forms an excited or compound nucleus of cesium. When sufficient energy of excitation is concentrated on a single neutron, it may escape from the nucleus. As the bombarding energy is increased, the compound nucleus, after emitting one neutron, may still contain enough energy to emit a second and possibly even a third or fourth neutron. Discrete thresholds exist for the various α,kn reactions. For alpha-particle energies below the threshold value, the probability of obtaining a given reaction becomes zero. On the other hand, if the alpha-particle energy is too high, the probability of emission of a multiple number of neutrons is so large that the probability of emitting a single neutron drops in significance.

An understanding of the threshold and shape of the cross section curves or excitation functions for the α,kn reactions permits some flexibility in controlling the relative production rates of the various isotopes. Threshold energies have been measured by several authors for Ag(α,kn)In,

In(α,kn)Sb, and Bi(α,kn)At reactions (GHO 48, TEM 49, BLE 53, KEL 47, 47A). The reaction thresholds for iodine α,kn reactions are probably quite similar to those of indium α,kn reactions. Temmer (TEM 49) gives the following values for indium:

Reaction	Threshold
$In^{115}(\alpha,n)Sb^{118}$	13 Mev
$In^{115}(\alpha,2n)Sb^{117}$	18 Mev
$In^{115}(\alpha,3n)Sb^{116}$	27 Mev

Each of these values is about 2 Mev higher than the thresholds assumed by Doggett in his calculations of the Br(α,kn)Rb excitation functions (DOG 56). Therefore it is reasonable to assume a threshold of ~36 Mev for the α,4n reaction. The above-mentioned thresholds for indium are the ones assumed for the I(α,kn)Cs reactions. With these values to predict required thicknesses of targets and absorbers, certain reactions may be selectively enhanced. For example, in an experiment on Cs^{130}, the Cs^{127} and Cs^{129} production may be lowered by degrading the alpha beam to ~18 to 20 Mev. In this way only the $I^{127}(\alpha,n)Cs^{130}$ reaction is probable, and little Cs^{127} and Cs^{129} are made. As another example, Cs^{127} may be selectively produced over Cs^{129} by making the target so thin that the alpha-particles still possess ~36 Mev as they leave the powder. Here the Cs^{127} is still produced, but some of its production, which would have occurred for alpha-particles in the range of 27 to 36 Mev, is eliminated.

B. The Xe(p,n)Cs Reactions

The second way cesium radio-isotopes were produced was through 12 Mev proton bombardment of normal xenon gas. Atmospheric xenon consists of nine known stable isotopes in widely different abundances. Because the proton, neutron reaction threshold is ~6 Mev in xenon and the energy of the available protons is low (12 Mev), only the p,1n reaction in xenon occurs. Therefore the following reactions are possible:

Xenon Abundance	Reaction	Cesium Half-Life
.094%	$Xe^{124}(p,n)Cs^{124}$	unknown
.092	$Xe^{126}(p,n)Cs^{126}$	1.6 m
1.92	$Xe^{128}(p,n)Cs^{128}$	3.8 m
26.4	$Xe^{129}(p,n)Cs^{129}$	31 hr
4.1	$Xe^{130}(p,n)Cs^{130}$	30 m
21.2	$Xe^{131}(p,n)Cs^{131}$	9.7 d
26.9	$Xe^{132}(p,n)Cs^{132}$	6.2 d
10.4	$Xe^{134}(p,n)Cs^{134}$	2.3 yr and 3.1 hr
8.9	$Xe^{136}(p,n)Cs^{136}$	13 d

Of these reactions, only Cs^{129}, Cs^{131}, and Cs^{132} are produced during a two-hour bombardment in sufficient quantity to be useful for measurements in the atomic beam apparatus. The production of Cs^{136} is marginal. As a result, Cs^{129}, Cs^{131}, Cs^{132} resonances have been observed after producing them by this method. A hint of a Cs^{136} resonance has appeared twice, but definite establishment of this resonance must await arrival of xenon enriched in the 136 mass isotope. Since both of the above production

schemes produce Cs^{129}, either form of production may be used for this isotope. Resonances have been observed for Cs^{129} produced by both methods.

C. The Powder Target

Fig. 21 shows the aluminum disk and covers used in the bombardment of powders. The three powder grooves are each about 1/8 inch wide and 2 inches long. Only a thin aluminum vane separates adjacent grooves and serves to conduct heat away from the powder. The depth of the grooves varied from ten to fifty thousandths of an inch, depending on the isotopes being produced. Aluminum foils were placed directly over the powder, and they were held in place by the cover which in turn was fastened to the aluminum disk by screws.

Several attempts to remove moisture from the barium iodide target at about three hundred degrees centigrade resulted in the formation of a white cake, which was insoluble in water. Likewise, iodine was evolved during the process. Placing the target in a good vacuum for ten minutes also resulted in the formation of large quantities of seemingly insoluble material. Finally, a baking procedure at sixty to eighty degrees centigrade was adopted to prevent this loss of iodine and to insure that the powder was an anhydrous as possible. All of these target experiments were performed before the first bombardment, so no difficulties were later encountered.

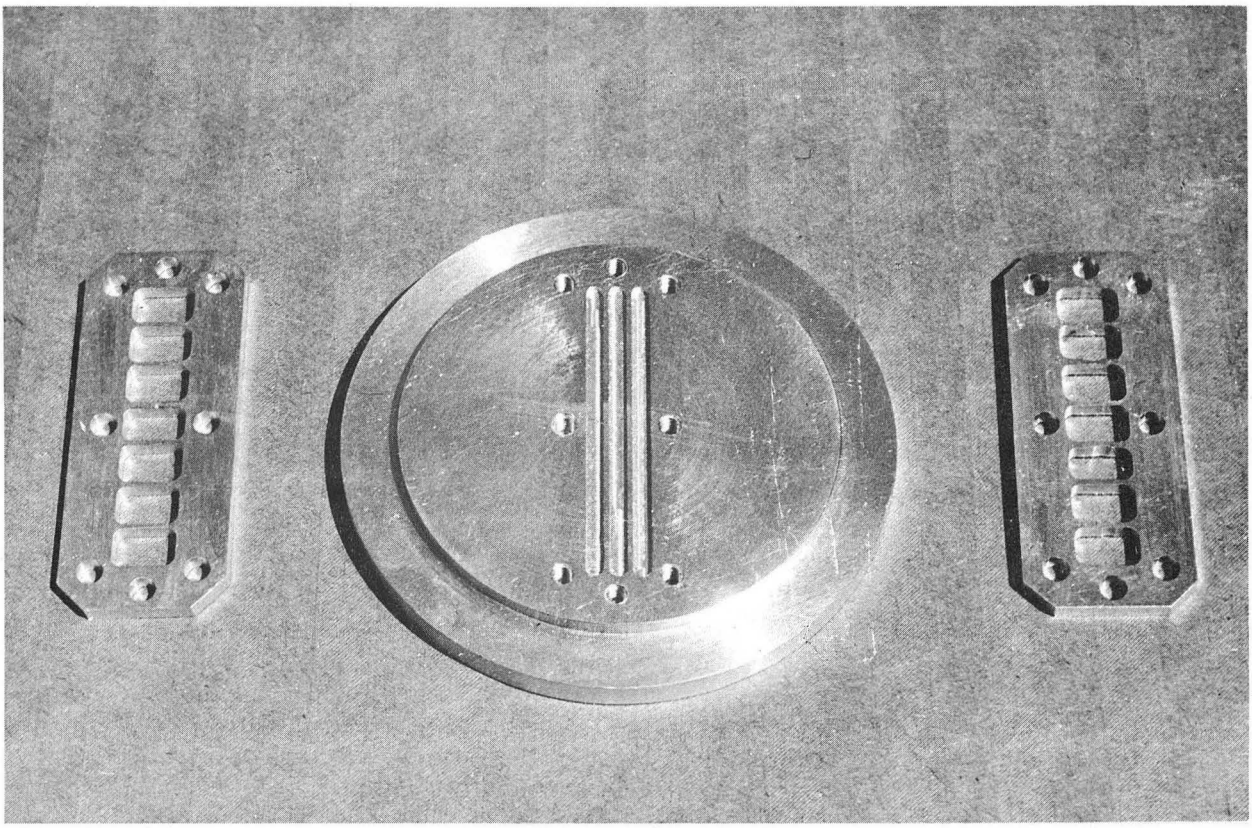

ZN-1729

Fig. 21. The powder cyclotron target.

D. The Xenon Target

Fig. 22 shows the container (bell jar) in which xenon gas was bombarded with protons of ~ 12 Mev energy. The bell jar was borrowed from Miss Kwan Hsu, who uses it in the preparation of isotopes for medical purposes. With external dimensions of 18 to 19 × 5 × 1-1/2 inches, the cast aluminum container has an internal volume of 2160 cubic centimeters. It is cooled by water circulating through copper tubing welded externally around the chamber. Attached to the chamber is the window assembly which contains two one-thousandths of an inch thick aluminum foils to partition the gas from the cyclotron vacuum. Thus the proton beam passes from the cyclotron vacuum through a one-mil foil into an air space maintained at a pressure of half an atmosphere. After traversing half an inch of air, the protons pass through another one-mil foil to enter the xenon region.

The Bragg-Kleeman rule (see EVA 55, p. 653) for the proton range in a substance compared to the proton range in air is good to about fifteen percent:

$$\text{Range in substance} = 3.2 \times 10^{-4} \frac{(A)^{1/2}}{\rho} \times \text{range in air}, \quad (27)$$

where A is the atomic weight of the substance, and ρ is the density of the substance in grams per cubic centimeter. With the density of xenon, A, set equal to 132, and the range energy relationship for protons in dry air given by Bethe (EVA 55, p. 65), the Bragg-Kleeman rule predicts a range of ~ 11 centimeters in xenon per Mev of proton energy between 11 and 5 Mev. At this rate, the protons would lose about 4 Mev in the xenon before hitting the end of the bombardment chamber. Taking into account the loss of about 1 Mev in traversing two mils of aluminum and half an inch of air

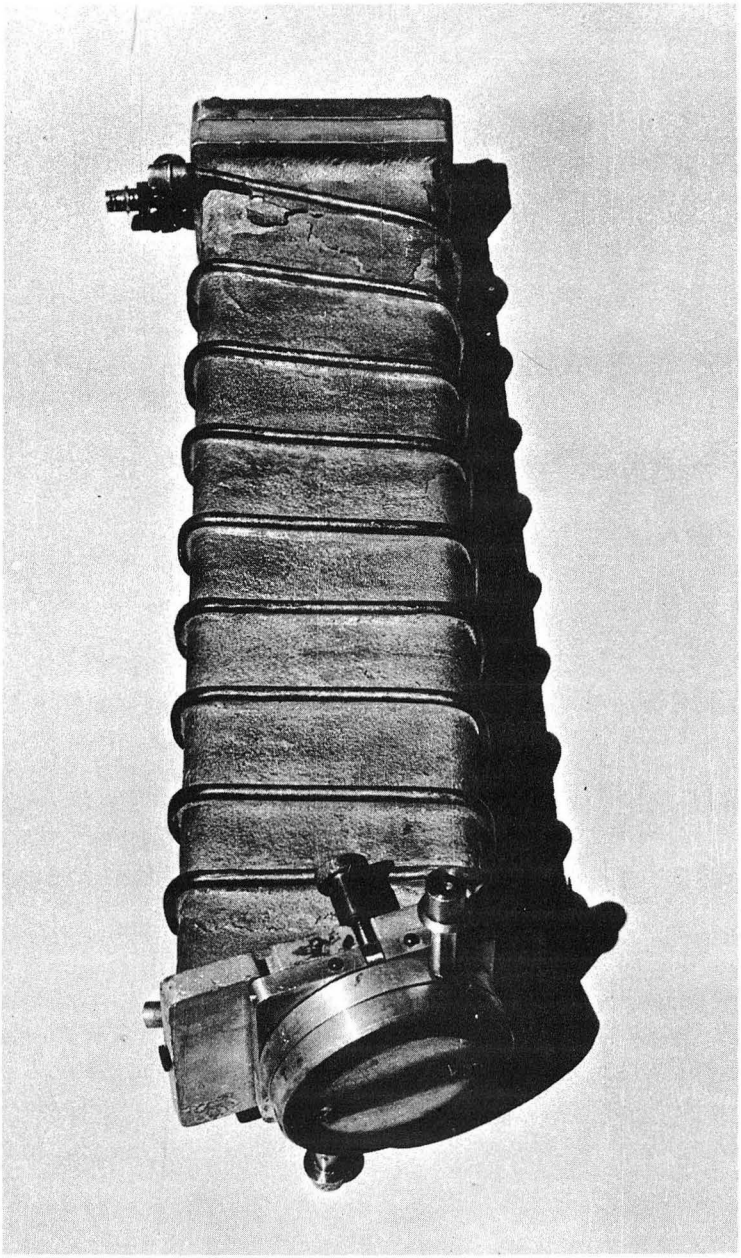

ZN-1730

Fig. 22. The bell jar used to bombard gaseous xenon with protons.

at half an atmosphere, the protons enter the xenon at 11 Mev and leave at 7 Mev. This energy range extends from 1 Mev above the threshold for the proton, neutron reaction to the highest energy, external proton beam available from the sixty-inch cyclotron. This arrangement thus utilizes the xenon with maximum efficiency.

E. Barium Iodide Chemistry

Because the cesium isotopes in these experiments were produced from two different elements, two distinct chemical procedures provided the necessary separation of the desired radio-isotopes from the bombarded or target material. One chemical procedure, involving several steps, isolated the cesium isotopes from barium iodide, BaI_2; while the other removed the cesium from the gaseous xenon target.

Following closely the chemistry used by Hobson, Hubbs, and Sunderland (HOB 54A, HUB 54, SUN 56A), several trial attempts to perform a similar procedure, using cesium in place of rubidium and barium iodide in place of barium bromide, gave encouraging results. The procedure, which was originally developed by Hobson, when translated to work for cesium, is as follows.

Approximately 100 to 200 milligrams of barium iodide, containing about 10^{10} to 10^{14} radioactive cesium atoms, are dissolved in 200 cubic centimeters of water containing controlled amounts of carrier cesium iodide (usually 5 to 50 milligrams). The barium iodide is washed directly from the target grooves into a beaker by a three foot long pipette, which permits the operator to remain at least three feet from the target. Next,

an excess of ammonium carbonate precipitates the barium as barium carbonate. This leaves ammonium iodide and cesium iodide in solution. After the solution is filtered to eliminate any suspended barium carbonate, the ammonium iodide and cesium iodide are concentrated by boiling the solution to dryness. There has been no evidence of any cerium activity following the cesium; so it is assumed that the cerium, produced by alpha-particles on barium, follows the barium and is precipitated as a carbonate.

Upon heating, the dry ammonium iodide sublimes, while the cesium iodide remains on the container walls. This occurs because at atmospheric pressure the sublimation temperature of ammonium iodide (551°C) and the boiling point of cesium iodide (1280°C) are separated by 729°C. In the rubidium chemistry, this separation is 800°C. Several trial experiments showed that most of the ammonium iodide could be removed without loss of significant amounts of cesium. In a vacuum the sublimation could be carried out at ~ 220°C, but the resulting complication in the chemistry apparatus seemed unwarranted.

After the sublimation, the radioactive cesium iodide, along with the stable carrier cesium iodide, is dissolved in ~ .2 cubic centimeters of distilled water and transferred to a small iron oven cup with a 25 λ pipette. The iron oven cup sits on an aluminum plate which receives heat from a steam bath. Also to hasten the evaporation of the water from the oven cup, a stream of air and an infrared heat lamp play upon it. In this way, the evaporation proceeds at the rate of about 10λ per minute without boiling. Boiling must be avoided to prevent splattering the radioactivity outside the oven cup.

Using radiation readings taken throughout the chemical separation, the overall recovery approached 50 to 80 percent, depending upon the time and care given to the procedure. During the runs of short-lived activities (30 minute half-life), some sacrifice in efficiency was made in order that the chemistry could be completed before too many half-lives elapsed. In this way, the entire chemistry was often performed in 45 to 75 minutes during the Cs^{130} runs. On the other hand, 2 or 3 hours were often consumed when working with the longer-lived activities.

F. The Xenon Chemistry

The xenon chemistry is appealing due to its simplicity. After a bombardment, the xenon contained in the target is recovered by transferring the gas to a two-liter glass bulb. This is accomplished by simply connecting the two vessels and immersing the glass bulb in liquid nitrogen. The xenon quickly condenses as a solid in the glass bulb. Within the sensitivity of ~ 1 milliroentgen per hour, no activity appears to follow the xenon during this transfer procedure. This indicates that most of the cesium produced during the bombardment has migrated and stuck to the walls of the bell jar assembly.

Next, using the vacuum existing in the bell jar, 100 to 200 cubic centimeters of water containing 5 to 50 milligrams of cesium iodide carrier and a trace of hydroiodic acid are drawn into the system. Vigorous shaking of the assembly enables the water to reach all sections of the container. Usually three washings are sufficient to remove ninety percent of the activity. Although very efficient, this method involves large quantities

of water and consequently requires long times for concentrating the resulting solution before placing it in the atomic beam oven cup. However, most of the isotopes produced by the xenon target are long-lived, and a long time spent in chemistry is tolerable.

G. Oven Chemistry

After the oven cup containing dried cesium iodide is placed in the oven well, an excess of sodium-free calcium is added. Presumably the calcium reacts with the cesium iodide according to the reaction:

$$Ca + 2CsI \rightarrow 2Cs + CaI_2.$$

The calcium iodide remains in the oven, while the cesium, which has a higher vapor pressure, leaves the oven as an atomic beam. This reaction works as well for cesium iodide as it does for rubidium bromide. The resulting beam of cesium atoms is at least 90% atomic as measured by the ability of the inhomogeneous magnetic fields to deflect atoms away from the detector.

H. Radiation Safety

Except for washing the powder targets, all of the chemistry was performed behind two-inch lead bricks and a three-inch lead glass shield in a forced draft hood. Because of the relatively large activities (up to 50 roentgens per hour at 6 inches) used in these experiments, the entire operation was monitored by U.C.R.L. health chemists. Palm badges, film badges, and dosimeters worn during the chemistry and during subsequent running time usually indicated radiation doses of less than 100 milliroentgens per run.

V. EXPERIMENTAL PROCEDURE

After the chemistry described in Section IV is completed, the atomic beam oven is inserted in the apparatus by the method described in detail by Sunderland (SUN 56A). By this method the oven slips in a drydock (see Figs. 6 and 7) which contains the heating coils. This assembly then is pushed into a hollow sleeve which is closed at the opposite side. The sleeve and the oven loader assembly then comprise a continuous bar ~ 1.5 inches in diameter, which may be pushed back and forth horizontally through the center of the apparatus (see Fig. 23). Meanwhile, the internal vacuum is preserved by O-rings on either side of the apparatus. The electron bombardment loader operates in a similar manner.

The placement of the oven loader and oven is reproducible to within a few thousandths of an inch, and only slight adjustment is necessary after a beam is obtained. Adjustments are made by a calibrated screw which accurately controls the relative position of the oven loader with respect to the vacuum housing. Slight vertical adjustments may be made by rotating the entire oven assembly. All of these line-up procedures are accomplished using the stable carrier cesium beam. Next the magnetic fields are energized to determine the throw-out ability of the deflecting fields. This gives a measure of the atomic content of the beam. For cesium, in the experiments presented here, about 85 to 95 percent of the particles were defocused or deflected away from the detector by the inhomogeneous fields. The stop wire eliminates essentially all of the atoms or molecules which are not thrown out by the magnets. With the stop wire in place, usually less than .1% of the full beam reaches the detector. These atoms presumably

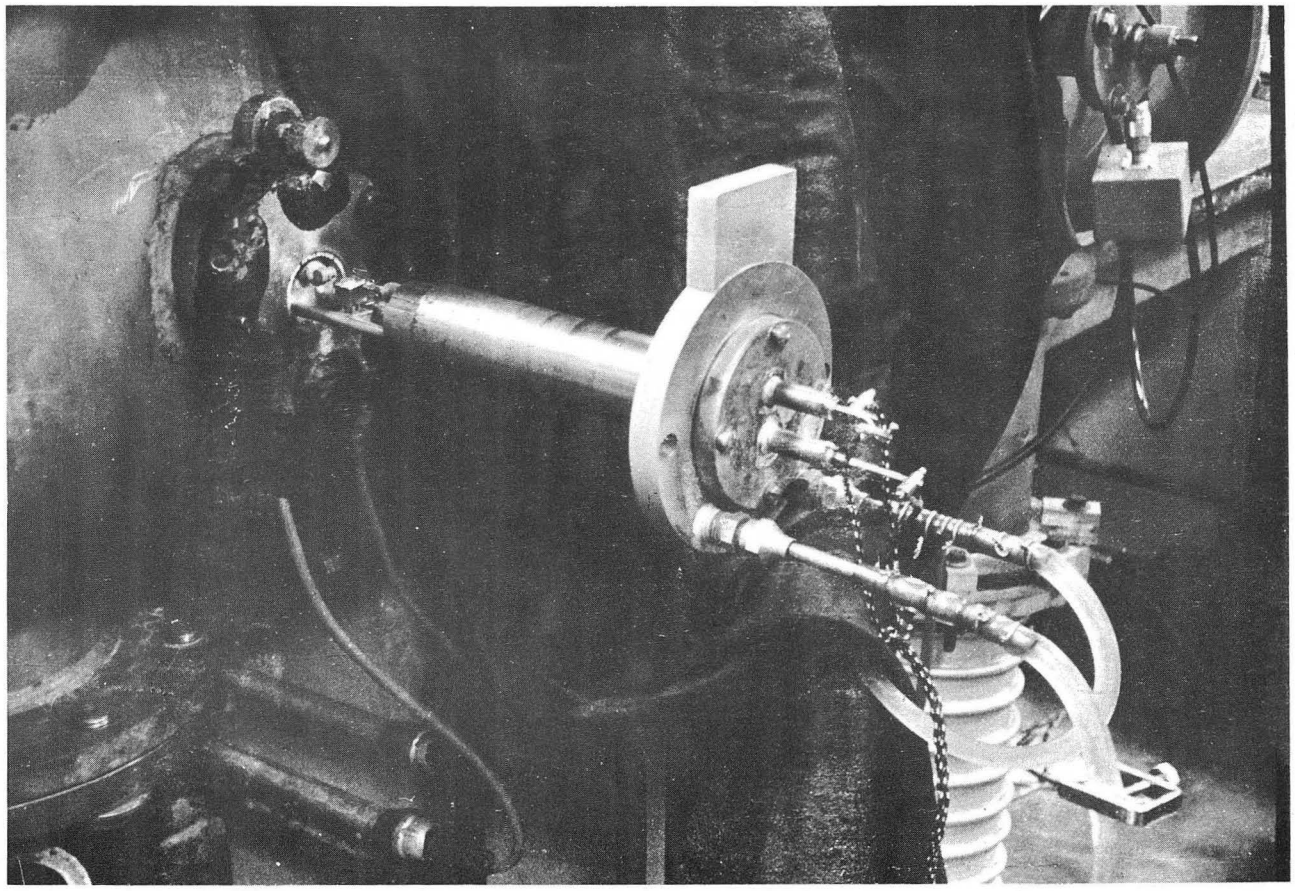

ZN-1731

Fig. 23. Placing the electron bombardment oven loader in the apparatus.

have undergone Majorana transitions (MAJ 32) in the changing field regions between the A and C, and the C and B magnets. This background of about .1% of the full beam is frequently called apparatus background. Depending upon the value of the nuclear spin, radioactive resonances may vary from 2% to 10% of the full beam intensity of the element.

Due to constant drifts in the A and B and also in the C fields, frequent calibrations are necessary. For each radioactive resonance curve presented here, a magnetic field drift curve is also shown. During each of these calibrations only the peak frequency of the Cs^{133} resonance was obtained. The frequency of making calibrations was determined to some extent by the rate of field drift, which changed from run to run. The final field values for a radioactive resonance were determined by various means. In most cases, the final value represents an average of the calibration values taken around the time at which the highest counting rate buttons on a radioactive resonance were taken.

Once the field is calibrated, the frequency appropriate to the measurement to be made is set, and a button is exposed for a fixed interval of time, usually 5 or 10 minutes. At the end of the exposure, the button is removed from the vacuum by means of the button loader (see Figs. 24 and 25). A piece of Scotch tape placed over the face of the sulfur prevents any of the activity from rubbing off and yet does not appreciably attenuate the various emitted radiations. These buttons are then transported to the counting room where their activity is determined, using thin crystal, sodium iodide, scintillation counters, as described in Section III-E. A preliminary counting rate is usually available 5 or 10

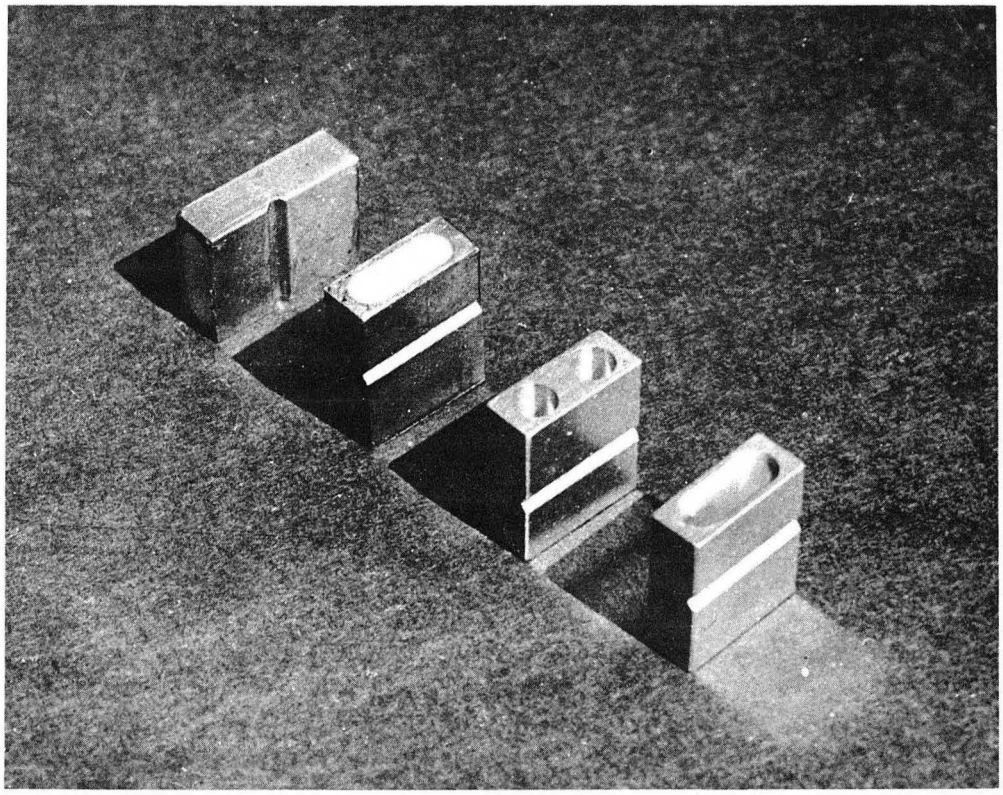

ZN-1732

Fig. 24. The sulfur coated buttons used to collect radioactive cesium atoms.

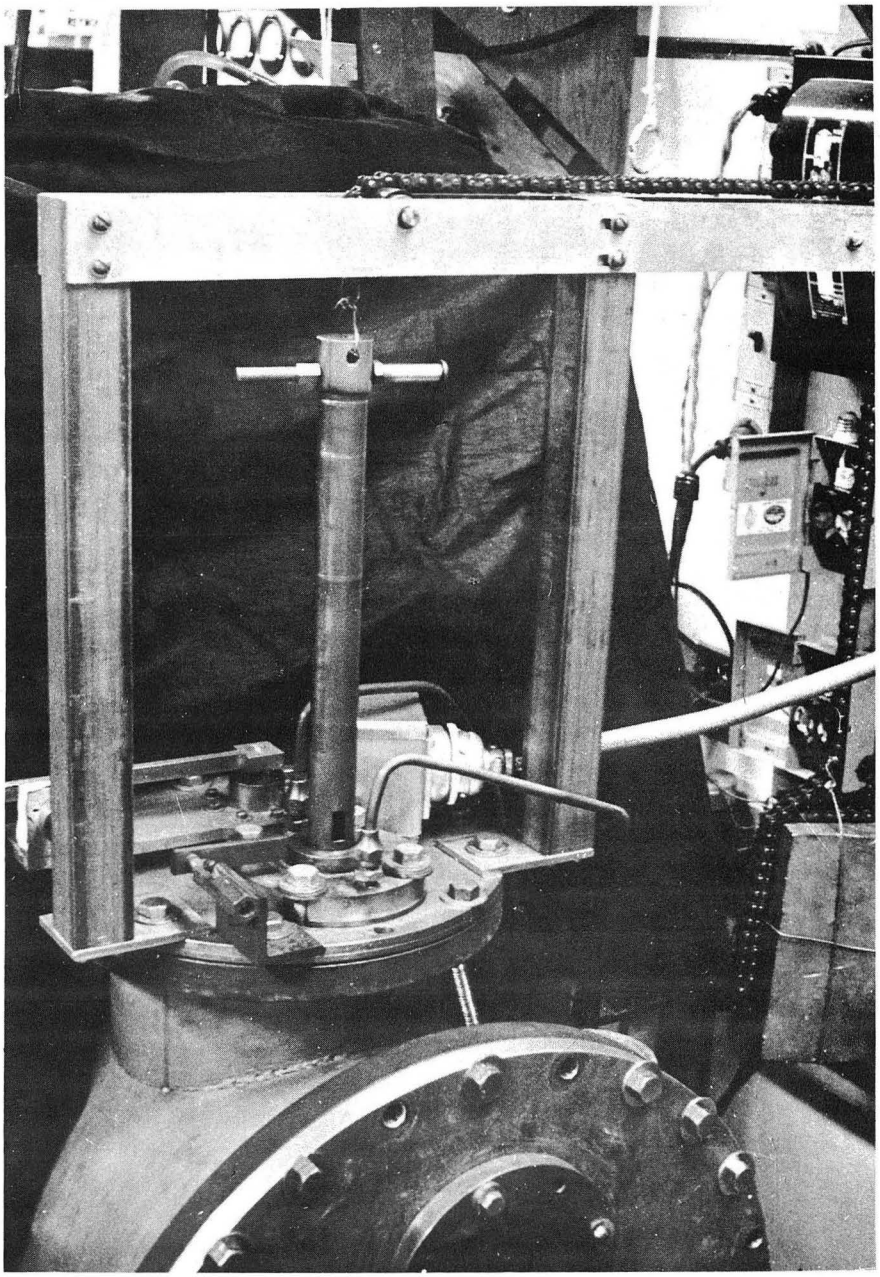

ZN-1733

Fig. 25. The button loader.

minutes after the exposure and may be used in determining future exposure settings. In this way efficient use is made of the relatively limited number of exposures that may be made from a single oven load.

During the initial stages of an investigation of a new isotope, the nuclear spin must be established. The consequent search is lessened by the observed fact that all odd-mass isotopes have half-odd integral spin, while all even-mass isotopes have integral spin. Furthermore, predictions of the shell model and results obtained from beta- and gamma-ray spectroscopy often indicate a preferred or likely value of the nuclear spin. As a guide, this information is useful in planning spin searches. Ultimately, though, many spin values are tried, and most of these serve as background exposures. For the case of a single isotope, the one button which shows a large counting rate is decayed to establish the identity of the isotope. When more than one isotope is present, decays of all high counting rate buttons, as well as of full beam buttons, are compared to indicate isotopic enrichment on certain spin samples. As mentioned in Section II, a single observed resonance does not unambiguously establish the nuclear spin, since the hyperfine structure interaction may shift a resonance position markedly. Sometimes it may be possible to obtain resonance indications at two or more fields during a single run. This is made possible by counting simultaneously with the run.

Just as the spin of a nuclear species may sometimes be predicted, the magnetic moments, and consequently the hyperfine structure separations, for particular nucleon configurations, are amenable to calculation. Oftentimes, an isotope under investigation may have a measured spin equal to the

spin of another isotope of the same element. If the magnetic moment of the second isotope has been measured, it is likely that the moment of the first isotope is quite similar to that of the second. Unfortunately this situation is not helpful for any of the isotopes reported here.

The hyperfine structure separation is obtained by following the resonance of an isotope to progressively higher and higher fields as explained in Section II-D. Due to the limited quantity of material available for these experiments, a search technique which maximizes the information obtained is followed. For a given line width, magnetic field, spin, and resonance peak frequency, the hyperfine structure separation may be determined to within certain limits by Eqs. (22) and (23). It is desirable to reduce the uncertainty on the next run and yet be certain of observing a resonance after exposing a reasonable number of buttons, about 10. Since most searching was done in 100 kc/sec intervals, a region of 1 mc/sec wide may be covered by 10 buttons. If a resonance is observed on at least one of these, the uncertainty in the hyperfine structure separation is greatly reduced. The next 10 exposures may then be used to further decrease the uncertainty at a higher field. Ultimately a limit is reached when a resonance is observed at 200 mc/sec, since this is the highest radiofrequency available with present equipment. The best values of the hyperfine structure separations obtained here for Cs^{127}, Cs^{129}, and Cs^{132} have come from several sweeps of the resonance at about 200 mc/sec.

Most of the calculations necessary to predict operating frequencies were computed the night before the run, although several occasions required computation during a run, so more than one resonance could be observed on

the same day. It should be noted that all of the resonances to be reported here were taken before the facilities of the Radiation Laboratory's IBM 650 data processing computer had been adapted to atomic beam computations. Nevertheless, all of the resonances have since been reprocessed by the computer, using programs developed in this laboratory by Professors Silsbee and Nierenberg. In general the computer results agree closely with results previously computed by hand.

VI. DATA REDUCTION

Information resulting from a run consists of the following:

1. A series of frequencies of the Cs^{133} carrier resonance taken at frequent intervals and used to calibrate the magnetic C field.

2. The heights of the Cs^{133} resonances for use in normalizing successive exposures and compensating for slow drops in beam intensity.

3. The frequency at which each button was exposed.

4. The net counting rate and standard deviation of the counting rate for each button.

5. The time of exposure of each button for exposure normalization.

6. The time of counting each button for decay normalization.

7. The decay information about important buttons for establishing identity of the isotopes responsible for the signal.

A. Treatment of Preliminary Data (Normalizations)

The first corrections applied to all counting rates normalized the various exposures for any variation in the full beam intensity. This was accomplished by dividing the counting rate and the standard deviation by the height of the Cs^{133} resonance during the exposure. During most of the runs, the beam slowly decreased in size, in spite of continual efforts to keep it constant by slowly raising the oven temperature.

Corrections for decay are made when necessary by extrapolating all counting rates to a common time, using the known half-life or apparent half-life in the case of a composite decay. In general, this correction was applied by multiplying the counting rate by a factor, f, given by

$$f = e^{\lambda t}, \qquad (28)$$

where e = the base of the natural logarithms; λ = the disintegration constant = .693/half-life; and t = time at which counting rate was taken minus time to which rates are to be normalized. The half-life correction plays a very important part in the Cs^{130}, Cs^{127}, Cs^{129} computations, but it has little effect on the Cs^{132} counting rates. Once the exposure and decay normalizations have been applied to the net counting rates, a plot of the counting rate versus the frequency of the exposure will give an indication of the resonance. Such plots appear later in Figs. 35 to 60. It must be kept in mind that no account for the variation in C field with time is made in these plots, except when a plot represents a superposition of two sweeps, first up in frequency and then down in frequency. On the other hand, the magnetic field calibration is calculated for those points nearest the center of the resonance, since those points have the most weight in determining the resonance peak position.

B. Curve Fitting

Before high-speed computer facilities were available, the peak resonance frequency was estimated by eye, with the results that appear later in Table 8. Recently, however, Professor Silsbee has programmed for the IBM 650 computer a fixed decimal point routine which fits a bell-shaped curve to the normalized data points. More exactly, the reciprocals of the counting rates are fitted to a parabola by a weighted least squares procedure. This technique gives more weight to points near the resonance peak. In this way, departures from a symmetric line shape have little effect on the

peak frequency determination.

If $y_i \pm \sigma_i$ is the counting rate and standard deviation at a frequency, x_i, the routine fits the polynomial $a + bx + cx^2$ to the set of quantities $1/y_i$ by minimizing the weighted square of the deviations from the curve.

$$\sum_i \left[\frac{(1/y_i) - (a + bx + cx^2)}{(\sigma_i/y_i^2)} \right]^2 = \text{minimum.} \qquad (29)$$

The weighting factor, $(\sigma_i/y_i^2)^2$ results from the relation

$$d(1/y_i) = dy_i/y_i^2 = \sigma_i/y_i^2. \qquad (30)$$

The mechanical solution of the problem involves solving four three-by-three determinants, the factors of which involve quantities of the type: $\sum_i y_i^3/\sigma_i^2$; $\sum_i x_i y_i^3/\sigma_i^2$; $\sum_i x_i^2 y_i^3/\sigma_i^2$; $\sum_i y_i^4/\sigma_i^2$; $\sum_i x_i y_i^4/\sigma_i^2$; $\sum_i x_i^2 y_i^4/\sigma_i^2$; $\sum_i x_i^3 y_i^4/\sigma_i^2$; and $\sum_i x_i^4 y_i^4/\sigma_i^2$. From these determinants, the position of the peak, the height of the peak, the half-width of the curve at half maximum, and the uncertainty in the peak location due to the uncertainties in the input data are calculated. The routine accepts up to 20 experimental points per resonance and completes the calculation in 15 to 20 seconds. The corresponding time required to complete the same calculation by hand lies between 20 and 90 minutes, depending upon the number of data points.

C. Magnetic Field Calculations

For an isotope with known hyperfine structure separation, $\Delta\nu$, magnetic moment, μ_I, nuclear spin, I, and electronic g-factor, g_J, the magnetic field, H, is given by Eq. (22) as a function of frequency, ν. Solution for

H involves solving a quadratic equation in ν by the quadratic formula or by iterative techniques. The value of the constants for Cs^{133} which were used in all calculations appear in Table 2. They are taken from various tables listed in RAM 56. The fundamental constants are those of DuMond and Cohen (DUM 53).

Table 2. Constants for Cs^{133}, I = 7/2

$\Delta\nu = 9192.63183(1)$ mc/sec

$\mu_I = +\ 2.57887(30)$ n.m.

$g_J = 2.00250(6)$

$\mu_o = .92732(6) \times 10^{-20}$ erg/gauss

$h = 6.6252(5) \times 10^{-27}$ erg sec

$\mu_B/\mu_{n.m.} = 1836.13(4)$

Computer routines, using both the Wolontis interpretive floating decimal point system, as well as one using fixed point operation, are available. The interpretive routine, developed by Professor Nierenberg, essentially evaluates the quadratic formula using the square root subroutine of the interpretive language of the Wolontis system. The quadratic formula is used in the form

$$x = \frac{-2c}{+b \pm (b^2 - 4ac)^{1/2}} \tag{31}$$

in order to avoid loss in significant figures. Professor Silsbee's fixed point routine performs an iteration, using a rapidly converging form derived from Eq. (22):

$$H = \frac{h}{\mu_o(g_I - g_J)}\,\beta\,\frac{1 + \frac{\beta}{\Delta\nu}}{\frac{1}{2I+1} + \frac{\beta}{\Delta\nu}}, \tag{32}$$

where $\beta = \nu + \frac{g_I \mu_o}{h} H$. This form converges to within a milligauss after three or four iterations for fields in the region up to 300 gauss.

D. Hyperfine Structure Separation Calculations

The hyperfine structure separation, $\Delta\nu$, and the nuclear g-factor, g_I, are in principle obtained from Eq. (22) by solving that equation at two values of ν and H. In practice, however, ν and H are not determined with sufficient accuracy to permit such an evaluation. Consequently, g_I is obtained from $\Delta\nu$ by the Fermi-Segrè relation [Eq. (23)] and substituted in Eq. (22), first assuming a positive sign for g_I and hence a positive sign for the nuclear magnetic moment. This reduces Eq. (22) to one unknown, $\Delta\nu$. Thus a $\Delta\nu$ may be calculated for a given spin, I, magnetic field, H, frequency, ν, and a positive nuclear moment. Because of the ambiguity of sign in Eq. (23), the above procedure is repeated, assuming a negative nuclear magnetic moment, to obtain a second value of $\Delta\nu$.

These calculations also are programmed for the IBM 650 computer in a manner similar to the magnetic field calculations described in the previous section. The results of these computations appear later in Table 9.

E. Magnetic Moment Calculation

With a given hyperfine structure separation, $\Delta\nu$, the Fermi-Segrè relation of Eq. (23) predicts the nuclear magnetic moment within the uncertainties of the derivation of the equation itself. When the known constants of Cs^{133} are used, the relation becomes:

$$\mu_I = 6.4123 \times 10^{-4} \frac{I}{2I + 1} \Delta\nu, \qquad (33)$$

for other cesium isotopes. Magnetic moments calculated from Eq. (33) are subject to a diamagnetic shielding correction which amounts to an increase in the observed moment by 1/2 percent for a Z of 55 (RAM 56). Also important, however, are the inherent errors in the derivation of the relation. The Fermi-Segrè relation assumes that nuclear magnetism is uniformly distributed over the nuclear volume. Deviations from this assumption give rise to the hyperfine structure anomaly which was first treated theoretically by Bohr and Weisskopf (BOH 50).

F. Treatment of Errors

The errors in the hyperfine structure determination enter from several sources. The magnetic field is determined from a frequency which could be set with limited accuracy. In addition, the magnetic field drifts with time to introduce uncertainties. In most cases the error placed on ν_o represents a root mean square deviation of the points used to compute ν_o. The effect of the error in ν_o, $\delta\nu_o$, on the calculation of $\Delta\nu$ was computed by obtaining the quantity $\partial\Delta\nu/\partial\nu_o$, under the assumption that $g_I = 0$. In this way the quantity $\partial\Delta\nu/\partial\nu_o$ could be used approximately for both $\Delta\nu_+$ and $\Delta\nu_-$ (i.e., assumed positive and negative moment).

The radioactive resonances usually contained data points in frequency steps of 100 kc/sec. The $\Delta\nu$'s calculated from the peak of the computer-fitted, bell-shaped curves indicate a consistency compatible with a probable error of about 1/20 the line width at 1/2 maximum. These errors are used in plotting the graphs of Figs. 30, 31, and 32. The more conservative error of 1/8 the frequency width at 1/2 maximum is used in computing

final errors.

The uncertainty in the frequency of the peak, due to a dependence on the uncertainties in the input data, is combined with the half-width uncertainty above before computing a resulting error in $\Delta\nu$. Thus the stated error on the radioactive peak frequency is the square root of the sum of the squares of the half-width uncertainty and the uncertainty arising from uncertainties in the input data. Here also the effect on $\Delta\nu$ is obtained by calculating $\partial\Delta\nu/\partial\nu$ and multiplying by the uncertainty in ν.

The final error on each $\Delta\nu$ is obtained from the square root of the sum of the squares of the $\Delta\nu$ uncertainties arising from errors in ν and ν_o.

The best value of $\Delta\nu$ for an isotope is taken as the weighted average of all hyperfine structure separation measurements. The weighting factor of the square of the reciprocal of the stated uncertainties, given in Table 9, assures that the highest weight is given to measurements with smallest error. The stated error of the final average (Table 10) is approximately the error of the highest field measurement.

A minimum error of 1% is placed on any magnetic moment obtained from the Fermi-Segrè formula to allow for the effects of diamagnetic shielding and the hyperfine structure anomaly.

G. Example of a $\Delta\nu$ Calculation

Run 0352

Calibration frequency $\nu_o = 81.399 \pm .005$ mc/sec

Frequency from curve fit $\nu = 129.989$ mc/sec

$\partial\Delta\nu/\partial\nu_o = 1.890 \frac{\text{mc/sec}}{\text{kc/sec}}$

$\partial\Delta\nu/\partial\nu = 1.184 \frac{\text{mc/sec}}{\text{kc/sec}}$

(Moment assumed positive) $\Delta\nu_+ = 8650.9$ mc/sec

(Moment assumed negative) $\Delta\nu_- = 8999.4$ mc/sec

(Uncertainty due to input data)^2 $\sigma^2 = .0000207$ mc^2/sec^2

(Half-width at half maximum)^2 $\omega^2 = .0338$ mc^2/sec^2

(Conservative error due to ω)^2 $\omega^2/16 = .00211$ mc^2/sec^2

(Probable error due to ω)^2 $\omega^2/100 = .000338$ mc^2/sec^2

Probable error in $\nu = \pm .019$ mc/sec

Conservative error in $\nu = \pm .046$ mc/sec

Error in $\Delta\nu$ due to error in H $= \pm 9.5$ mc/sec

Probable error in $\Delta\nu$ due to error in $\nu = \pm 22.5$ mc/sec

Conservative error in $\Delta\nu$ due to error in $\nu = \pm 54.5$ mc/sec

Probable uncertainty in $\Delta\nu = \pm 24.5$ mc/sec

Conservative uncertainty in $\Delta\nu = \pm 55.3$ mc/sec

$\Delta\nu_+ = 8650.9$ mc/sec $\pm$ 55.3 conservative

$\Delta\nu_- = 8999.4$ mc/sec $\pm$ 24.5 probable.

H. Decay Curves

For the purposes of identification, the decay of important samples was followed. When only one component was present, the half-life was determined by the best eye-fit of a straight line to the experimental points (see Figs. 26, 27, 28, and 29).

Composite decay of two components, such as in the decay of each resonance button in Runs 0231 and 0232, were fitted by a least squares technique. In particular, a series of decay points $y_i(t) \pm \sigma_i$ were fitted to $Ae^{-\lambda_1 t} + Be^{-\lambda_2 t}$ by minimizing the quantity

$$\sum_i \left[\frac{y_i(t) - Ae^{-\lambda_1 t} - Be^{-\lambda_2 t}}{\sigma_i} \right]^2 ,$$

where λ_1 is the disintegration constant of the A component; λ_2 is the disintegration constant of the B component; A is the amplitude of the A component; B is the amplitude of the B component. The amplitude A, for example, is given by

$$A = \frac{\begin{vmatrix} \sum_i e^{-\lambda_1 t} y_i/\sigma_i^2 & \sum_i e^{-\lambda_1 t} e^{-\lambda_2 t}/\sigma_i^2 \\ \sum_i e^{-\lambda_2 t} y_i/\sigma_i^2 & \sum_i (e^{-\lambda_2 t})^2/\sigma_i^2 \end{vmatrix}}{\begin{vmatrix} \sum_i (e^{-\lambda_1 t})^2/\sigma_i^2 & \sum_i e^{-\lambda_1 t} e^{-\lambda_2 t}/\sigma_i^2 \\ \sum_i e^{-\lambda_1 t} e^{-\lambda_2 t}/\sigma_i^2 & \sum_i (e^{-\lambda_2 t})^2/\sigma_i^2 \end{vmatrix}} . \qquad (34)$$

B is given by the same form with the roles of λ_1 and λ_2 interchanged. If the denominator of Eq. (34) is called Δ, the standard deviation of A

is given by

$$\sigma^2(A) = \frac{1}{\Delta} \Sigma \, (e^{-\lambda_2 t})^2 / \sigma_i^2, \tag{35}$$

where λ_2 is the disintegration constant of the B component.

VII. EXPERIMENTAL RESULTS

A. Run Classification

For the purpose of identification, each computation is given a code number consisting of four digits. The middle two digits are the run number and usually correspond to a single cyclotron bombardment. The last digit refers to a particular resonance sweep taken during the run. The first digit is used to distinguish different computations on the same sweep. For example if a resonance is counted twice, then the first counting may appear as 0--- and the second counting as 1---. A list of the runs discussed here appears in Table 3, and a description of the code used for the various $\Delta\nu$ curves appears in Table 4.

Table 3. Summary of Atomic Beam Runs

Run	Remarks
7	Observed I = 1/2 for Cs^{127} and Cs^{129}.
14	Confirmed I = 1/2 for Cs^{127} and Cs^{129}; preliminary $\Delta\nu$.
15	Obtained $\Delta\nu$ of Cs^{127} and Cs^{129}.
16	Enhanced Cs^{127} production over Cs^{129}; preliminary $\Delta\nu$.
17	Observed I = 1 for Cs^{130}.
19	Confirmed I = 1 for Cs^{130}.
20	Obtained $\Delta\nu$ of Cs^{130}.
23	Obtained $\Delta\nu$ of Cs^{127} and Cs^{129}.
25	Obtained $\Delta\nu$ of Cs^{130}.
26	Obtained $\Delta\nu$ of Cs^{130}.
28	Observed I = 1/2 for Cs^{129}, I = 5/2 for Cs^{131}, and I = 2 for Cs^{132} from xenon bombardment; preliminary $\Delta\nu$ of Cs^{132}.
35	Obtained $\Delta\nu$ of Cs^{132}.

Table 4. Summary of Δν Curves

Run Code	Frequency Steps	Isotopes	Remarks
0151	250 kc/sec	Cs^{127}, Cs^{129}	First counting
1151	250	Cs^{127}, Cs^{129}	Second counting
0152	100	Cs^{127}, Cs^{129}	First counting
1152	100	Cs^{127}, Cs^{129}	Second counting
0160	250	Cs^{127}, Cs^{129}	
0200	200	Cs^{130}	Counter variation neglected
1200	200	Cs^{130}	Counter variation corrected
0231	150	Cs^{127}	
1231	150	Cs^{129}	
0232	50	Cs^{127}	
1232	50	Cs^{129}	
0250	100	Cs^{130}	
0260	100	Cs^{130}	
0280	100	Cs^{132}	
0351	100	Cs^{132}	
0352	100	Cs^{132}	
0353	100	Cs^{132}	Third ~~First~~ counting
1353	100	Cs^{132}	Second counting

Table 5. Counting Rates for Cs^{127} and Cs^{129} Half-Integral Spin Values

Spin Value	1/2	3/2	5/2	7/2	9/2
Counting Rate (Arbitrary Units)	100±1.3	1.4±0.2	1.9±0.2	1.8±0.2	1.4±0.2

B. Run Information

Run 7

Purpose: To obtain the spin of Cs^{127} and Cs^{129}.

Target: 50 mils deep BaI_2 covered by two 1-mil Al foils.

Bombardment: 47.5 μa-hr of α's at 45.5 Mev in 6 hours.

Carrier: 16 mg CsI and .9 mg RbI.

Beam duration: 3 hr, 50 min.

Results: All spin values from 1/2 to 9/2 were exposed with the results shown in Table 5. The signal at spin 1/2 clearly established a resonance and decayed, as is shown in Fig. 26. Both Cs^{127} and Cs^{129} appear on the spin 1/2 sample in the same proportions as they do on the full beam sample. The activity ratio Cs^{127}/Cs^{129} was .25 at the end of the bombardment.

Run 14

Purpose: To verify the spin of Cs^{127} and Cs^{129}.

Target: 13.2 μa-hrs of α's at 45.5 Mev in 35 min.

Carrier: 16.3 mg CsI.

Beam duration: 4 hrs, 30 min.

Results: The resonance of Cs^{127} and Cs^{129} was observed again at I = 1/2 for a different magnetic field than in Run 7. A very poor resonance of I = 1/2 at 80 mc/sec showed that the $\Delta\nu$ was in the region of 8000 to 10,000 mc/sec.

Run 15

Purpose: To obtain the $\Delta\nu$ of Cs^{127} and Cs^{129}.

Target: 50 mils of BaI_2 covered by two 1-mil dural foils.

Bombardment: 68.6 μa-hrs of 45.5 Mev α's in 3 hr.

Carrier: 25 mg of CsI.

Results: Two sweeps of the I = 1/2 resonance at ~127 mc/sec provided the first useful estimates of the hyperfine structure separation of Cs^{127} and Cs^{129}. The two sweeps are labeled 0151 and 0152. Later, the buttons were counted again and the resulting peaks called 1151 and 1152 (see Figs. 34, 35, 36, 37, and 38).

Run 16

To enhance the production of Cs^{127}, a thin layer of powder permits the α-particles to leave the powder before the cross section of the Cs^{129} reaction becomes large. This scheme does not produce more Cs^{127}, but it does increase the ratio of Cs^{127}/Cs^{129}.

Purpose: To enrich the production of Cs^{127} over Cs^{129} and verify their spins.

Target: 18 mils BaI_2 and two 1-mil dural foils.

Bombardment: 108 μa-hrs of 45.5 Mev α's in 4 hrs.

Carrier: 25 mg CsI.

Beam Duration: 4 hrs.

Results: The I = 1/2 resonance was seen again and decayed, as shown in Fig. 27. Again, the spin 1/2 sample decayed exactly as the full beam sample. The Cs^{127}/Cs^{129} activity ratio was found to be 1.50 at the end of the bombardment. This ratio is six times higher than it was in Run 7. A $\Delta\nu$ resonance is shown in Fig. 40.

Run 17

Thick absorber foils were used to reduce the α-particle energy to limit the production of Cs^{127} and Cs^{129} and still permit the α,n reaction which makes Cs^{130}.

Purpose: To obtain the spin of Cs^{130}.

Target: 30 mils BaI_2 covered by 22 mils of Al foils.

Bombardment: 17.5 μa-hrs of 45.5 Mev α's in 30 min.

Carrier: 4.7 mg of CsI.

Beam Duration: 1 hr.

Results: The counting rates of all integral spins from 0 to 4, as shown in Table 6, indicate the nuclear spin of Cs^{130} is I = 1. The spin I = 1 samples decayed with essentially a 30 minute half-life, corresponding to Cs^{130}, while the full beam contained an appreciable quantity of Cs^{129} (31 hr half-life).

Table 6. Counting Rates for Cs^{130} Integral Spin Values

Spin Value	0	1	2	3	4
Counting Rate (Arbitrary Units)	-14±7	100±13	7±5	14±6	9±3

Run 19

Purpose: To verify the spin of Cs^{130}.

Target: 30 mils of BaI_2 covered by 22 mils of Al foil.

Bombardment: 5.6 μa-hr of 45.5 Mev α's in 15 min.

Carrier: 5.0 mg CsI.

Beam Duration: 1 hr.

Results: The assignment of I ± 1 to Cs^{130} was verified, and the decay curve shown in Fig. 28 was obtained. The enrichment of the 30 minute component in the spin sample over the full beam is very large.

Run 20

Purpose: To obtain the $\Delta\nu$ of Cs^{130}.

Target: 30 mils BaI_2 covered by 23 mils of Al foils.

Bombardment: 16.0 μa-hr of 45.5 Mev α's in 35 min.

Carrier: 8.6 mg CsI.

Beam Duration: 1 hr.

Results: One sweep of the I = 1 resonance at 49 mc (Figs. 42 and 43) gave a preliminary value of the hyperfine structure separation of Cs^{130}. Computation 0200 assumes all of the counters have the same counting efficiency, which is not exactly true. Computation 1200 uses data points which have been corrected for variations in counter efficiency.

Run 23

Purpose: To obtain better $\Delta\nu$'s for Cs^{127} and Cs^{129}.

Target: 16 mils BaI_2 covered by two 1-mil dural foils.

Bombardment: 126 μa-hr of 45.5 Mev α's in 4.4 hr.

Carrier: Not recorded.

Beam Duration: 8 hr.

Results: Two resonance curves of Cs^{127} and Cs^{129} at 200 mc/sec were obtained. Fig. 45 shows the resolution of the resonance, taken in 150 kc/sec steps, into its two components. Fig. 47 shows a similar analysis of the curve taken in 50 kc/sec steps.

Run 25

Purpose: To improve the $\Delta\nu$ measurement of Cs^{130}.

Target: 25 mils BaI_2 covered by 22 mils of Al foil.

Bombardment: 19.1 μa-hr of 45.5 Mev α's in 30 min.

Carrier: 9.2 mg CsI.

Beam Duration: 1 hr.

Results: A resonance, shown in Fig. 49, gave an improved value to the hyperfine structure separation of Cs^{130}.

Run 26

Purpose: To improve the $\Delta\nu$ measurement of Cs^{130}.

Target: 16 mils BaI_2 covered by 19 mils Al foil.

Bombardment: 16 μa-hr of 45.5 Mev α's in 40 min.

Carrier: 82 mg CsI.

Beam Duration: 1 hr.

Results: Curve 0260 (Fig. 51) shows the Cs^{130}, 90 mc/sec resonance which establishes the hyperfine structure separation to about 6%.

Run 28

Purpose: To obtain the spin of Cs^{132}.

Target: 2 liters of xenon gas at atmospheric pressure.

Bombardment: 67 μa-hr of 12 Mev protons in 3.5 hr.

Carrier: 35 mg CsI.

Beam Duration: 7 hr, 30 min.

Results: The spins of I = 1/2 for Cs^{129}, I = 5/2 for Cs^{131} and I = 2 for Cs^{132} were all observed (see Table 7). The important

Table 7. Counting Rates for Cs^{132} Spin Search

Spin	Counting rate (arbitrary units)	Isotope identity
0	4.8 ± .4	
1/2	127.8 ± 1.8	Cs^{129}
1	6.1 ± .4	
3/2	35.7 ± 1.0 *	Cs^{129} *
2	54.5 ± 1.2	Cs^{132}
5/2	27.7 ± .9	Cs^{131}
3	4.8 ± .4	
7/2	5.0 ± .4	
4	6.5 ± .4	
9/2	4.5 ± .4	
5	7.5 ± .4	
6	3.8 ± .3	
7	2.7 ± .3	

* The second harmonic of the 3/2 frequency caused a resonance of I = 1/2 to appear on the I = 3/2 sample.

samples decayed as shown in Fig. 29. All of the samples are easily identified by their respective half-lives. The measurement of I = 5/2 for Cs^{131} confirms the earlier work of Bellamy and Smith (BEL 53). A sweep of the I = 2 resonance (Fig. 53) at 34 mc gave a preliminary value of the hyperfine structure separation of Cs^{132}.

Run 35

Purpose: To confirm the spin assignment of Cs^{132} and to increase the accuracy of the Cs^{132} $\Delta\nu$.

Target: 2 liters of gaseous xenon at one atmosphere pressure.

Bombardment: 127 μa-hr of 12 Mev protons in 4.6 hr.

Carrier: 37.4 mg CsI.

Beam Duration: 9 hr.

Results: Three sweeps (0351, 0352, and 0353) of the Cs^{132} resonance were obtained at 70, 130 and 200 mc/sec respectively (see Figs. 55, 57, 59, 60).

C. Determination of the Nuclear Magnetic Moment Sign

An estimate of the consistency of the hyperfine structure separation obtained for a given sign of the nuclear magnetic moment is made by plotting $\Delta\nu$ versus the magnetic field at which the observation was made. For this purpose the errors, as discussed in Section VI-F, due to 1/20 the line width, are used. Figs. 30, 31, and 32 show such plots. For Cs^{127} and Cs^{129}, the assumption of a positive magnetic moment (Fig. 30) is more consistent with the experimental data than would be a negative moment. The

choice of a positive sign for Cs^{127} and Cs^{129} rests on this observation. The positive sign choice is consistent with the simple Schmidt picture of magnetic moments which requires the magnetic moment of odd Z, spin 1/2 nuclei to lie between - .26 and + 2.79 nuclear magnetons. (MAY 55)

The scatter in experimental data for Cs^{130} (Fig. 31) makes a sign determination impossible. As a result, values of the hyperfine structure separation and the nuclear magnetic moment are given for either sign assumptions.

On the basis of data presented in Fig. 32, the nuclear magnetic moment of Cs^{132} is positive. The theoretical curve drawn for the assumed negative moment shows the calculated variation of the observed hyperfine structure separation. The "correct" values of the hyperfine structure separation and magnetic moment are used in this computation.

D. Summary of Measurements

As a result of 12 cyclotron bombardments, totalling 28.5 hours, four nuclear spins and four hyperfine structure separations have been established.

Table 8. Comparison of Eye-Fit and Computer-Fit to Resonances

Run	Eye-Fit (Conservative Errors)	Computer-Fit
0151	127.500(200) mc/sec	127.283(289) mc/sec
0152	127.400(150)	127.269(165)
1151	127.500(200)	127.636(420)
1152	127.400(150)	127.216(160)
0160	127.500(500)	127.262(283)
0231	200.050(100)	200.020(89)
0232	200.200(100)	200.119(67)
1231	199.900(100)	199.868(84)
1232	200.000(100)	200.016(77)
0200	48.300(150)	48.293(141)
0250	91.250(200)	91.124(150)
0260	91.200(100)	91.096(103)
0280	34.000(75)	---
0351	70.325(75)	70.318(59)
0352	130.000(50)	129.989(46)
0353	200.975(50)	200.981(35)
1353	200.975(50)	200.988(72)

Table 9. Summary of Hyperfine Structure Separation Calculations. The errors in the last significant figures are given in parentheses.

Run	Isotope	ν_o	ν	$\Delta\nu+$	$\Delta\nu-$	Error
0151	$Cs^{127, 129}$	32.195(5)	127.283(289)	10,430	12,440	±2300
0152	$Cs^{127, 129}$	32.171(3)	127.269(165)	9,940	11,630	1180
1151	$Cs^{127, 129}$	32,195(5)	127.636(420)	8,560	9,560	2200
1152	$Cs^{127, 129}$	32.171(3)	127.216(160)	10,260	12,160	1070
0160	$Cs^{127, 129}$	32.225(15)	127.262(283)	11,390	14,190	2820
0231	Cs^{127}	50.787(5)	200.020(89)	8,939	9,621	204
0232	Cs^{127}	50.811(5)	200.119(67)	8,928	9,606	155
1231	Cs^{129}	50.787(5)	199.868(84)	9,255	10,02o	210
1232	Cs^{129}	50.811(5)	200.016(77)	9,139	9,872	185
0200	Cs^{130}	18.026(5)	48.293(141)	5,425	5,850	965
0250	Cs^{130}	34.106(10)	91.124(150)	6,607	6,998	433
0260	Cs^{130}	34.070(18)	91.096(103)	6,432	6,790	310
0280	Cs^{132}	21.296(5)	34.000(75)	9,721	12,436	1850
0351	Cs^{132}	43.964(7)	70.318(59)	8,518	9,184	240
0352	Cs^{132}	81.399(5)	129.989(46)	8,651	8,999	55
0353	Cs^{132}	126.039(7)	200.981(35)	8,653	8,868	18
1353	Cs^{132}	126.039(7)	200.988(72)	8,650	8,864	36

The final values obtained appear in Table 10.

Table 10. Nuclear Spins, Hyperfine Structure Separations, and Magnetic Moments

Isotope	Spin	$\Delta\nu$ mc/sec	Magnetic Moment, n.m.
6.2 h Cs^{127}	I = 1/2	$\Delta\nu$ = 8960±200	μ_I = +1.44±.03
31 h Cs^{129}	I = 1/2	$\Delta\nu$ = 9230±200	μ_I = +1.48±.03
30 m Cs^{130}	I = 1	$\Delta\nu$ = 6420±350 if	μ_I = +1.37±.08
		$\Delta\nu$ = 6800±350 if	μ_I = -1.45±.08
6.2d Cs^{132}	I = 2	$\Delta\nu$ = 8653±30	μ_I = +2.22±.02

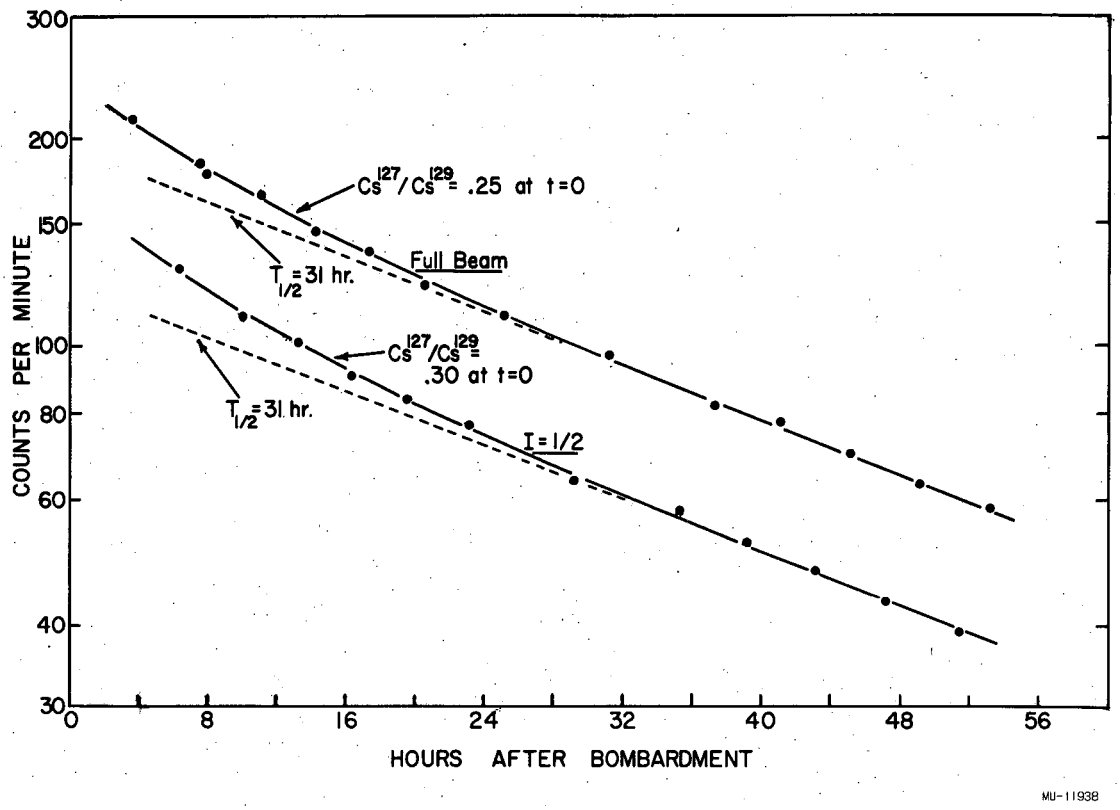

Fig. 26. Decay of I = 1/2, Cs^{127} and Cs^{129} button.

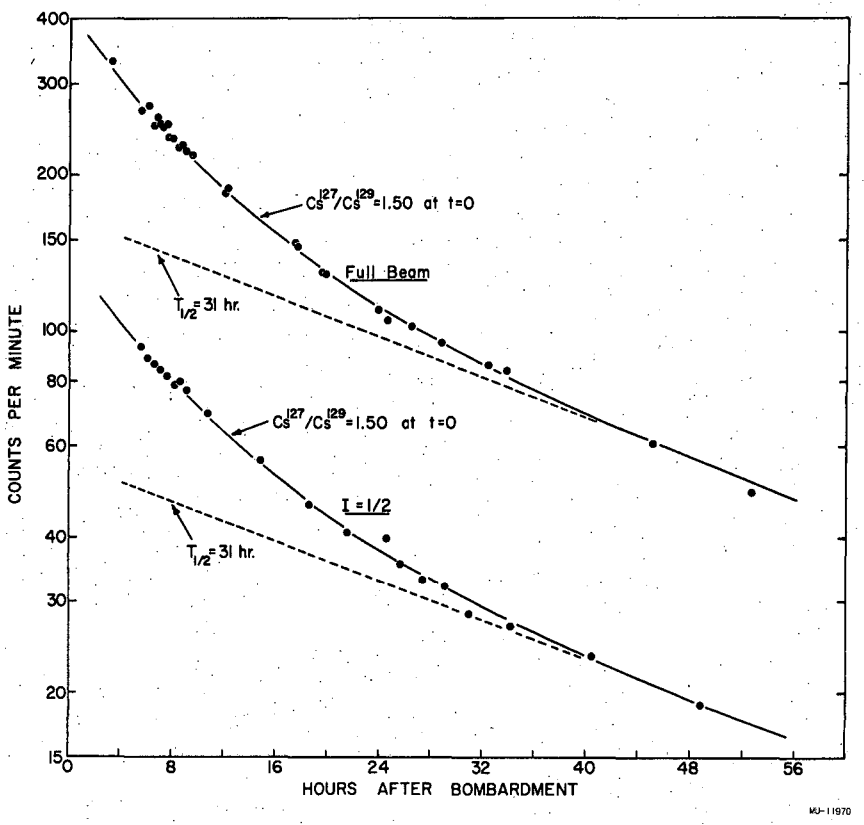

Fig. 27. Decay of I = 1/2, Cs^{127} and Cs^{129} button.

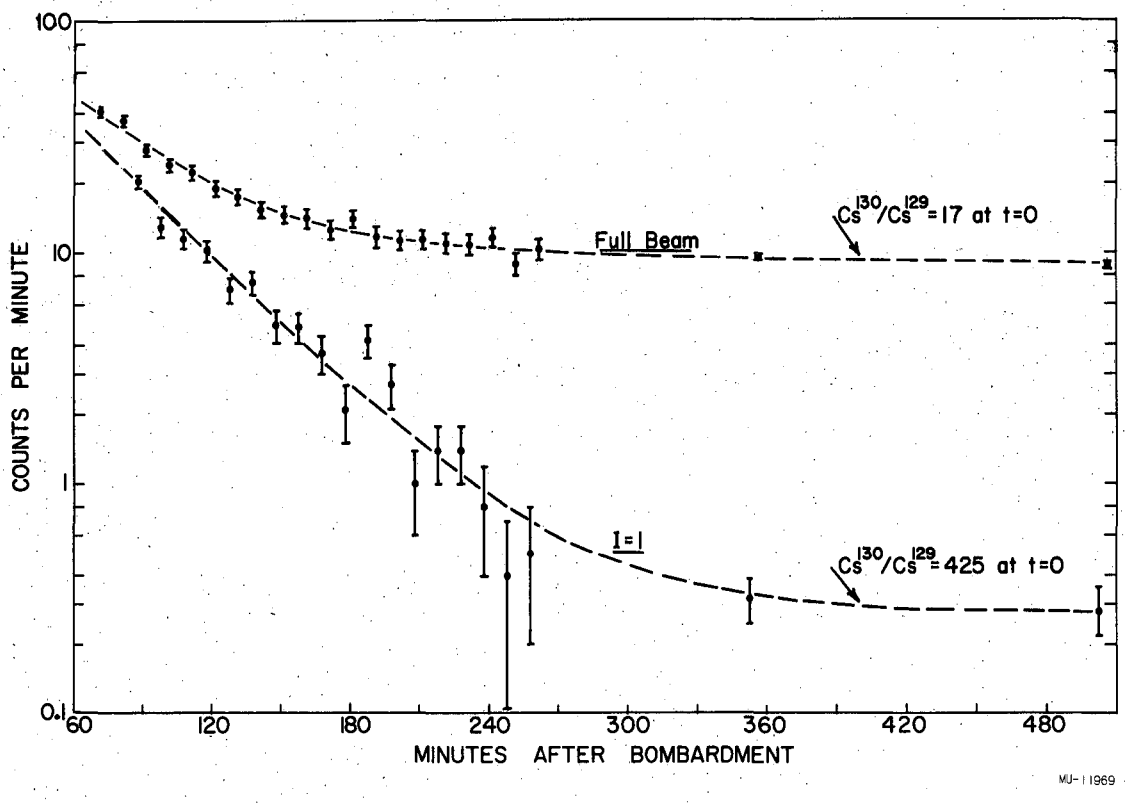

Fig. 28. Decay of I = 1, Cs^{130} button.

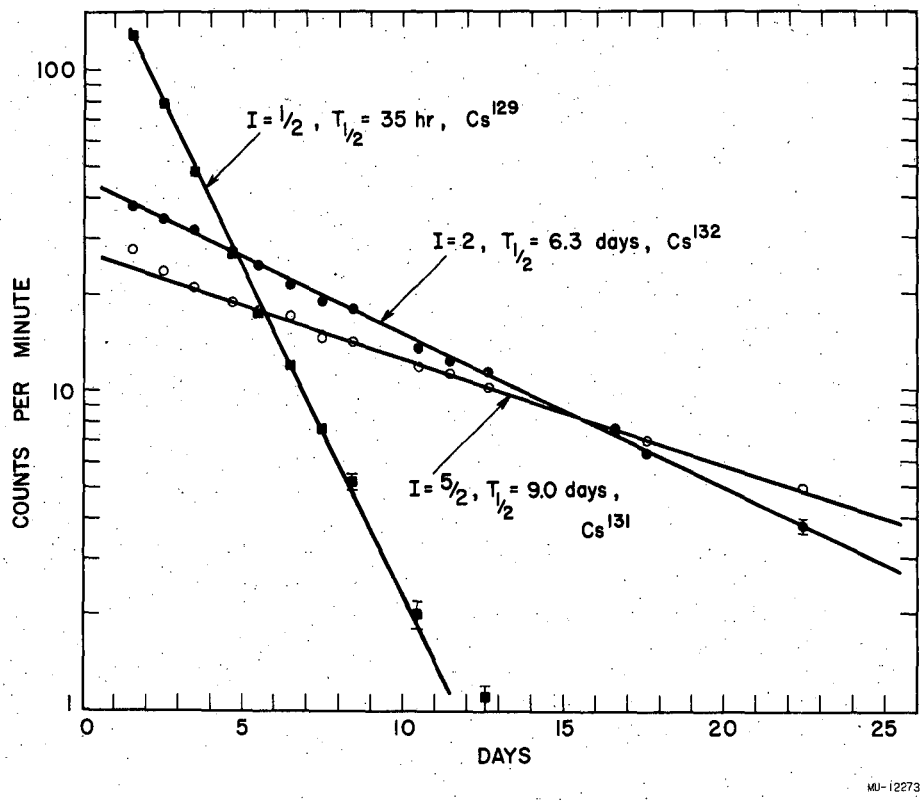

Fig. 29. Decay of I = 2, Cs^{132} button.

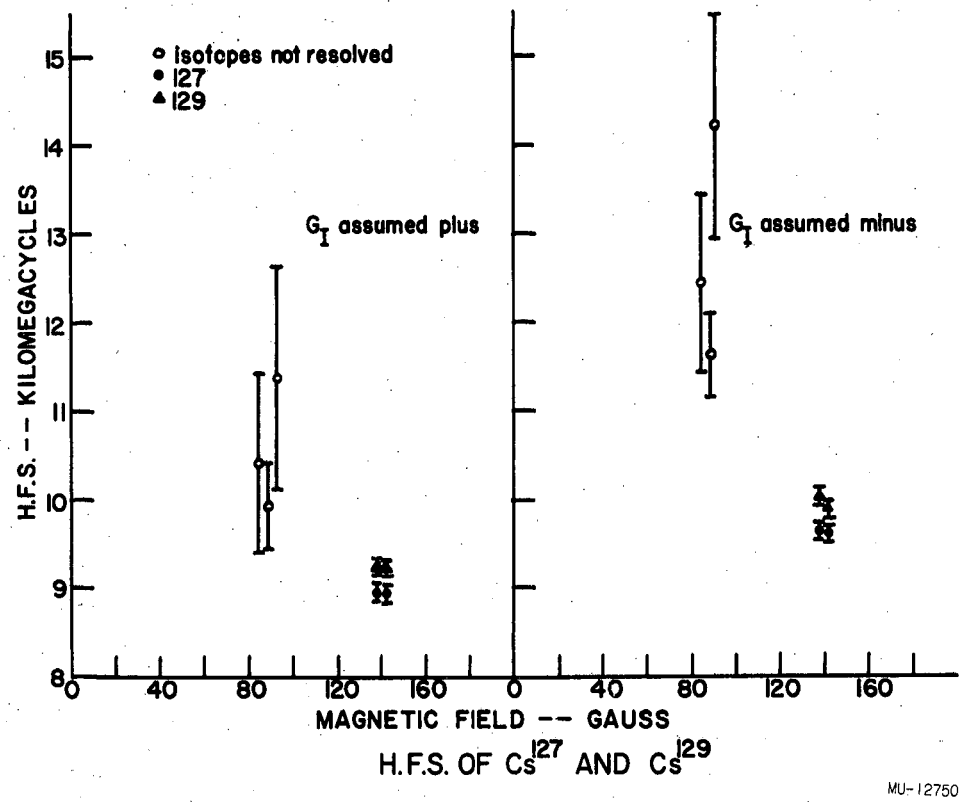

Fig. 30. $\Delta\nu$ sign determination for Cs^{127} and Cs^{129}.

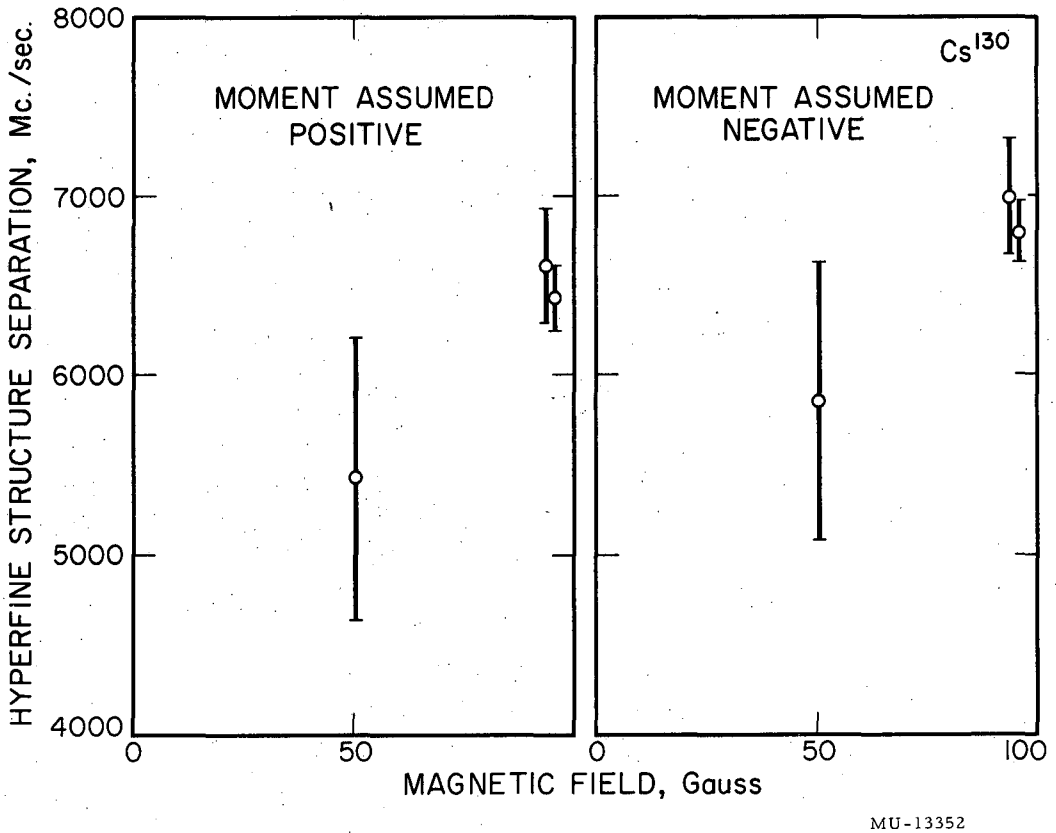

Fig. 31. $\Delta\nu$ sign curves for Cs^{130}.

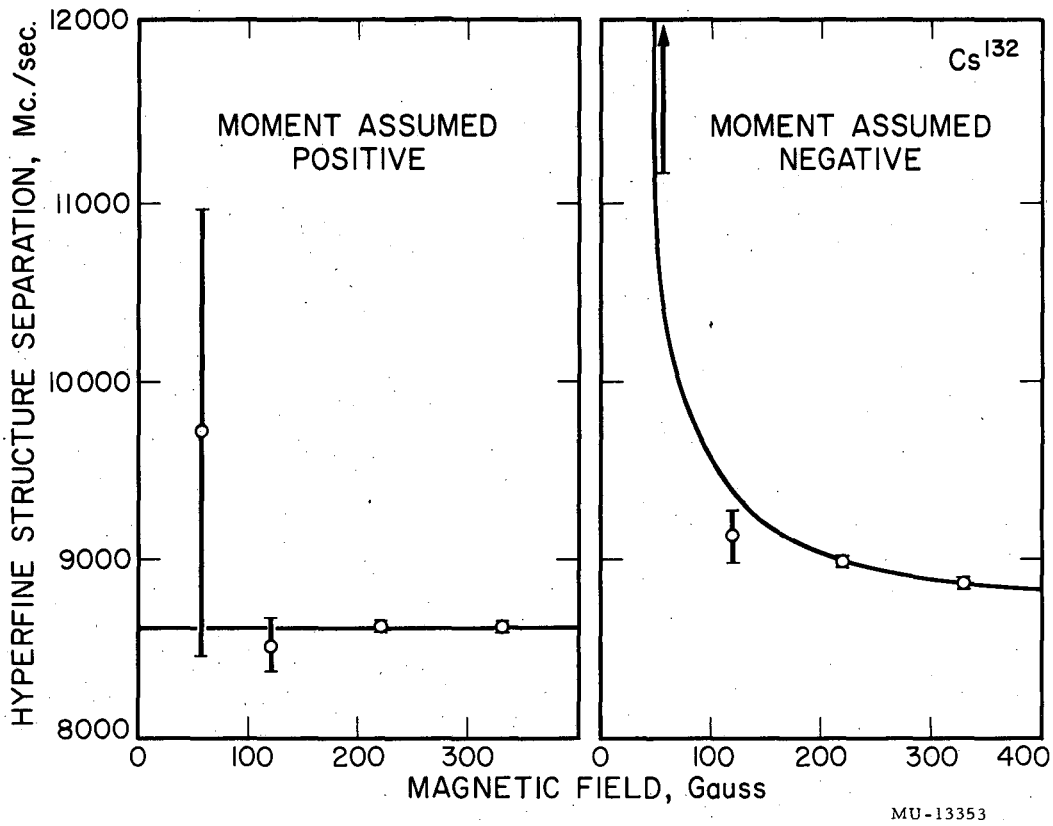

Fig. 32. $\Delta\nu$ sign curves for Cs^{132}.

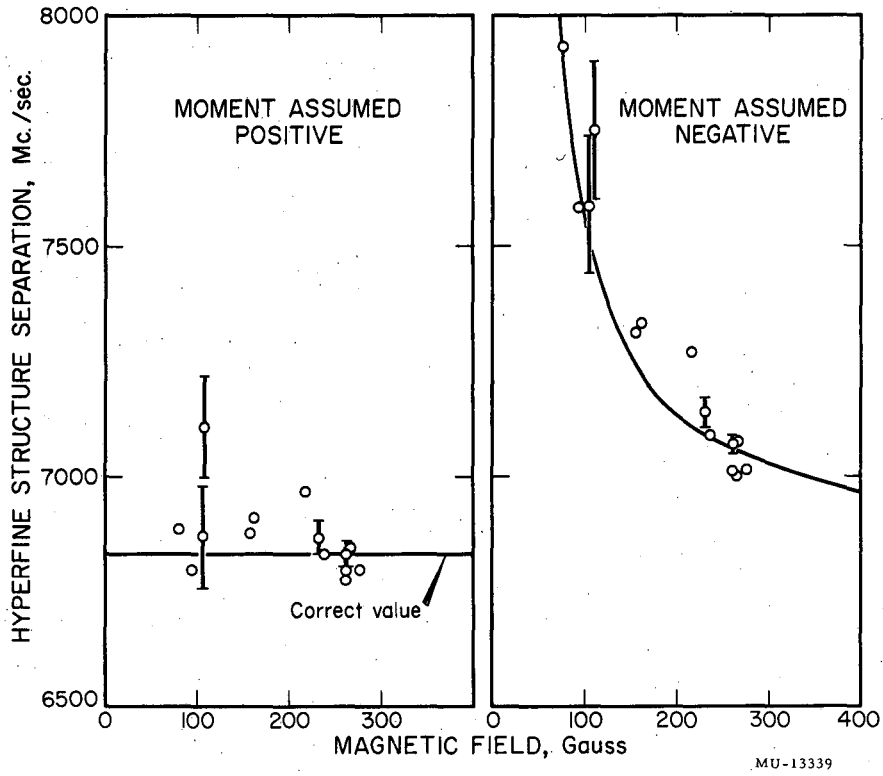

Fig. 33. Stable Rb^{87} $\Delta\nu$ sign curves for testing apparatus performance.

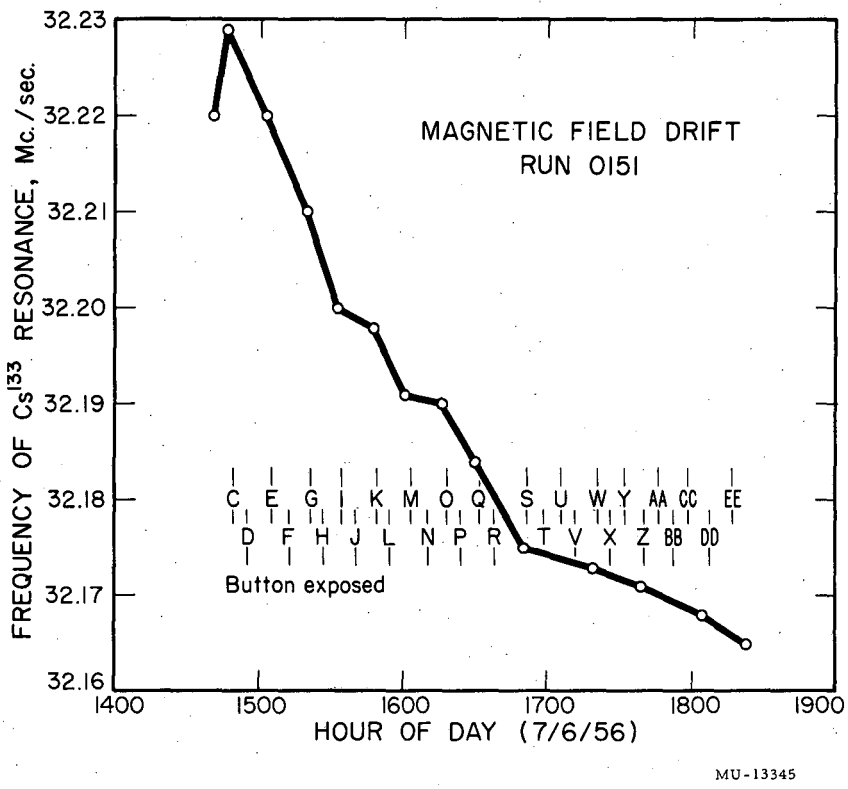

Fig. 34. Magnetic field drift, run 0151.

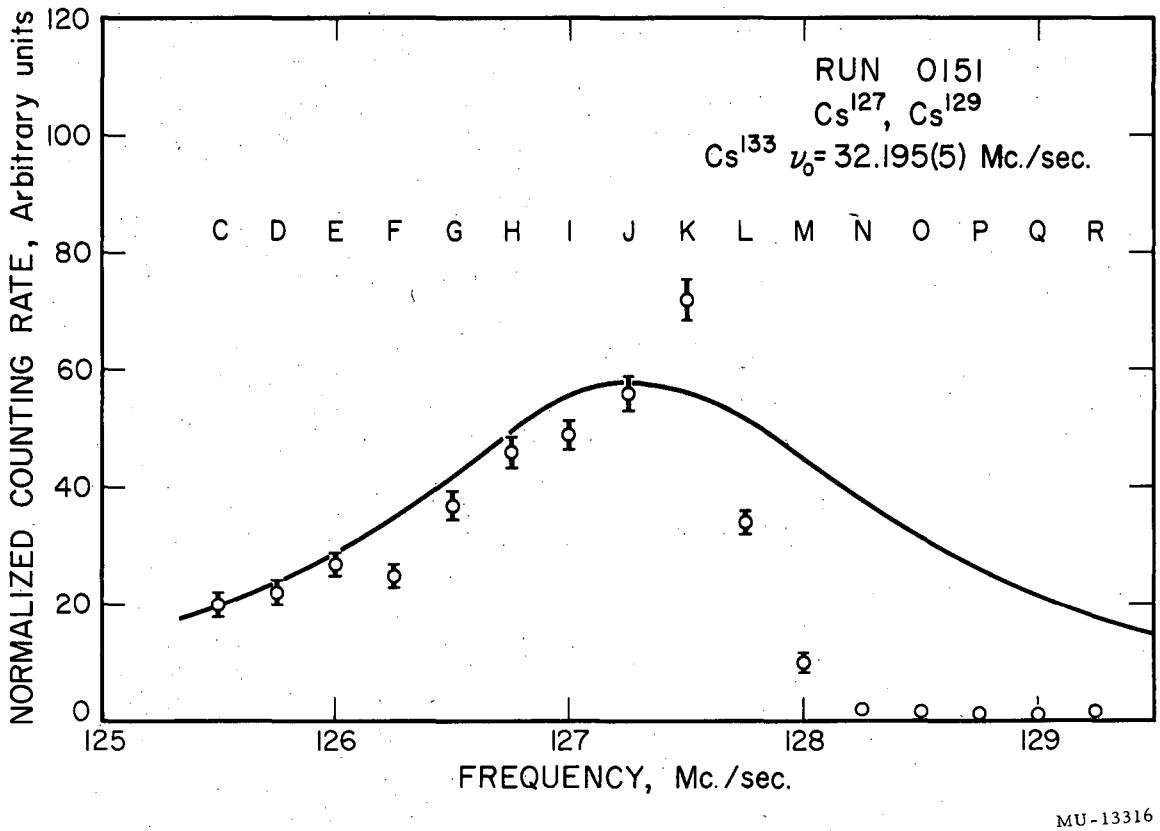

Fig. 35. Cs^{127}, Cs^{129} resonance curve, run 0151.

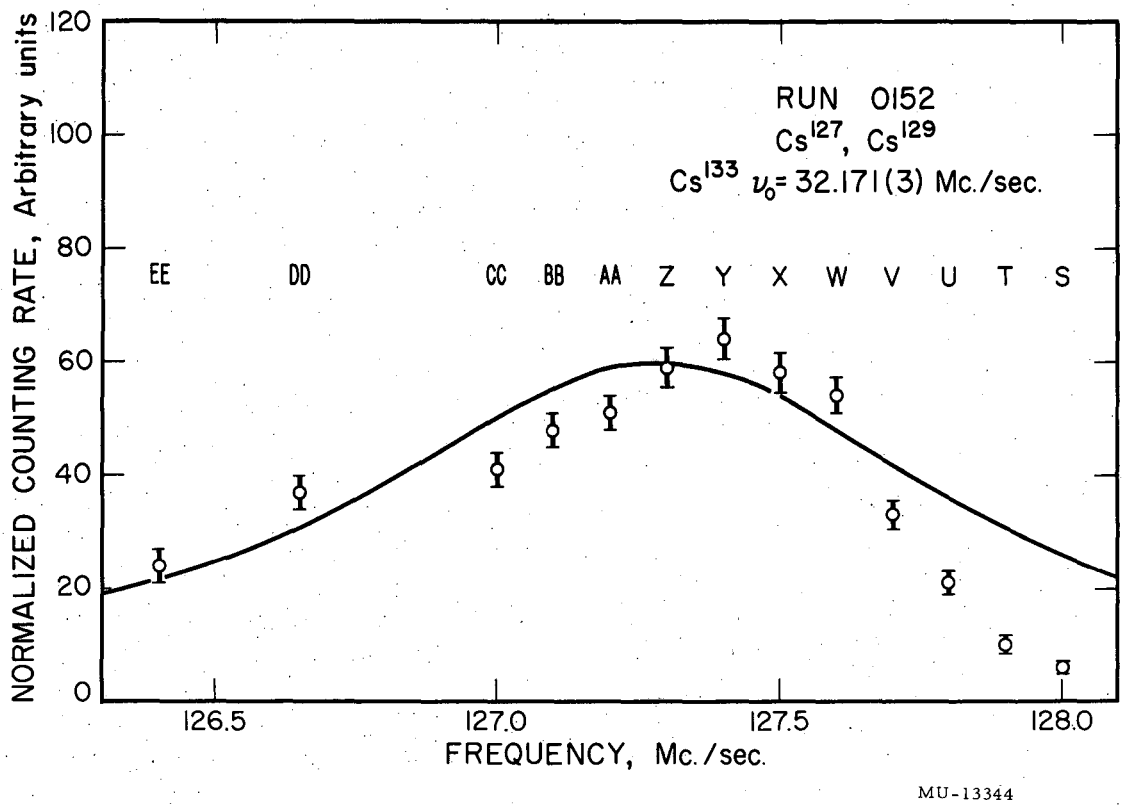

Fig. 36. Cs^{127}, Cs^{129} resonance curve, run 0152.

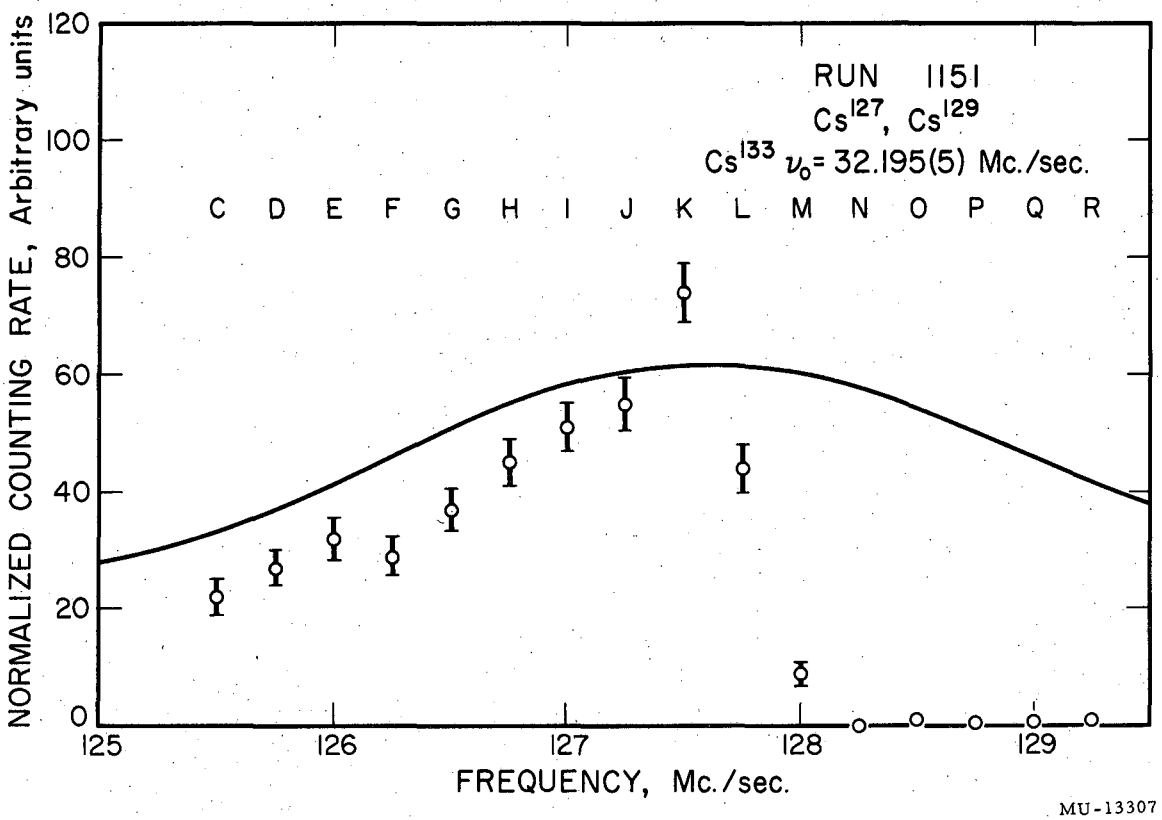

Fig. 37. Cs^{127}, Cs^{129} resonance curve, run 1151.

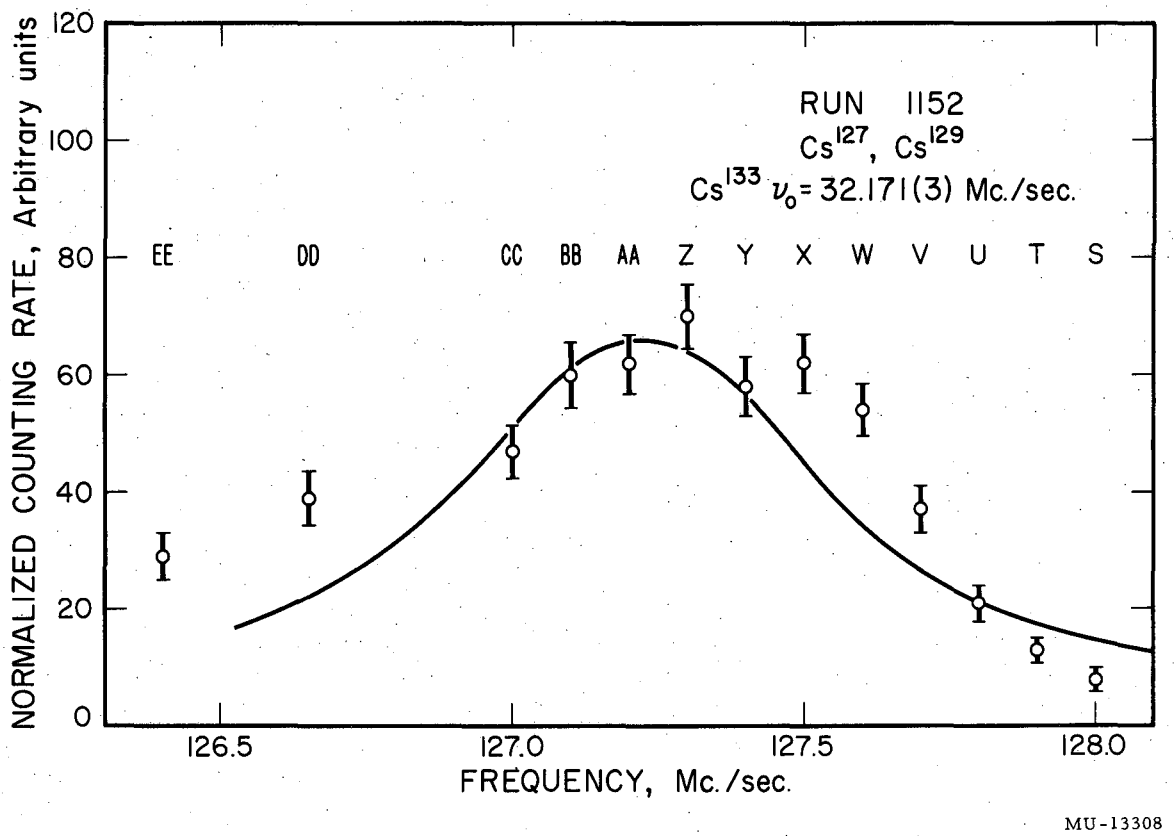

Fig. 38. Cs^{127}, Cs^{129} resonance curve, run 1152.

Fig. 37. Cs^{127}, Cs^{129} resonance curve.

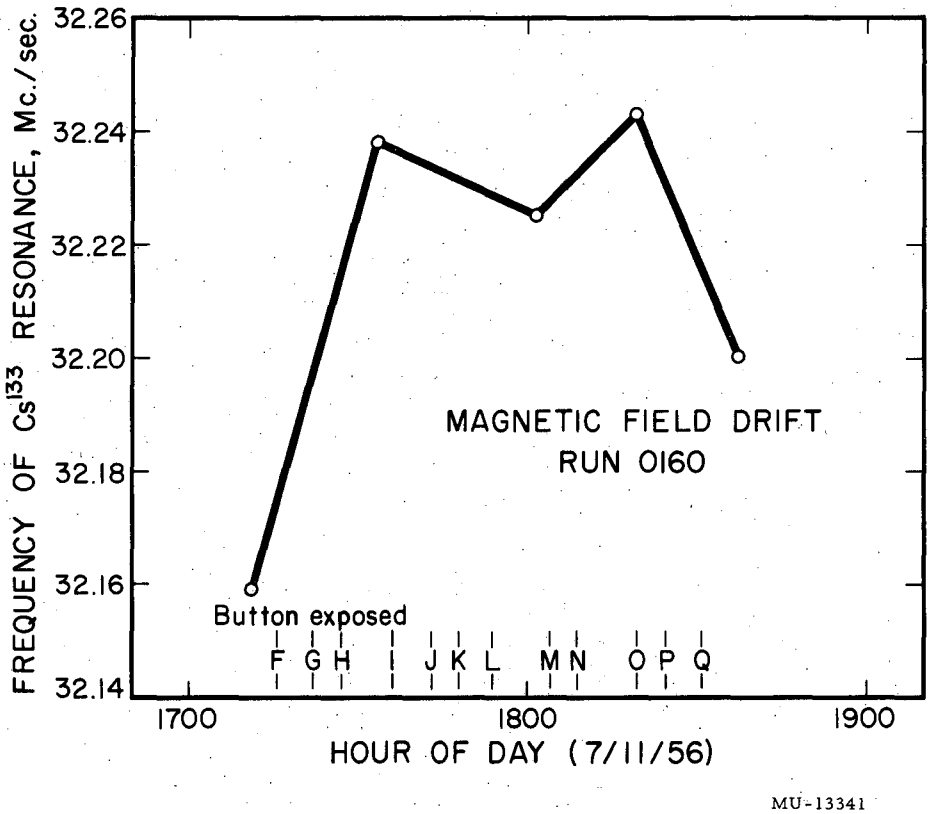

Fig. 39. Magnetic field drift, run 0160.

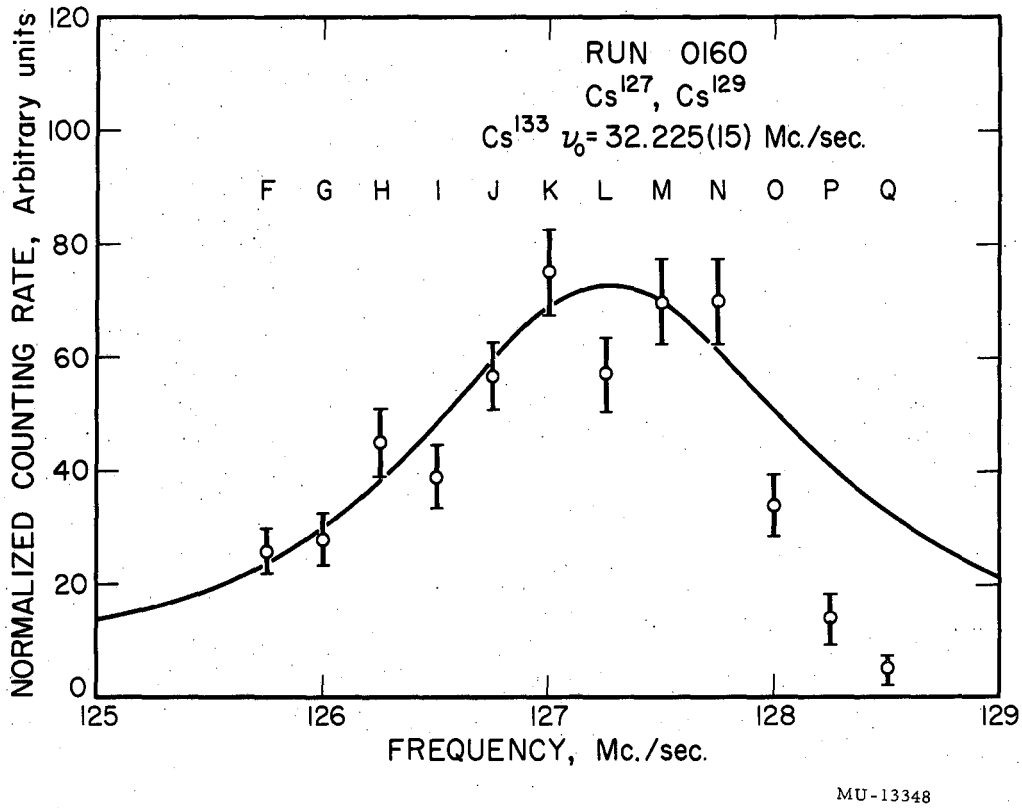

Fig. 40. Cs^{127}, Cs^{129} resonance curve, run 0160.

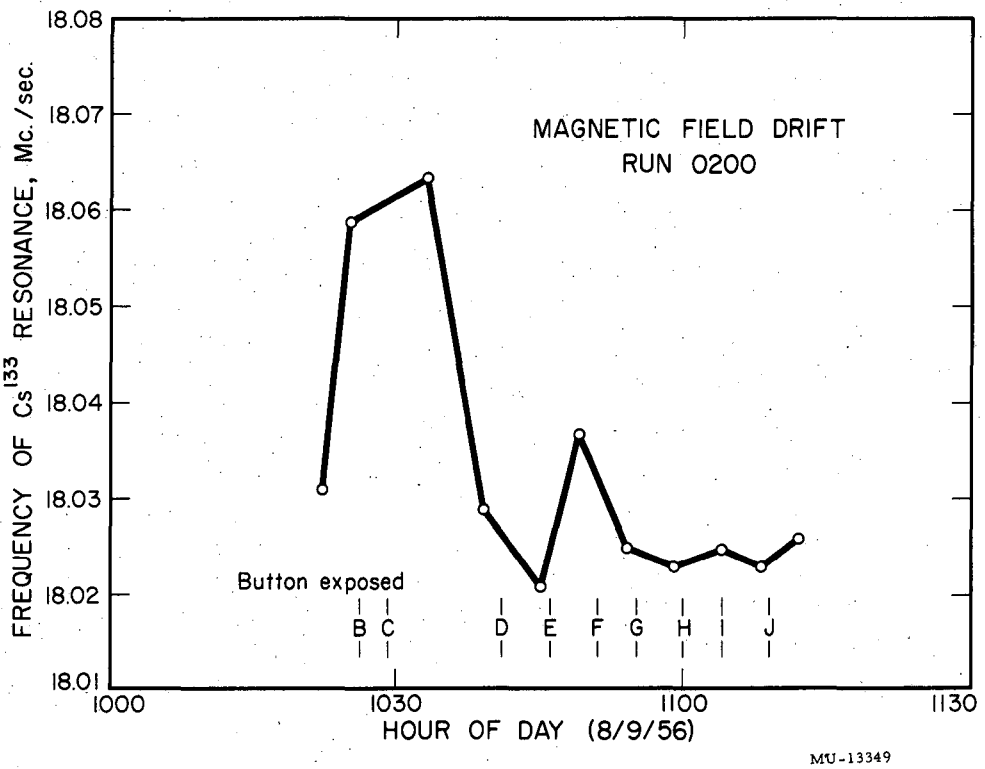

Fig. 41. Magnetic field drift, run 0200.

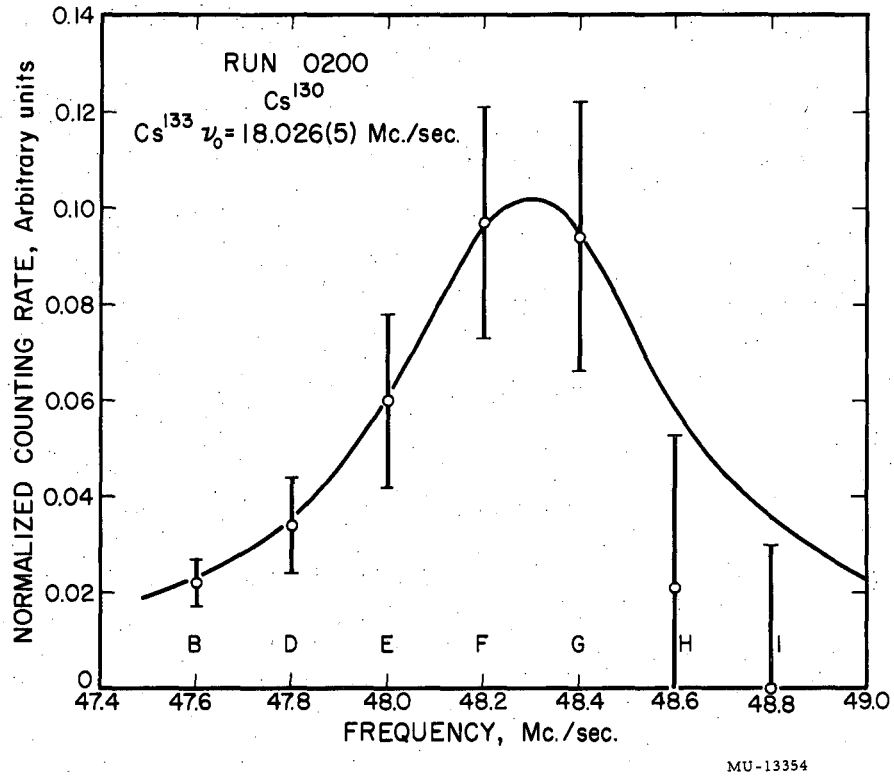

Fig. 42. Cs^{130} resonance curve, run 0200.

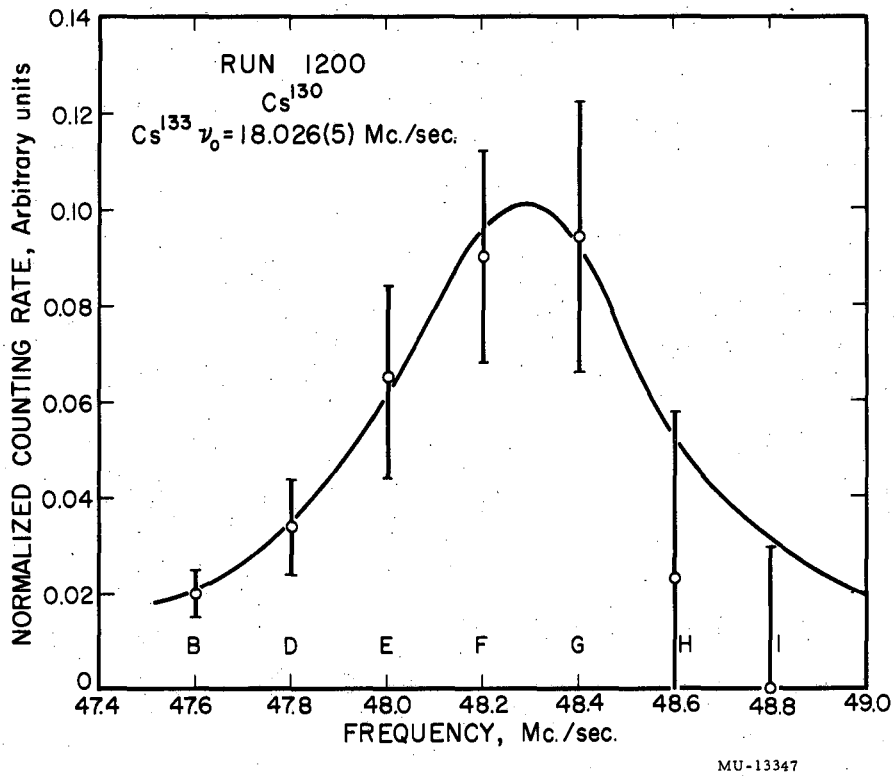

Fig. 43. Cs^{130} resonance curve, run 1200.

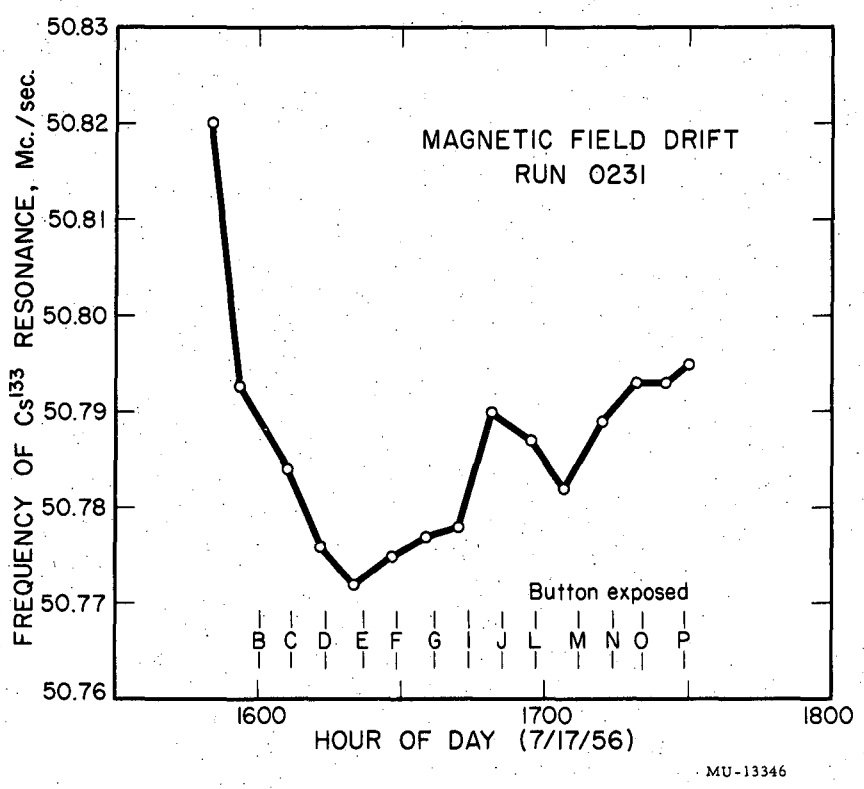

Fig. 44. Magnetic field drift, run 0231.

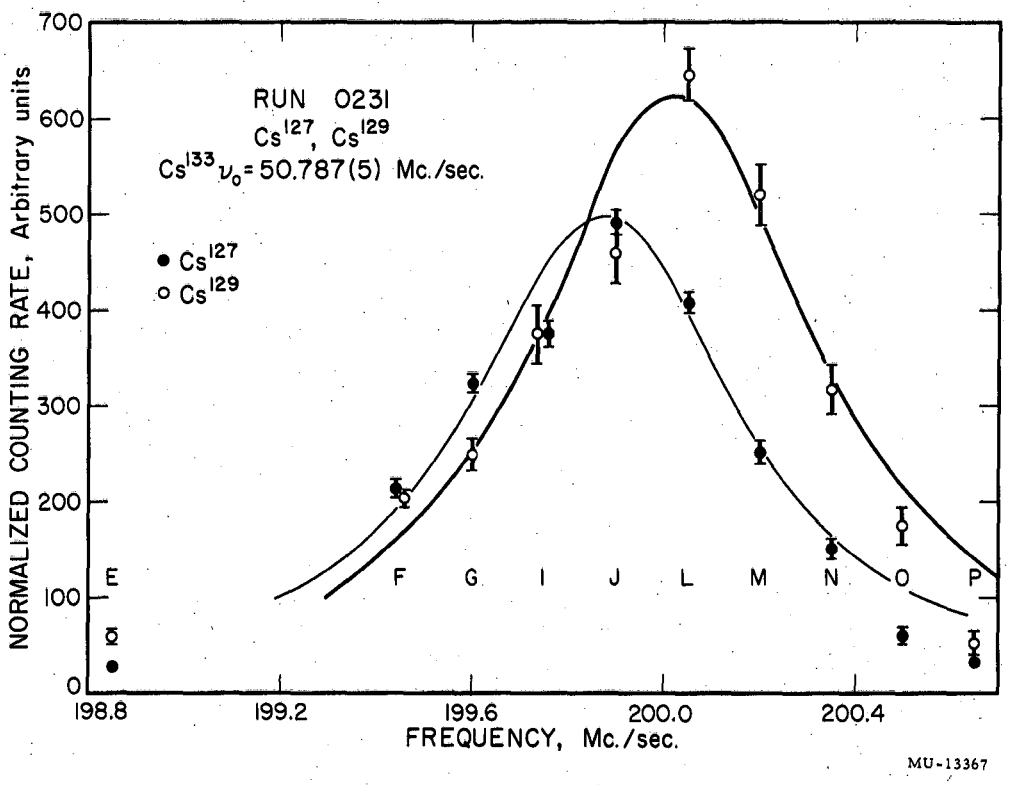

Fig. 45. Cs^{127} and Cs^{129} resonance curves, run 0231.

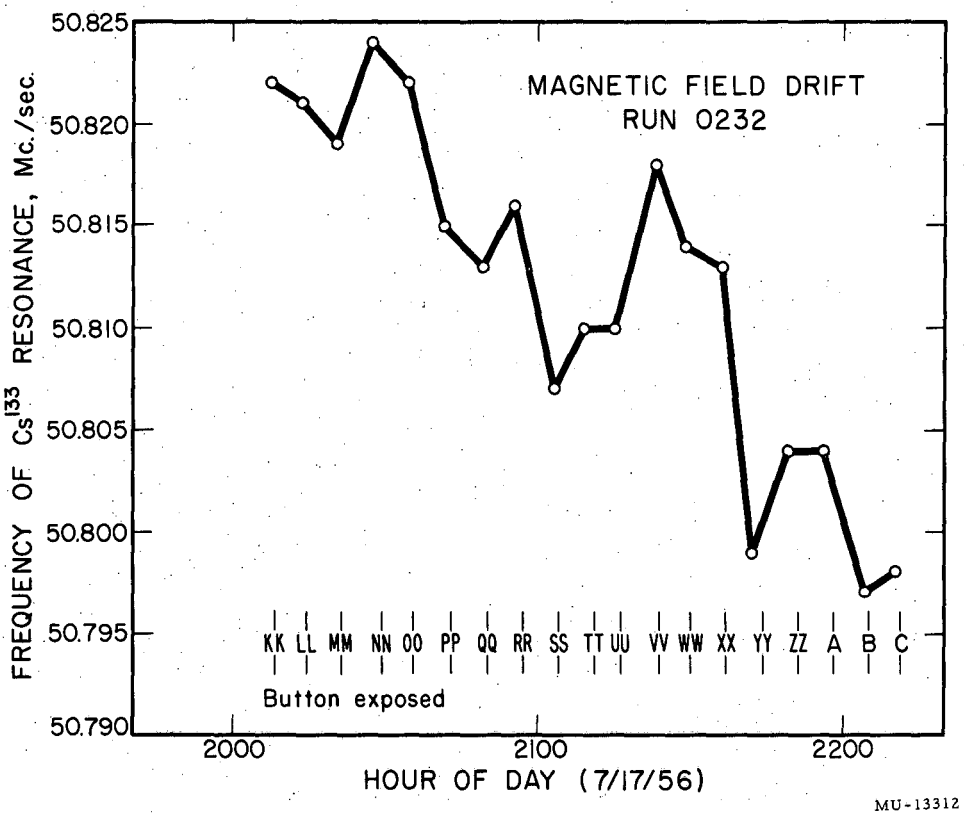

Fig. 46. Magnetic field drift, run 0232.

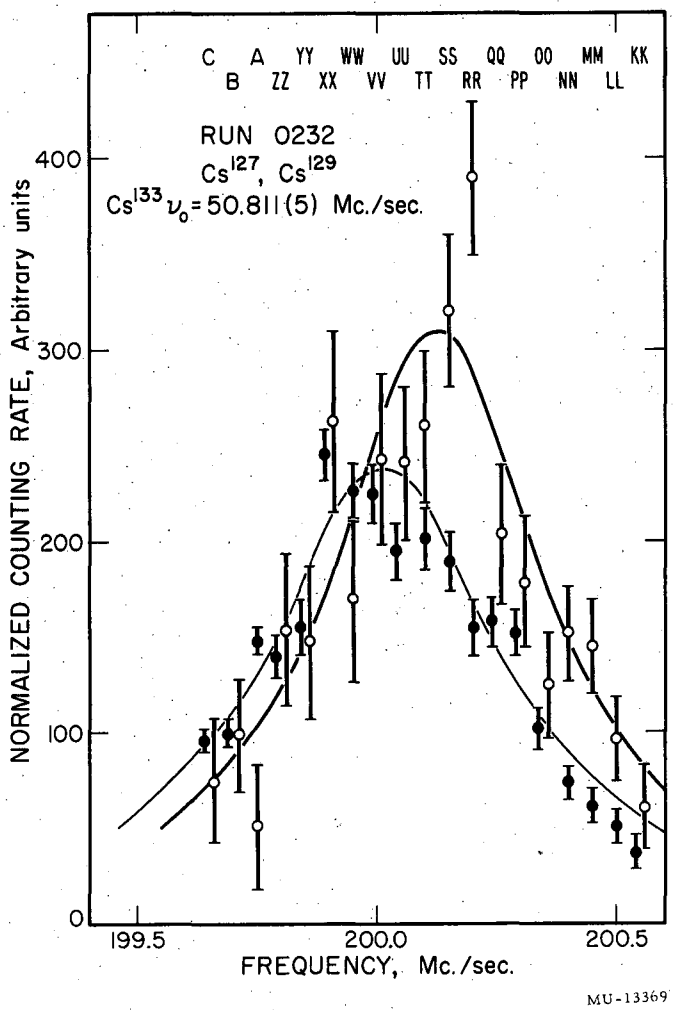

Fig. 47. Cs^{127} and Cs^{129} resonance curves, run 0232.

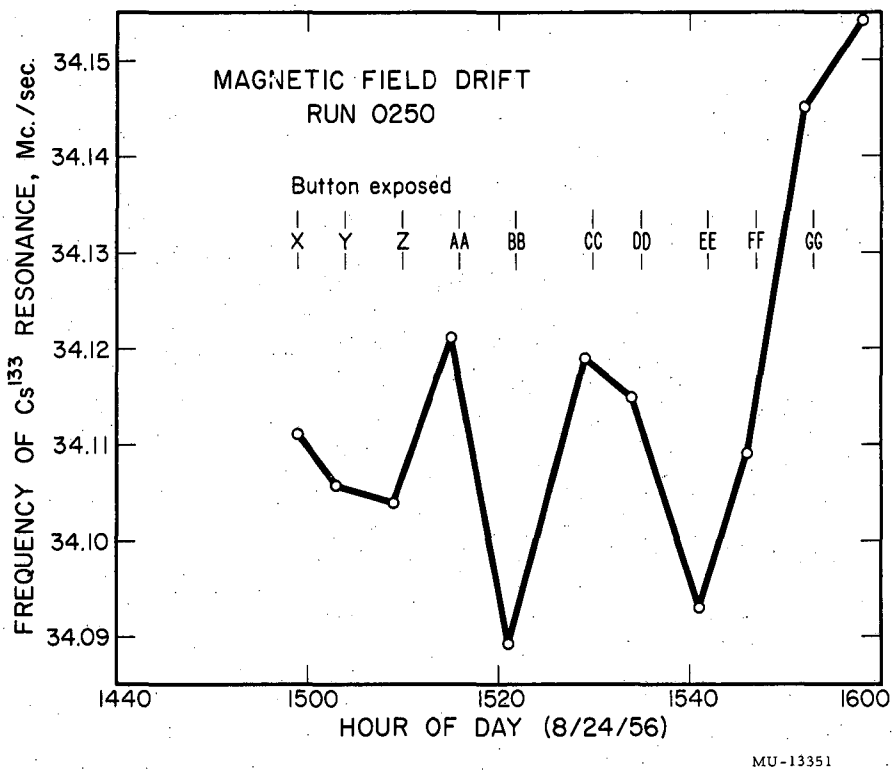

Fig. 48. Magnetic field drift, run 0250.

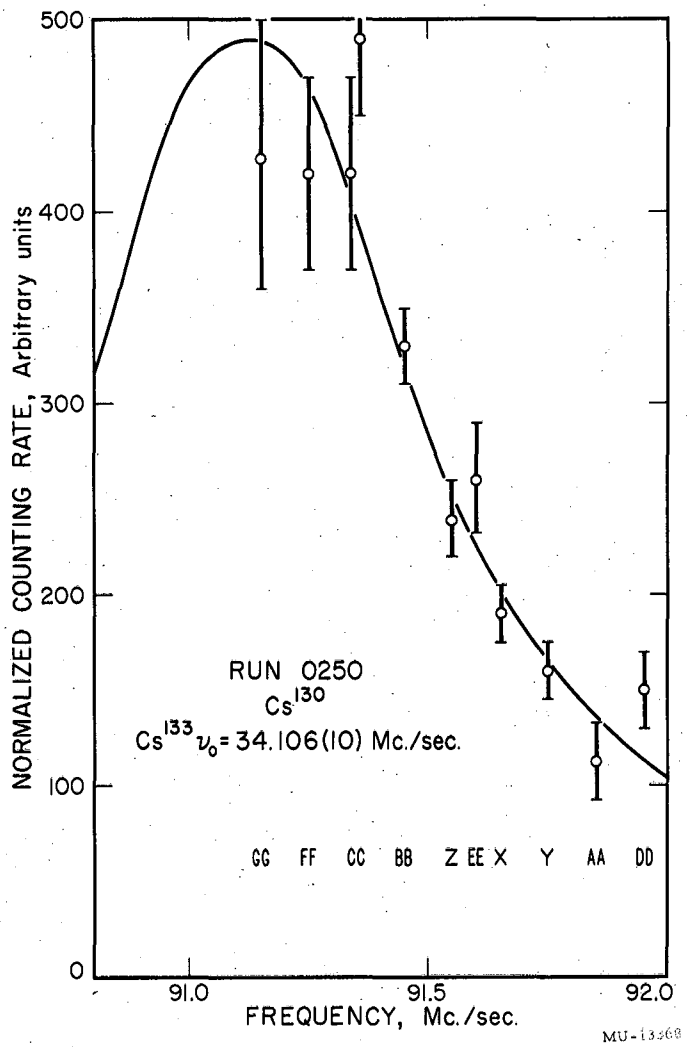

Fig. 49. Cs^{130} resonance curve, run 0250.

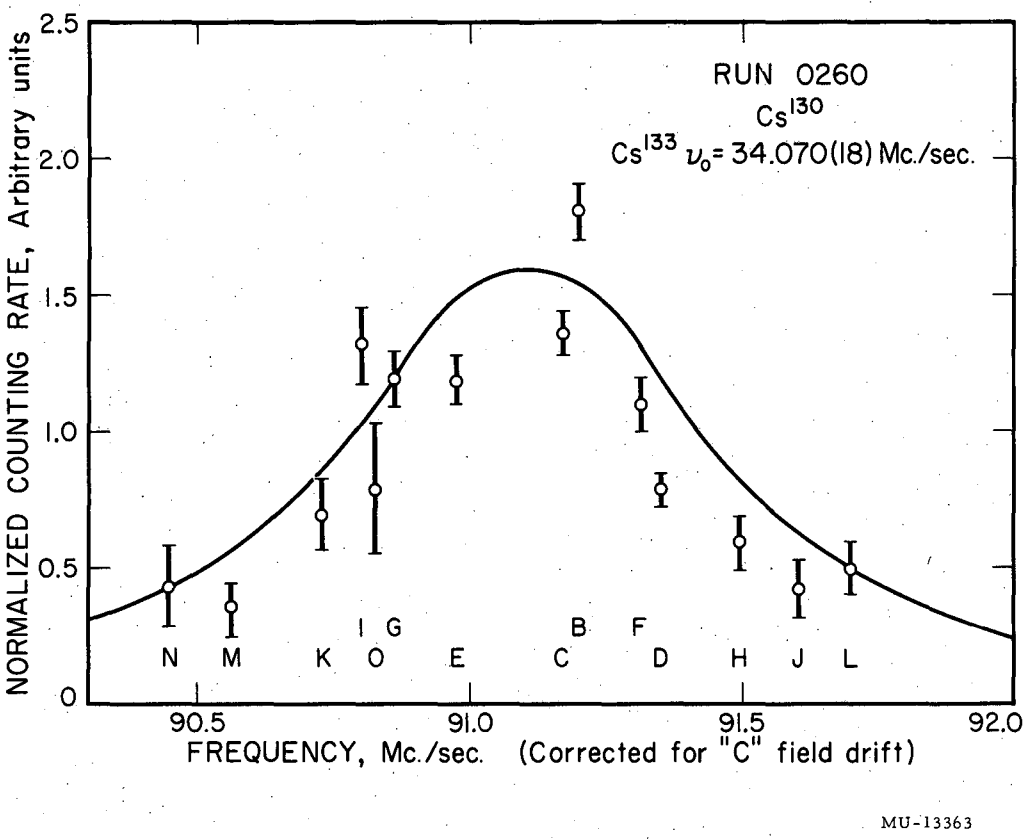

Fig. 50. Magnetic field drift, run 0260.

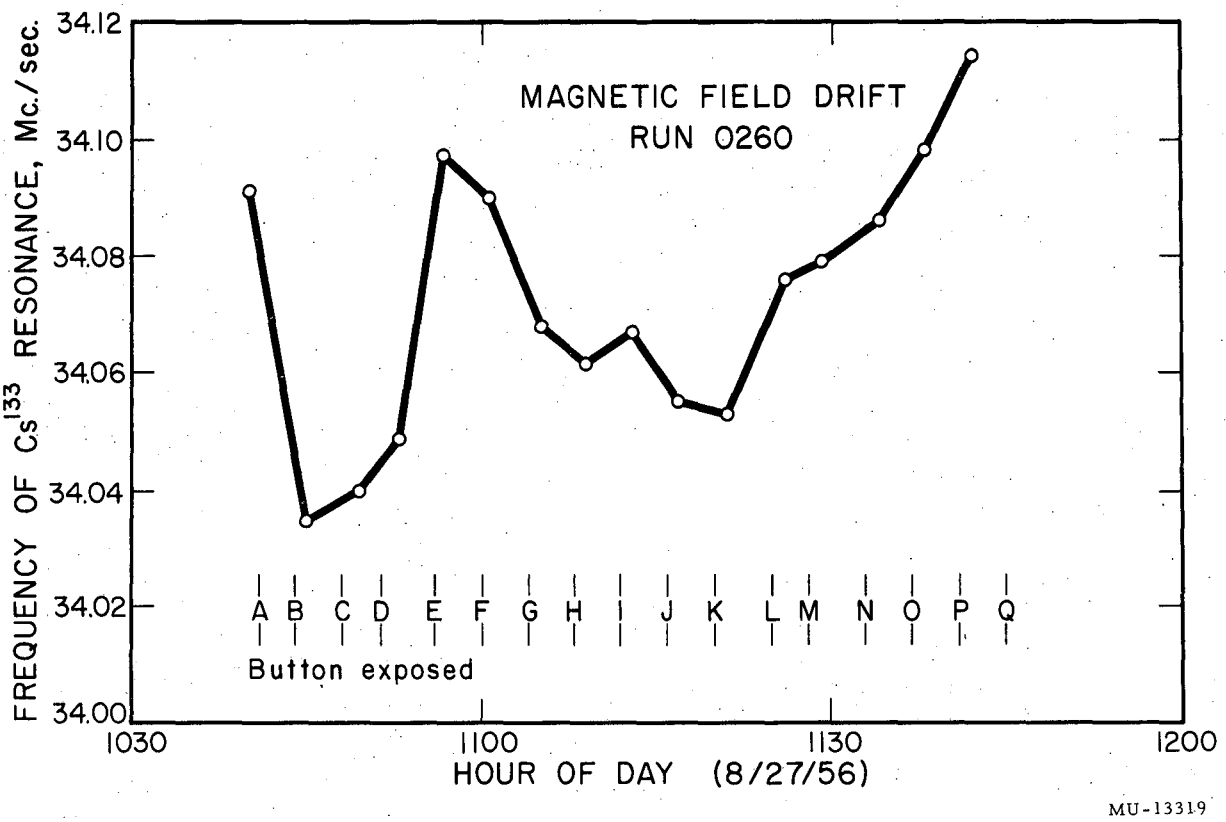

Fig. 51. Cs^{130} resonance curve, run 0260.

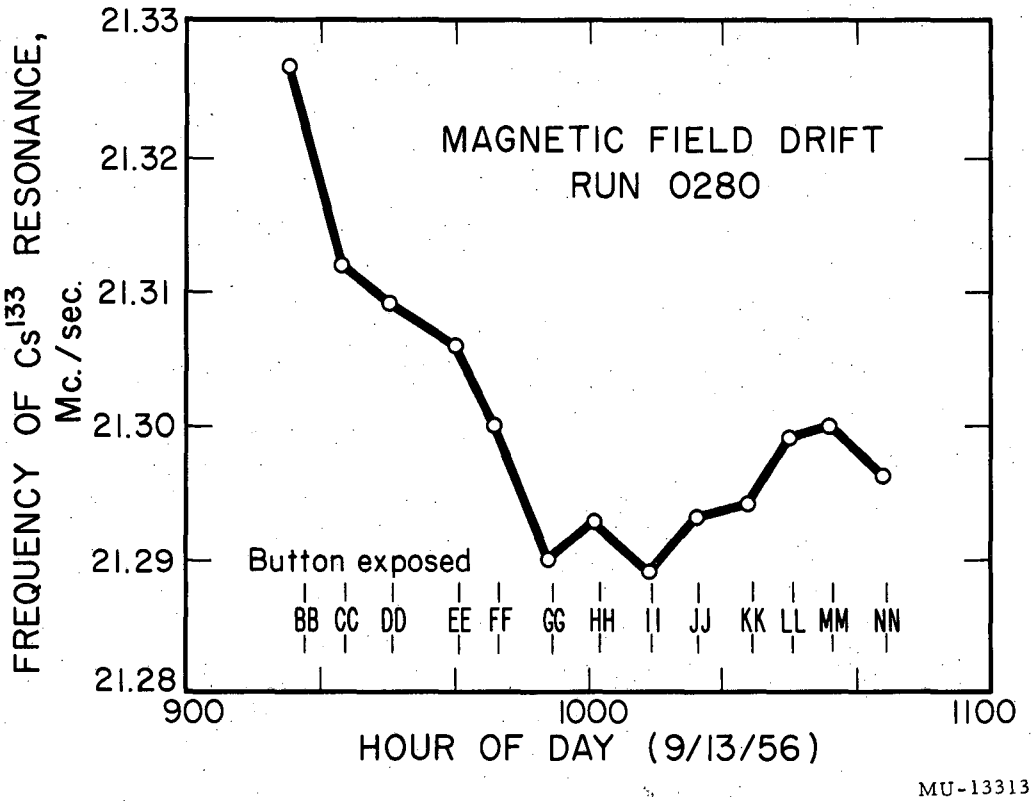

Fig. 52. Magnetic field drift, run 0280.

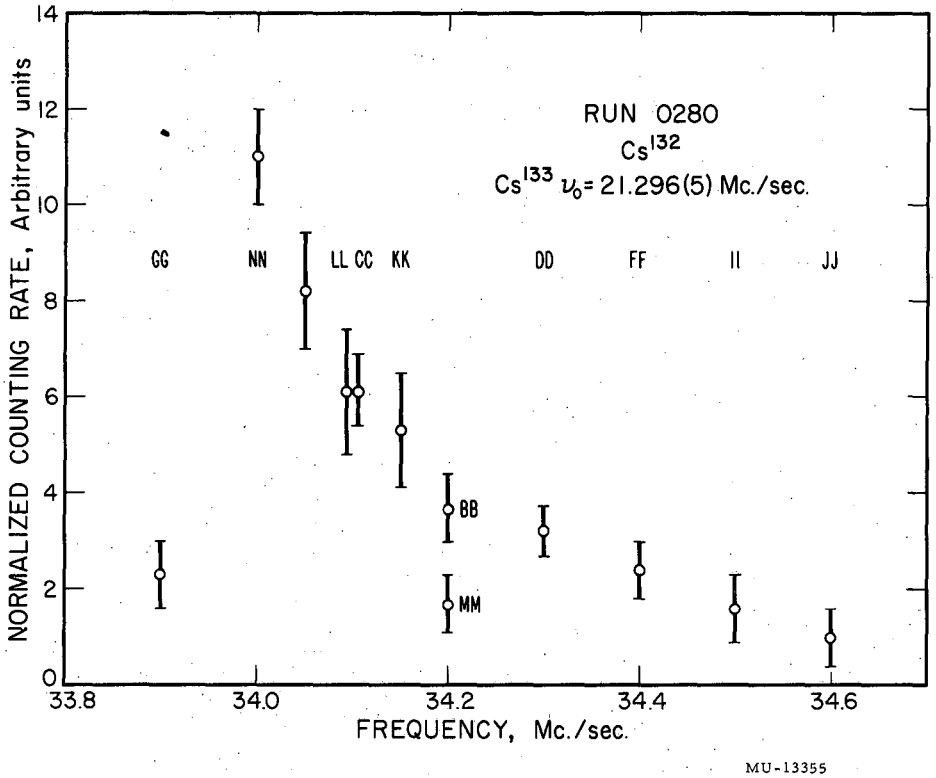

Fig. 53. Cs^{132} resonance curve, run 0280.

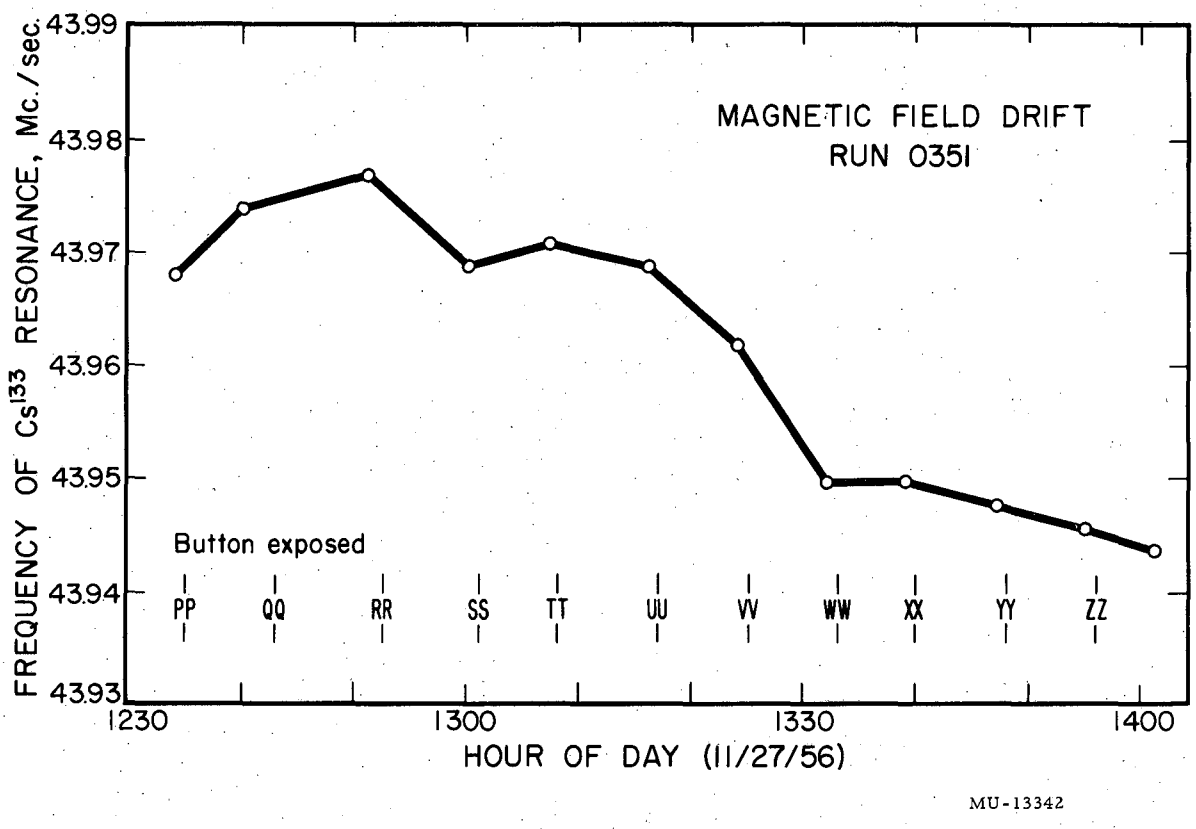

Fig. 54. Magnetic field drift, run 0351.

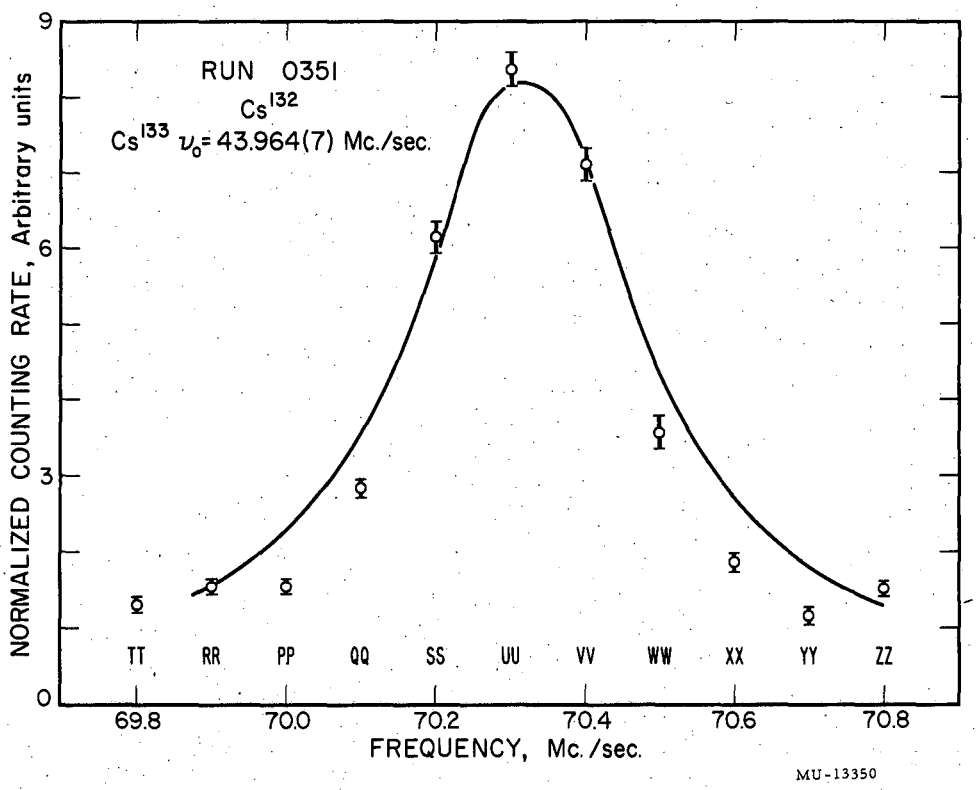

Fig. 55. Cs^{132} resonance curve, run 0351.

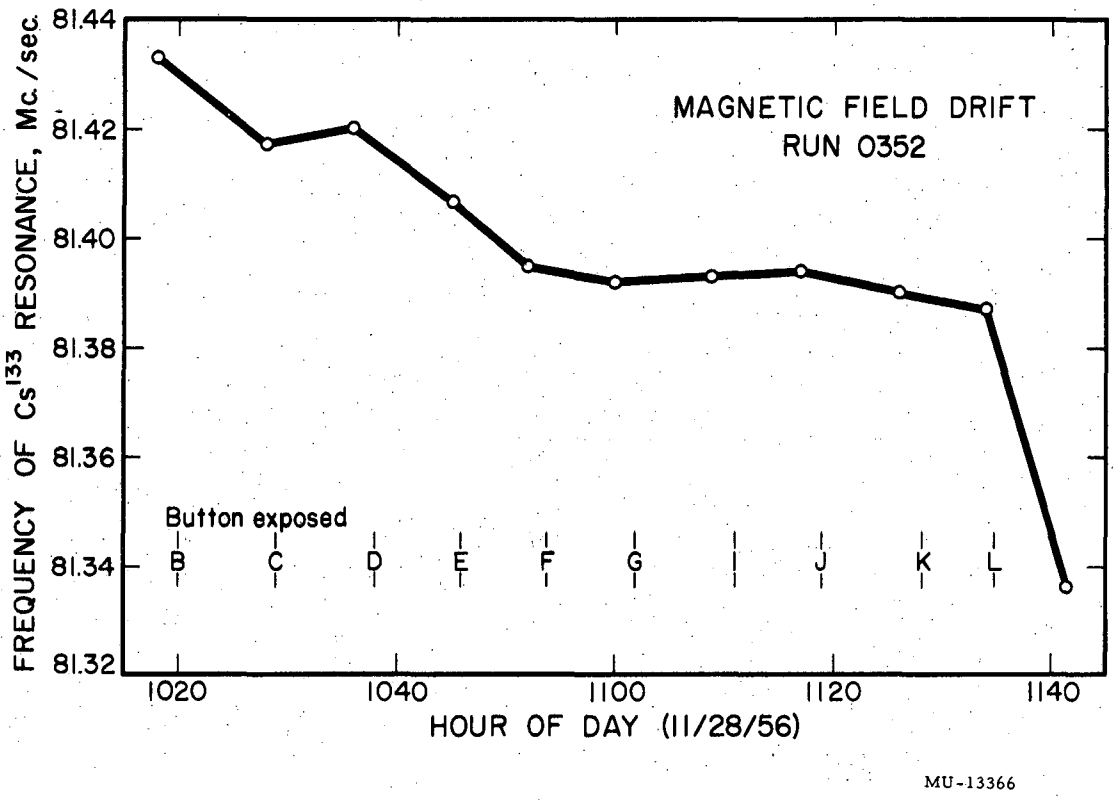

Fig. 56. Magnetic field drift, run 0352.

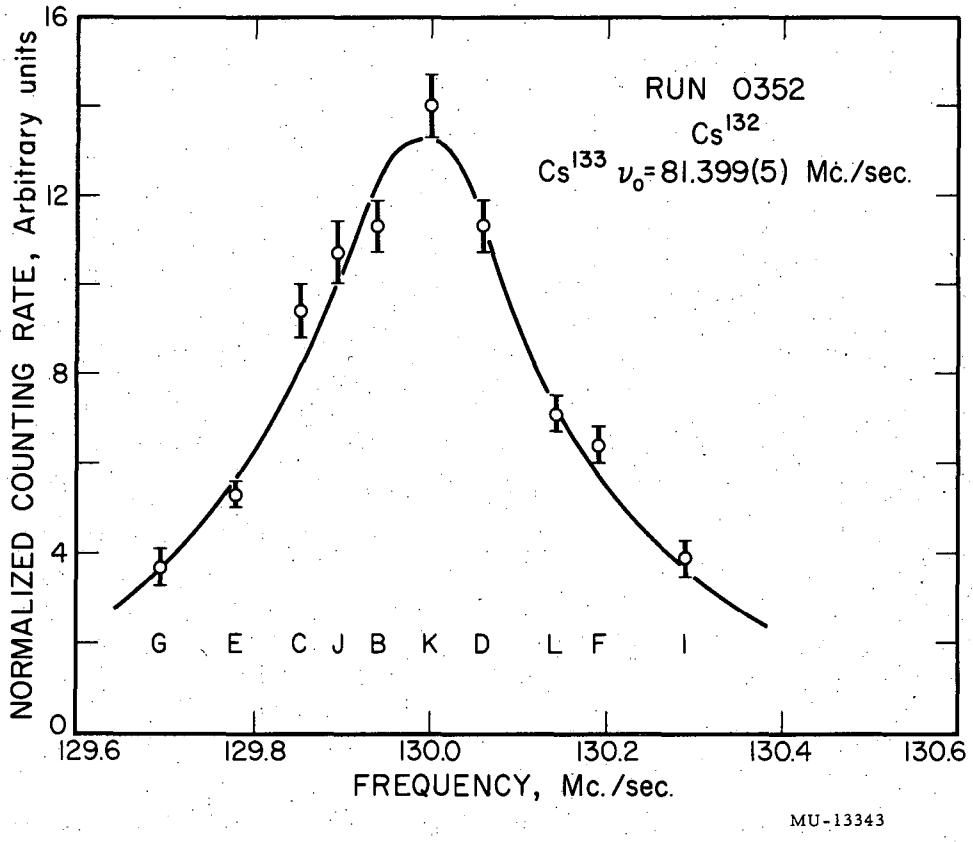

Fig. 57. Cs^{132} resonance curve, run 0352.

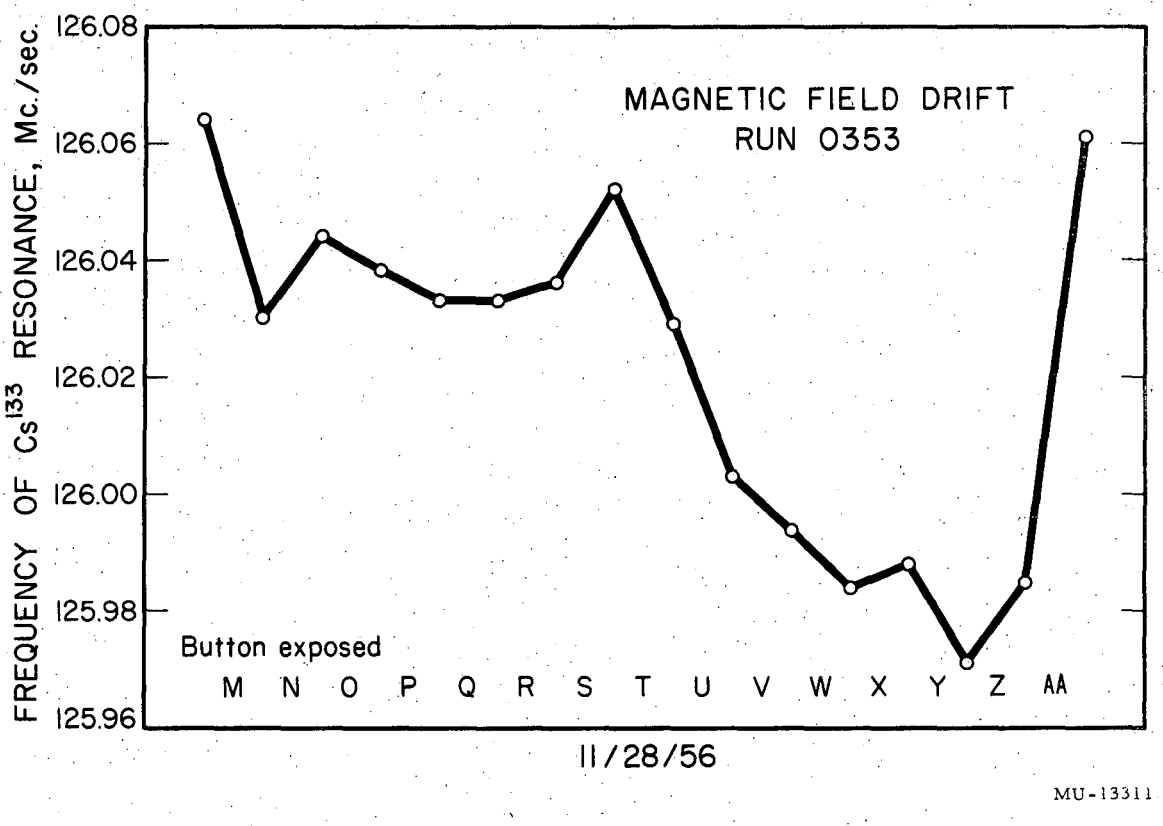

Fig. 58. Magnetic field drift, run 0353.

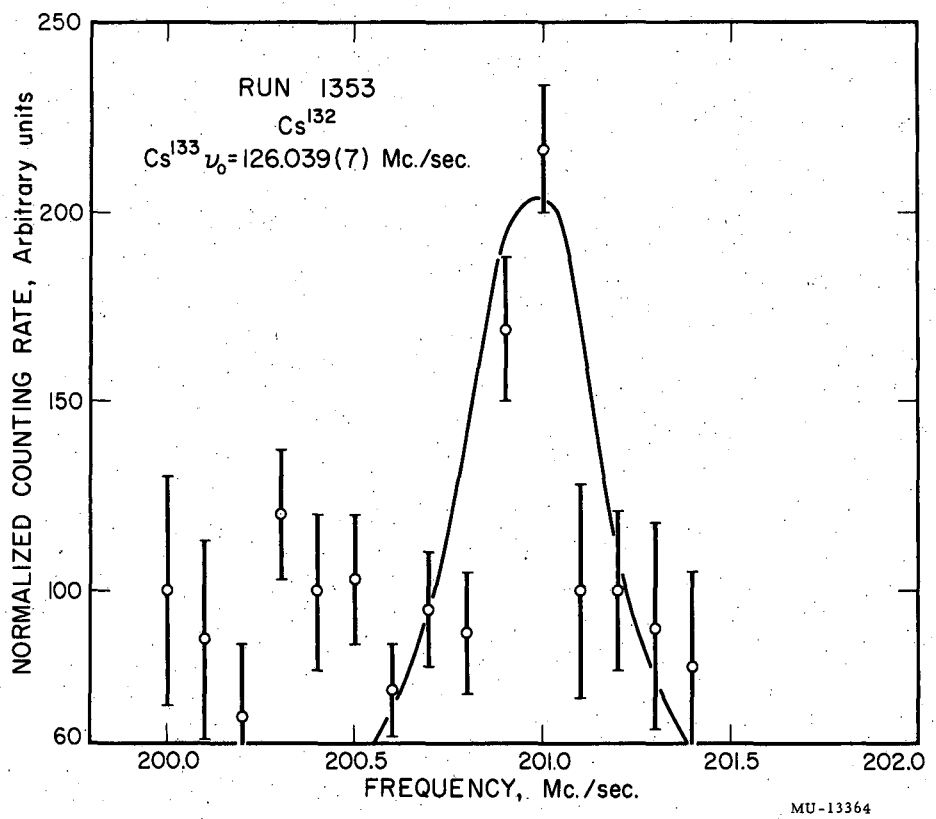

Fig. 59. Cs^{132} resonance curve, run 1353.

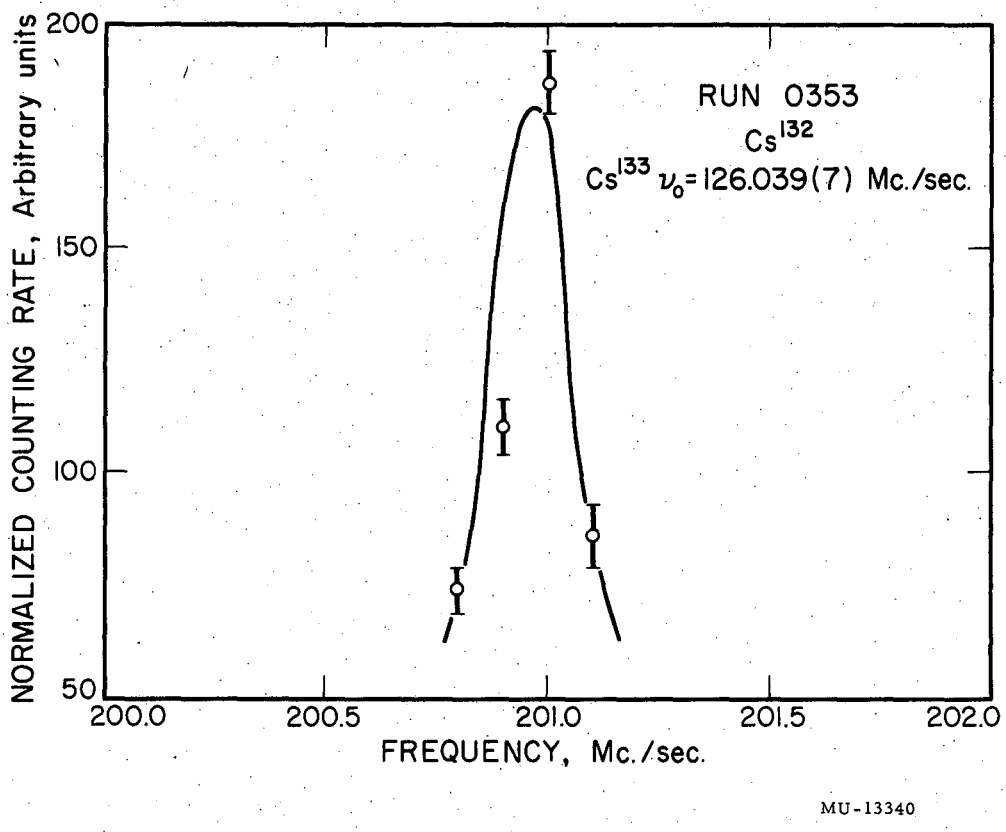

Fig. 60. Cs^{132} resonance curve, run 0353.

VIII. DISCUSSION

The measurement of spin 1/2 for Cs^{127} and Cs^{129} is totally unexpected on the basis of the simple shell model (MAY 55). The simple odd-particle shell model would predict a spin of 7/2 or 5/2 for these isotopes, since Cs^{133}, Cs^{135}, and Cs^{137} have I = 7/2 (MIL 36, DAV 49, 49A), and Cs^{131} has I = 5/2 (BEL 53). Also it is not possible to couple particles in j = 7/2 or j = 5/2 levels to give a spin of 1/2. The $3s_{1/2}$ level which could give the observed spin in the simple shell model lies at the top of the 50 to 82 proton shell. For Tl^{203} and Tl^{205}, an odd proton in this shell gives a magnetic moment of about +1.6 n.m. (see p. 79, MAY 55), which is not too far from the observed value of +1.5 n.m. If a single proton should exist in the $s_{1/2}$ level, many lower levels ($d_{5/2}$, $h_{11/2}$, and $d_{3/2}$) would remain unoccupied. This configuration, therefore, seems unlikely unless a reordering of levels occurs for Cs^{127} and Cs^{129}. The observed magnetic moment lies approximately midway between the Schmidt limits of -.3 and +2.8 nuclear magnetons.

Another way of attempting to explain the observed results would be by the recent Bohr-Mottelson "unified model" or "collective model", in which the odd particle and the deformed core share the total angular momentum (BOH 51, 53). Details of the single particle levels in deformed potentials are discussed by Nilsson and Mottelson (NIL 55, MOT 55). It is found that some of the degeneracy of the single particle moving in a spherical potential is removed by the deformed core. A quantum number Ω which represents the component of the single particle angular momentum on the nuclear axis, now specifies the levels resulting from removing the degeneracy of the

spherical well level. Each of these levels is still doubly degenerate, corresponding to $\pm\Omega$. The relative spacing of the levels is specified by various values of Ω, depending upon the degree of core deformation. Nilsson diagrams (NIL 55, MOT 55) show the theoretical variation in single particle energy as a function of core deformation. Although certain level energies decrease monotonically with deformation, one must remember that the ultimate configuration will be determined by an energy minimum of the whole nucleus. Therefore, some point will be reached where an increase in the energy of the deformed core is greater than the corresponding decrease in energy of the single particle moving in the deformed core potential. In this way an equilibrium is reached which depends, to some extent, upon the resistance of a nucleus to deformation. For neutron or proton numbers near closed shells of 2, 8, 20, 28, 50, 82, and 126, the nucleus is observed to be quite resistant to deformation. On the other hand, the large quadrupole moments observed for elements away from closed shell configurations show that large nuclear deformations exist in these regions.

The series of cesium isotopes, Cs^{137}, Cs^{135}, Cs^{133}, Cs^{131}, Cs^{129}, and Cs^{127}, represent neutron configurations extending away from a closed shell of 82 neutrons as in Cs^{137}. The spin of 7/2 for Cs^{137}, Cs^{135}, and Cs^{133} are in good agreement with the single odd proton moving in a spherical potential, which is associated with closed shells of nucleons. The spin of 5/2 for Cs^{131} and 1/2 for Cs^{129} and Cs^{127} are then to be explained by the single odd proton deforming the core and consequently deforming the potential in which it moves. Presumably the core of Cs^{129} and Cs^{127} is more easily deformed than that of Cs^{131} due to their greater separation

from the closed shell configuration of 82 neutrons.

Uretsky (URE 57) has calculated the magnetic moments to be expected for Cs^{129} and Cs^{127} on the basis of the level scheme given by Mottelson and Nilsson (MOT 55). He, using the notation of Mottelson and Nilsson, finds the following equilibrium magnetic moments:

Cs^{129} and Cs^{127}	Spin	Proton	Level	Deformation, η	μ n.m.
	1/2	$d_{5/2}$	#34	+3	+2.02
	1/2	$g_{7/2}$	#30	-4	+1.38

The $g_{7/2}$ proton, which has a core of large oblate deformation, appears more consistent with the experimentally determined magnetic moment.

In future work on these isotopes, it would be desirable to operate at a sufficiently high frequency for the Cs^{127} and Cs^{129} peaks to be resolved. Use of Cs^{129} made from Xe^{129} would remove any interference caused by Cs^{127}. Similarly the production of Cs^{127} over Cs^{129} may be further enhanced by using thinner targets than those described here.

The observed spin of 1 for Cs^{130} may be due to a contribution of 1/2 from the protons, as in Cs^{127} and Cs^{129} coupled to an $s_{1/2}$ neutron, as in Xe^{129}. Using the magnetic moments of these nuclei and assuming a simple vector model coupling, the magnetic moment for coupling to spin 1 is +.68 nuclear magnetons. This value is one-half of the observed moment of Cs^{130}.

Due to the urgency of other work, investigation of the hyperfine structure of Cs^{130} ceased after the magnetic moment was obtained to an accuracy of 6%. This was insufficient to permit a definite evaluation

of the sign of the magnetic moment. Since the details of the technique of performing the experiment have been worked out, a determination of the sign of the moment and more accurate hyperfine structure separation measurement will probably be made in the near future.

The results of I = 2 for Cs^{132} may be due to the coupling of a $g_{7/2}$ proton as in Cs^{133}, and a $d_{3/2}$ neutron in Xe^{131}. A simple vector model addition of these gives a magnetic moment of +1.74 nuclear magnetons, as compared to the measured value of +2.22 nuclear magnetons. The error of ±30 mc/sec in the hyperfine structure separation will have to be improved slightly before a search for the $\Delta F = \pm 1$ transitions are sought.

The measurements made here represent a preliminary step toward more difficult hyperfine structure anomaly determinations, which will probably be made within the next few years.

ACKNOWLEDGMENTS

I wish to express my appreciation to Professor H. B. Silsbee for introducing me to the subject of atomic and molecular beams and for his interest and assistance, especially in the systematic processing of data, during all phases of this research. I am indebted to Professor W. A. Nierenberg, who suggested the research topic described in this thesis, for his guidance and untiring enthusiasm throughout the course of this work. It has been a pleasure to associate with J. L. Worcester, R. J. Sunderland, and W. B. Ewbank. With them, many hours have been spent in constructing and operating equipment, taking and interpreting data, and in discussions.

Helpful discussions with Dr. J. C. Hubbs, Dr. E. Lipworth, Dr. G. O. Brink and R. Marrus are also acknowledged. S. Goldberg prepared most of the sulfur-coated buttons used in these experiments. The crew of the sixty-inch Crocker cyclotron is to be commended for their skillful handling of the cyclotron during our numerous bombardments.

I am grateful to Mrs. Eleanor Thornhill for typing this thesis.

The work described here has been made possible through financial support from the U. S. Office of Naval Research and the U. S. Atomic Energy Commission.

REFERENCES

BEL 53 E. H. Bellamy and K. F. Smith, Phil. Mag. 44, 33, 1953.

BEM 53 G. Bemski, Ph.D. Thesis, University of California, 1953.

BES 42 W. H. Bessey and O. C. Simpson, Chem. Rev. 30, 234, 1942.

BLA 52 J. M. Blatt and V. F. Weisskopf, Theoretical Nuclear Physics (John Wiley and Sons, New York, 864 pp., 1952).

BLE 53 E. Bleuler, A. K. Stebbins, and D. J. Tendam, Phys. Rev. 90, 460, 1953.

BIT 49 F. Bitter, Phys. Rev. 75, 1326, 1949.

BOH 50 A. Bohr and V. F. Weisskopf, Phys. Rev. 77, 94, 1950.

BOH 51 A. Bohr, Phys. Rev. 81, 134, 1951.

BOH 51A A. Bohr, Phys. Rev. 81, 331, 1951.

BOH 53 A. Bohr and B. R. Mottelson, Kgl. Danske Videnskab. Selskab, Mat.-fys. Medd. 27, 16, 1953.

BRE 28 G. Breit, Nature 122, 649, 1928.

BRE 30 G. Breit, Phys. Rev. 35, 1447, 1930.

BRE 31 G. Breit and I. I. Rabi, Phys. Rev. 38, 2082, 1931.

BRE 33 G. Breit and L. Wills, Phys. Rev. 44, 470, 1933.

BRE 48 G. Breit and G. E. Brown, Phys. Rev. 74, 1278, 1948.

BRE 49 G. Breit, G. E. Brown, and G. B. Arfken, Phys. Rev. 76, 1299, 1949.

BRI 56 G. O. Brink, J. C. Hubbs, W. A. Nierenberg, and J. L. Worcester, Bull. Am. Phys. Soc. II, 1, 343, 1956.

BRI 57 G. O. Brink, J. C. Hubbs, W. A. Nierenberg, and J. L. Worcester, Bull. Am. Phys. Soc. II, 2, 200, 1957.

BRI 57A G. O. Brink, Ph.D. Thesis, University of California, 1957.

DAV 49 L. Davis, Phys. Rev. 76, 435, 1949.

DAV 49A L. Davis, D. E. Nagle, and J. R. Zacharias, Phys. Rev. 76, 1068, 1949.

DOG 56 W. O. Doggett, Ph.D. Thesis, University of California, 1956.

DUM 53 J. W. M. DuMond and E. R. Cohen, Rev. Mod. Phys. 25, 706, 1953.

DUN 11 L. Dunoyer, Compt. Rend. 152, 594, 1911.

EST 46 I. Estermann, Rev. Mod. Phys. 18, 300, 1946.

EVA 55 R. D. Evans, The Atomic Nucleus (McGraw-Hill Book Co., Inc., New York, 972 pp., 1955).

FER 30 E. Fermi, Z. Physik 60, 320, 1930.

FER 33 E. Fermi and E. Segre, Z. Physik 82, 729, 1933.

FER 50 E. Fermi, Nuclear Physics (University of Chicago Press, Chicago, 248 pp., 1950, revised 1953).

FIN 50 R. W. Fink, F. L. Reynolds, D. H. Templeton, Phys. Rev. 77, 614, 1950.

FOX 35 M. Fox and I. I. Rabi, Phys. Rev. 48, 746, 1935.

FRA 31 R. G. J. Fraser, Molecular Rays (Cambridge University Press, Cambridge, 204 pp., 1931).

FRA 37 R. G. J. Fraser, Molecular Beams (Methuen and Co., Ltd., London, 70 pp., 1937).

GHO 48 S. N. Ghoshal, Phys. Rev. 73, 417, 1948.

GOU 33 S. Goudsmit, Phys. Rev. 43, 636, 1933.

HAM 39 D. R. Hamilton, Phys. Rev. 56, 30, 1939.

HAM 41 D. R. Hamilton, Am. J. Phys. 9, 319, 1941.

HOB 54 J. P. Hobson, J. C. Hubbs, W. A. Nierenberg, and H. B. Silsbee, Phys. Rev. 96, 1450, 1954.

HOB 54A J. P. Hobson, Ph.D. Thesis, University of California, 1954.

HOB 55 J. P. Hobson, J. C. Hubbs, W. A. Nierenberg, and H. B. Silsbee, Phys. Rev. 99, 612, 1955.

HOB 56 J. P. Hobson, J. C. Hubbs, W. A. Nierenberg, H. B. Silsbee, and R. J. Sunderland, Phys. Rev. 104, 101, 1956.

HUB 54 J. C. Hubbs, Ph.D. Thesis, University of California, 1954.

HUB 55 J. C. Hubbs, J. P. Hobson, W. A. Nierenberg, and H. B. Silsbee, Phys. Rev. 99, 612, 1955.

HUB 56 J. C. Hubbs, W. A. Nierenberg, H. A. Shugart, and H. B. Silsbee, Phys. Rev. 104, 757, 1956.

HUB 57 J. C. Hubbs, W. A. Nierenberg, H. A. Shugart, and J. L. Worcester, Phys. Rev. 105, 1928, 1957.

HUB 57A J. C. Hubbs, W. A. Nierenberg, H. A. Shugart, H. B. Silsbee, and R. J. Sunderland (to be published).

KEL 46 J. M. B. Kellogg and S. Millman, Rev. Mod. Phys. 18, 323, 1946.

KEL 47 E. L. Kelley, Phys. Rev. 72, 746, 1947.

KEL 47A E. L. Kelley and E. Segre, Phys. Rev. 75, 999, 1947.

KOS 52 G. F. Koster, Phys. Rev. 86, 148, 1952.

KUS 50 P. Kusch, Lecture Notes on Molecular Beams (Columbia University, New York, 147 pp., 1950).

LAM 41 W. E. Lamb, Phys. Rev. 60, 817, 1941.

MAJ 32 E. Majorana, Nuovo Cimento 9, 43, 1932.

MAN 36 J. H. Manley, Phys. Rev. 49, 921, 1936.

MAN 36A J. H. Manley and S. Millman, Phys. Rev. 50, 380, 1936.

MAN 37 J. H. Manley and S. Millman, Phys. Rev. 51, 19, 1937.

MAR 40 H. Margenau, Phys. Rev. 57, 383, 1940.

MAY 55 M. G. Mayer and J. Hans D. Jensen, Elementary Theory of Nuclear Shell Structure (John Wiley and Sons, Inc., New York, 269 pp., 1955).

MIL 35 S. Millman, Phys. Rev. 47, 739, 1935.

MIL 36 S. Millman and M. Fox, Phys. Rev. 50, 220, 1936.

MIL 38 S. Millman, I. I. Rabi, and J. R. Zacharias, Phys. Rev. 53, 384, 1938.

MOT 55 B. R. Mottelson and S. G. Nilsson, Phys. Rev. 99, 1615, 1955.

NIE 56 W. A. Nierenberg, H. A. Shugart, H. B. Silsbee, and R. J. Sunderland, Phys. Rev. 104, 1380, 1956.

NIE 56A W. A. Nierenberg, J. C. Hubbs, H. A. Shugart, H. B. Silsbee, and P. O. Strom, Bull. Am. Phys. Soc. II, 1, 343, 1956.

NIE 57 W. A. Nierenberg, H. A. Shugart, and H. B. Silsbee, Bull. Am. Phys. Soc. II, 2, 200, 1957.

NIE 57A W. A. Nierenberg, H. A. Shugart, and H. B. Silsbee (to be published).

NIL 55 S. G. Nilsson, Kgl. Danske Videnskab. Selskab, Mat.-fys. Medd. 29, 16, 1955.

RAB 38 I. I. Rabi, J. R. Zacharias, S. Millman, and P. Kusch, Phys. Rev. 53, 318, 1938.

RAM 50 N. F. Ramsey, Atomic and Nuclear Moments (Collier's Encyclopedia, 1950).

RAM 52 N. F. Ramsey, Phys. Rev. 86, 243, 1952.

RAM 53 N. F. Ramsey, Nuclear Moments (John Wiley and Sons, Inc., New York, 169 pp., 1953).

RAM 56 N. F. Ramsey, Molecular Beams (Oxford University Press, London, 466 pp., 1956).

REN 40 N. A. Renzetti, Phys. Rev. 57, 30, 1940.

SCH 55 C. Schwartz, Phys. Rev. 97, 380, 1955.

SHU 56 H. A. Shugart, J. C. Hubbs, E. Lipworth, W. A. Nierenberg, and H. B. Silsbee, Bull. Am. Phys. Soc. II, 1, 253, 1956.

SIL 56 H. B. Silsbee, W. A. Nierenberg, H. A. Shugart, and P. O. Strom, Bull. Am. Phys. Soc. II, 1, 389, 1956.

SIL 57 H. B. Silsbee, W. A. Nierenberg, H. A. Shugart, and R. J. Sunderland, Bull. Am. Phys. Soc. II, 2, 30, 1957.

SMI 52 A. B. Smith, A. C. G. Mitchell, and R. S. Caird, Phys. Rev. 87, 454, 1952.

SMI 55 K. F. Smith, Molecular Beams (Methuen and Co., Ltd., London, 133 pp., 1955).

STE 21 O. Stern, Z. Physik 7, 249, 1921.

SUN 56 R. J. Sunderland, J. C. Hubbs, W. A. Nierenberg, and H. B. Silsbee, Bull. Am. Phys. Soc. II, 1, 252, 1956.

SUN 56A R. J. Sunderland, Ph.D. Thesis, University of California, 1956.

TEM 49 G. M. Temmer, Phys. Rev. 75, 1464, 1949; 76, 424, 1949; 76, 1002, 1949.

TOR 41 H. Torrey, Phys. Rev. 59, 293, 1941.

URE 57 J. Uretsky, private communication.

WOR 57 J. L. Worcester, private communication.

ZAC 42 J. R. Zacharias, Phys. Rev. 61, 270, 1942.